Proceedings of the Twenty-Fifth Annual Biochemical Engineering Symposium September 16, 1995

Rakesh K. Bajpai
Editor

Department of Chemical Engineering
University of Missouri, Columbia, MO

Proceedings of the Twenty-Fifth Annual Biochemical Engineering Symposium September 16, 1995

Rakesh K. Bajpai
Editor

Department of Chemical Engineering
University of Missouri, Columbia, MO

PREFACE:

The Annual Biochemical Engineering Symposium Series started in 1970 when Professors Larry E. Erickson (Kansas State University) and Peter J. Reilly (then with University of Nebraska-Lincoln) got together in Manhattan, KS along with their students for a half-day pow-wow and technical presentation by their students. Ever since then, it has been a forum for Biochemical Engineering students in the heartland of USA to present their research to their colleagues in the form of talks and posters. The institutions actively involved with this annual symposium include Colorado State University, Kansas State University, Iowa State University, University of Colorado, University of Kansas, University of Missouri-Columbia, and University of Oklahoma. The University of Iowa and University of Nebraska-Lincoln have also participated in the conference in recent years. The host institutions for the different symposia have been: Kansas State University (1, 3, 5, 9, 12, 16, 20), Iowa State University (6, 7, 10, 13, 17, 22), University of Missouri-Columbia (8, 14, 19, 25), Colorado State University (11, 15, 21), University of Colorado (18, 24), University of Nebraska-Lincoln (2, 4), University of Oklahoma (23). The next symposium will be held at Kansas State University.

Proceedings of the Symposium are edited by faculty of the host institution and include manuscripts written and submitted by the presenters (students). These often include work-in-progress and final publication usually takes place in refereed journals.

Attendees for this meeting at the University of Missouri-Columbia were:

Colorado State University: Professor James Linden, Pat Gilcrease, Miklos Pecs, Xinzhi Sun
University of Colorado: Professor Robert Davis, Professor Paul Todd, Gautam Banik, Steve Cape, Martin Heller, LoToya Jones, Jeff Kern, Pete Kunze, Ching-Yuan Lee, Antonio Payano, Travis Thelen, Barry Vant-Hull
Iowa State University: Professor Charles Glatz, Professor Peter J. Reilly, Scott E. Carver, Pedro M. Coutinho, Weiyu Fan, Zhong Gu, Carole Heath, Peng Jin, Anurag Joshi, Hsuan-Liang Liu, Mark Mawry, Greg Rutkowski, Mungara Saikumar, Arun Sivasothy, Ruta Waghmare, Ruth Fink Winter
Kansas State University: Professor Larry Erickson, Xueou Deng, Melissa Miller, Muralidharan Narayanan, Krishna Kumar V. Nedunuri, Satish Kumar Santharam, Xiaowei Wu, Qizhi Zhang
University of Kansas: Professor Marylee Southard, Soma Chakrabarti, Mike Rigney, Fred Souder, Sridhar Sunderam
University of Missouri-Columbia: Professor Rakesh Bajpai, Professor Gene Iannotti, Professor George Preckshot, Professor Robert Segar, Jun Gu, Zhonglin Jin, Jan Johansson, Prashant Karia, Kevin Leung, Yadong Li, Natalie Stennis, Krishna Subramanian, Sudhakar Vivek
Oklahoma University: Professor Roger Harrison, Greg Davis, Brad Farlow, Carolyn L. Lauron, Matt Rose, Laura Wosthen

Rakesh K. Bajpai
Columbia, MO
April 1996

Table of contents:

Use of 2,4,6-Trinitrotoluene (TNT) as a nitrogen source by a *Pseudomonas fluorescens* species under aerobic conditions.

Patrick C. Gilcrease and Vincent G. Murphy

Department of Chemical and Bioresource Engineering, Colorado State University, Fort Collins, Colorado 80523

Abstract. A *Pseudomonas fluorescens* species isolated from TNT contaminated soil utilized TNT as a sole nitrogen source under aerobic conditions. Growth as measured by four independent methods was higher in the presence of TNT when compared with a no nitrogen control. 2-amino-4,6-dinitrotoluene (2-ADNT) was an observed TNT metabolite, but separate experiments indicated that it does not serve as a nitrogen source for this organism. Picric acid and trinitrobenzene were also identified as TNT metabolites and could potentially be part of a nitrogen use pathway. Dry weight and acetate measurements indicate that a significant amount of the TNT nitrogen present was used for growth by the organism.

Abbreviations: TNT = 2,4,6-trinitrotoluene; TNB = 1,3,5-trinitrobenzene; 3,5-DNA = 3,5-dinitroaniline; 2-ADNT = 2-amino-4,6-dinitrotoluene; 4-ADNT = 4-amino-2,6-dinitrotoluene; 2,4-DANT = 2,4-diamino-6-nitrotoluene; 2,6-DANT = 2,6-diamino-4-nitrotoluene; TAT = 2,4,6-triaminotoluene; 2,2'-AZ = 4,4',6,6'-tetranitro-2,2'-azoxytoluene; 4,4'-AZ = 2,2',6,6'-tetranitro-4,4'-azoxytoluene; 4-*N*-AcANT = 4-*N*-acetylamino-2-amino-6-nitrotoluene.

The aerobic biodegradation of TNT was first investigated as another possible way to reduce TNT. While the bioreduction of TNT has been observed with aerobic cultures [1-3], it occurs more readily under anoxic or anaerobic conditions [4]. Since *Pseudomonas fluorescens* is capable of assimilatory nitrate reduction (nitrate is reduced to ammonia and used as a nitrogen source for growth), we postulated that aerobic cultures growing on nitrate might also have the ability to reduce TNT. Thus, one could take advantage of the reductive pathway without having to maintain anoxic or anaerobic conditions. While aerobic cultures growing on nitrate did not reduce TNT to the extent that anoxic (nitrate-reducing) cultures did [5], an important observation was made. Cultures designed to have nitrogen as the limiting nutrient for growth exhibited additional growth when more carbon (ethanol or acetate) was added. The fact that media designed to be nitrogen limited could become carbon limited suggested that TNT was being utilized as a nitrogen source. The use of nitroaromatic compounds as a nitrogen source has been reported by others [6-9].

The nitro groups on TNT render this compound resistant to biodegradation; hence, reduction or removal of these nitro groups appears necessary before further degradation can occur. Culture conditions where nitrogen is the limiting nutrient may promote removal and use of TNT nitrogen. The goal of this study was to demonstrate that a *Pseudomonas fluorescens* species is capable of using TNT as the sole source of nitrogen for growth under aerobic conditions. Culture growth where TNT is the only nitrogen source implies that nitrogen has been removed from the aromatic ring; the resulting aromatic compounds may lend themselves to further attack and eventual mineralization.

MATERIALS AND METHODS

Organism. The *Pseudomonas fluorescens* strain used in all experiments was isolated from TNT contaminated soils by Pat Unkefer's group at Los Alamos National Laboratory.

Medium. The medium was the same as Naumova's medium 3 [2] with the addition of the following trace minerals (g/l): $CuSO_4*5H_2O$, 1.1 $x10^{-4}$; $CoCl_2*6H_20$, 3.3 $x10^{-5}$; H_3BO_3, 7.0 $x10^{-6}$; $ZnCl_2$, 2.37 $x10^{-5}$. Carbon, nitrogen, and nitroaromatic components varied; their concentrations are noted for each experiment.

Culture conditions. All experiments were performed in 500 ml shake flasks agitated at 30°C and 150 rpm under aerobic conditions. Isolated colonies from nutrient agar plates were used to inoculate 200 ml of liquid starter medium, which contained the same carbon substrate used in the degradation experiment (2.0 g/l ethanol or sodium acetate) and 0.2 g/l KNO_3 (no TNT or other nitroaromatics). Starter cultures were incubated at 25-30°C and 150 rpm for 24 hours. For unwashed cell inoculum, 20 ml of starter culture was directly used to inoculate 200 ml of nitroaromatic medium. For washed cell inoculum, the starter culture was centrifuged, decanted, washed with sterile phosphate buffer (0.4 g/l KH_2PO_4, 0.69 g/l Na_2HPO_4), centrifuged and decanted again, and finally resuspended in 200 ml sterile phosphate buffer. 20 ml of this suspension was used to inoculate 200 ml of the nitroaromatic medium.

Analytical. TNT and its metabolites were detected and quantified by high pressure liquid chromatography (HPLC). The reversed-phase column was a Rainin Microsorb C8 80-315-C5. Separations were performed using a solvent gradient program with 0.003 N H_2SO_4 (A) and acetonitrile (B) as the mobile phases. The gradient program was as follows: 0 to 4 min, 90% A-10% B; 5 to 15 min, 50% A/50% B; 16 to 25 min, 15% A-85% B; 26 to 30 min, 90% A-10% B. Changes between compositions were made via a linear ramp over 1 min. Total flow rate was held constant at 1.0 ml/min. Compounds were detected by measuring UV A_{254} with a Waters 486 Tunable Absorbance Detector. Selected samples were run on a separate HPLC system with a Beckman Module 168 Diode Array Detector. 2-ADNT, 4-ADNT, 2,4-DANT, TNB, 3,5-DNA, picric

acid, and 4-*N*-AcANT were identified by HPLC comparisons with standards. Acetate was also quantified via HPLC; the isocratic method used a Biorad HPX-87H column at 65°C, 0.6 ml/min of 0.008 N H_2SO_4 for 22 minutes, and UV A_{210}.

Optical density readings (560 nm) were corrected for absorbance by TNT metabolites by subtracting the absorbance of a filtered (0.45 μm) sample from the absorbance of the raw (unfiltered) sample. Nitrite was assayed colorimetrically using the sulfanilamide method [10].

Chemicals. TNT was obtained from Chem Service, Inc. phloroglucinol, pyrogallol, 2,6-DANT, 2,4-dinitrotoluene, 2-nitrotoluene, 4-nitrotoluene, toluene, 2,4-dinitrophenol, 3,5-DNB, 1,3-dinitrobenzene, 3-nitroaniline, and nitrobenzene were obtained from Aldrich. 2-ADNT, 4-ADNT, 2,4-DANT, TAT, 4,4'-AZ, 2,2'-AZ, TNB, 2,4,6-trinitrobenzaldehyde, 2,4,6-trinitrobenzoic acid, picric acid, and 4-*N*-AcANT standards were generously provided by Ron Spanggord of SRI International.

RESULTS

Experimental results for a culture containing TNT as the sole nitrogen source are presented in Figure 1A. Sodium acetate was the carbon source, and TNT was the sole nitrogen source. A flask containing acetate but no TNT or other nitrogen source served as the control. TNT was transformed in this experiment, and was completely gone at 350 hours. Growth as indicated by optical density (560 nm) and acetate consumption was greater for the culture containing TNT. Plate counts at 291, 428 hours, and dry weights at 571 hours all confirm additional growth in the presence of TNT (see Table 1). Identified TNT metabolites were 2-ADNT, TNB, 3,5-DNA, and picric acid; final concentrations at 566 hours account for 10.5, 0.7, 4.0, and 1%, respectively, of the TNT that disappeared. A slight shoulder on the right of the 2-ADNT peak suggested a small amount of 4-ADNT present, but diode array scans indicated that 2-ADNT was the predominant isomer. The 2-ADNT that was formed remained persistent, while the TNB concentration went through a maximum at 230 hours. The decline in TNB concentration after this time was associated with the formation of the TNB reduction product 3,5-DNA. Picric acid (not shown in Fig. 1) was first detected at 230 hours; the maximum concentration at 422 hours was equal to 1% of the TNT initially present. In a repeat experiment, nitrite in the culture fluid was measured colorimetrically. A nitrite spike occurred at 50 hours; the observed NO_2^- concentration was 0.007 mM or 0.6% of the NO_2 present as TNT. A similar spike was also observed in the no nitrogen control culture at 25 hours; the nitrite concentration was 0.004 mM in this case.

Three significant unknown compounds appeared at 50 hours, and a fourth unknown appeared at 160 hours. Diode array scans did not match any of the compounds listed in Materials and Methods, but did indicate that all four unknowns were aromatic. None of these unknowns were observed in the control culture

without TNT, indicating they are TNT-related. Peak areas for these unknown compounds are shown in Figure 1B, and a representative HPLC chromatogram is shown in Figure 2. Areas for the first and third unknown peaks reached a maximum at 230 hours, while the areas of the second and fourth unknowns were still increasing at 566 h. The sum of all unknown peak areas at 566 hours add up to 8% of the TNT peak area at time zero.

A second aerobic experiment with acetate and TNT as the sole nitrogen source was performed; conditions were identical to those above except that the inoculum had been washed and suspended in a phosphate buffer. A second control containing acetate and no nitrogen was also inoculated from the same washed cell batch. Results were similar to the first experiment, except that a 300 hour (approx.) lag period was observed before the onset of TNT disappearance and growth (Figure 3). All of the initial TNT (95 mg/l) disappeared by 930 h. Acetate and O.D. curves in the control were flat this time; apparently the residual nitrogen in the unwashed inoculum allowed for some growth and accelerated the TNT degradation process. Final growth measurements are shown in Table 2; once again all values indicate additional growth in the presence of TNT. Final 2-ADNT, TNB, 3,5-DNA, and picric acid concentrations account for 8.5, 3.2, 3.7, and 1%, respectively, of the initial TNT. Final unknown peak areas at 930 h add up to 9% of the initial TNT peak area.

In order to determine whether 2-ADNT or 4-ADNT was an intermediate in the pathway for nitrogen usage, or simply a dead end metabolite, the experiment shown in Figure 4 was performed. In this case 2-ADNT (9.4 mg/l) and 4-ADNT (27.9 mg/l) were provided as the sole nitrogen source, and acetate was again provided as the carbon source. 2-ADNT remained completely persistent, while some 4-ADNT transformation took place. 24% of the 4-ADNT had been transformed after 930 hours, but O.D. and acetate curves indicated no growth above that of the no nitrogen control. 2,4-DANT and 4-*N*-AcANT were observed as metabolites; final concentrations (1.2,1.5 mg/l) account for 22 and 21%, respectively, of the 4-ADNT degraded.

Preliminary experiments were run with either TNB or picric acid as the sole nitrogen source and sodium acetate (2.0 g/l) as the carbon source. For TNB, the initial concentration was 70 mg/l, and 7% of this was degraded after 2 months. 15% of the TNB degraded was accounted for as 3,5-DNA. No transformation of picric acid was observed after 2 months; the initial picric acid concentration for this experiment was 170 mg/l.

DISCUSSION

Four different measurements of culture growth were obtained for the experiment shown in Figure 1A; all indicate additional growth when TNT was present as the sole nitrogen source when compared with a control containing no added nitrogen source. Typical values for the weight percent nitrogen in dry biomass (12%, [11]), and the yield coefficient for *Pseudomonas*

fluorescens growing on acetate (16.8 g DW/mol acetate [12]) were used to estimate the additional biomass formed and acetate consumed *if* the TNT present were used as a nitrogen source. TNT accounted for as 2-ADNT, TNB, 3,5-DNB, or picric acid was not included in these calculations. For the experiment shown in Figure 1A and Table 1, the additional biomass formed in the presence of TNT (0.193 g dry biomass/l) is actually 60% greater than the theoretical value (0.12 g dry biomass/l) based on the above assumptions. While the theoretical value is merely an estimate, this calculation suggests that a significant amount of the TNT nitrogen was used for growth. An additional 0.493 g/l of sodium acetate was consumed in the flask containing TNT compared to the control. If all the TNT nitrogen not accounted for as known metabolites were used for biomass, this would theoretically result in 0.586 g/l of acetate consumption. Thus the additional acetate consumed was 84% of theoretical, again suggesting that a significant amount of the TNT nitrogen ends up as biomass nitrogen.

The fact that no growth was observed when 2-ADNT + 4-ADNT was the sole nitrogen source with acetate (Figure 3) gives credence to the argument that ADNT is not part of the pathway by which nitrogen is removed from the aromatic ring. While some conversion of 4-ADNT to 2,4-DANT and 4-*N*-AcANT was observed, previous experiments suggest that this organism cannot use 2,4-DANT as a source of nitrogen [5]. Since growth with TNT as the sole nitrogen source was confirmed, there must be another unknown metabolic pathway that leads to removal of nitrogen from the TNT molecule. While Duque et al. [8] report the removal of nitrite to form dinitrotoluene, nitrotoluene, and toluene, none of these compounds was observed in our cultures. One would not expect to see nitrite accumulation in our cultures, since this strain has demonstrated the ability to use nitrate as a nitrogen source. The observance of a nitrite spike when TNT was the sole nitrogen source may or may not be significant, since a similar spike was observed in the control culture.

The observance of picric acid and trinitrobenzene was surprising, since this implies that the initial attack on the TNT molecule involves the methyl group rather than the nitro group. The transient accumulation of TNB, and the minute concentrations of picric acid tends to suggest that these are intermediates rather than end products. Lenke and Knackmuss [9] report the use of picric acid as a nitrogen source by a *Rhodococcus erythropolis* strain; in this case nitrite was removed to form 2,4-dinitrophenol. However, 2,4-dinitrophenol was not observed in the TNT or the picric acid cultures, and picric acid was not degraded when present as the sole nitrogen source. The use of TNB as a sole source of nitrogen by a *Pseudomonas* consortium was reported by Boopathy et al. [6]; the reported pathway is shown in Figure 5. 3,5-DNA is the only metabolite in this pathway that has been observed in our cultures, and little degradation occurred when TNB was used as the sole nitrogen source. These results suggest that picric acid and/or TNB are not part of the

the nitrogen use pathway, but the high concentrations used in our sole nitrogen source experiments (70 mg/l TNB; 170 mg/l picric acid) may have been toxic to the cultures. Further experiments at lower concentrations of TNB/picric acid are needed to confirm this observation.

The amount of TNT reduced to 2-ADNT (11%, 8%) in these experiments is quite low compared to other reports of aerobic TNT degradation by bacteria. Boopathy et al. report that with aerobic degradation of TNT by a *Pseudomonas aeruginosa* species, 85% of the TNT initially present was accounted for as either 2-ADNT, 4-ADNT, or an unknown metabolite [13]. While Duque et al. [8] demonstrated removal of nitrite from the TNT molecule under aerobic conditions, they also reported that the most abundant TNT metabolites were 2-ADNT, 4-ADNT, and azoxy dimers. For aerobic soil cultures, Funk et al. [14] reported that 15% of the ^{14}C labeled TNT was accounted for as 4-ADNT, 5% as 2,4-DANT, and 71% as an insoluble material (speculated to be polymerized azoxy compounds). Since ADNT appears to be persistent under aerobic conditions, it may be important to minimize the amount of ADNT formed. The fact that only 24% (approx.) of the TNT that disappears in our cultures can be accounted for as known or unknown aromatics (UV A_{254}) is also significant. It suggests that ring cleavage may be occurring in these TNT cultures; further experiments with ^{14}C labeled TNT are needed to verify that mineralization takes place.

CONCLUSIONS

Growth of this *Pseudomonas fluorescens* species with TNT as the sole nitrogen source indicates that nitrogen is being removed from the aromatic ring of the TNT molecule. While the mechanism for nitrogen removal is unknown at this point, biomass yield and acetate consumption values indicate that a significant amount of the TNT nitrogen was converted to biomass. ADNT, picric acid, and TNB were identified as TNT metabolites, but do not appear to be part of the nitrogen use pathway. The high conversion of TNT nitrogen to biomass and the relatively low conversion of TNT to ADNT are attractive aspects of this degradation scheme. Since the removal of nitrogen from the TNT molecule renders it more susceptable to further degradation and ring cleavage, the use of TNT as a nitrogen source could prove to be an important first step in the complete biodegradation/ mineralization of TNT.

ACKNOWLEDGEMENTS

This work was supported in part by a fellowship from the Colorado Institute for Research in Biotechnology.

We thank Pat Unkefer of Los Alamos National Laboratory for providing the culture, and Ron Spanggord of SRI International for providing compound standards. We also thank Shirley Nishino and Jim Spain of Tyndall Air Force Base for their assistance with metabolite identification.

REFERENCES

1. McCormick, N.G., F.E. Feeherry, and H.S. Levinson, *Microbial transformation of 2,4,6-trinitrotoluene and other nitroaromatic compounds.* Applied and Environmental Microbiology, 1976. **31**(6): p. 949-958.

2. Naumova, R.P., S.Y. Selivanovskaya, and I.E. Cherepneva, *Conversion of 2,4,6-trinitrotoluene under conditions of oxygen and nitrate respiration of Pseudomonas fluorescens.* Prikladnaya Biokhimiya i Mikrobiologiya, 1988. **24**(4): p. 493-498.

3. Schackmann, A. and R. Müller, *Reduction of nitroaromatic compounds by different Pseudomonas species under aerobic conditions.* Applied Microbiology and Biotechnology, 1991. **34**: p. 809-813.

4. Preuß, A. and P.-G. Rieger, *Anaerobic transformation of 2,4,6-trinitrotoluene and other nitroaromatic compounds,* in *Biodegradation of nitroaromatic compounds,* J.C. Spain, Editor. 1995, Plenum Press: New York. p. 69-85.

5. Gilcrease, P.C. and V.G. Murphy, *Bioconversion of 2,4-diamino-6-nitrotoluene to a novel metabolite under anoxic and aerobic conditions.* Applied and Environmental Microbiology, 1995. **61**(12): p. in press.

6. Boopathy, R., *et al.*, *Metabolism of trinitrobenzene by a Pseudomonas consortium.* Canadian Journal of Microbiology, 1994. **40**: p. 787-790.

7. Bruhn, C., H. Lenke, and H.-J. Knackmuss, *Nitrosubstituted aromatic compounds as nitrogen source for bacteria.* Applied and Environmental Microbiology, 1987. **53**(1): p. 208-210.

8. Duque, E., *et al.*, *Construction of a Pseudomonas hybrid strain that mineralizes 2,4,6-trinitrotoluene.* Journal of Bacteriology, 1993. **175**(8): p. 2278-2283.

9. Lenke, H. and H.-J. Knackmuss, *Initial hydrogenation during catabolism of picric acid by Rhodococcus erythropolis HL 24-2.* Applied and Environmental Microbiology, 1992. 58(9): p. 2933-2937.

10. Rand, M.C., A.E. Greenberg, and M.J. Tarasled, ed. *Standard methods for the examination of water and wastewater.* 14 ed. 1976, American Public Health Association: Washington, D.C. 434-436.

11. Atkinson, B. and F. Mavituna, *Biochemical engineering and biotechnology handbook.* 1983, Surrey, England: Macmillan Publishers Ltd. 120.

12. Nagai, S., *Mass and energy balances for microbial growth kinetics,* in *Advances in biochemical engineering,* T.K. Ghose, A. Fiechter, and N. Blakebrough, Editor. 1979, Springer-Verlag: New York. p. 53.

13. Boopathy, R., *et al.*, *Biological transformation of 2,4,6-trinitrotoluene (TNT) by soil bacteria isolated from TNT-contaminated soil.* Bioresource Technology, 1994. 47: p. 19-24.

14. Funk, S.B., *et al.*, *Initial-phase optimization for bioremediation of munition compound-contaminated soils.* Applied and Environmental Microbiology, 1993. 59(7): p. 2171-2177.

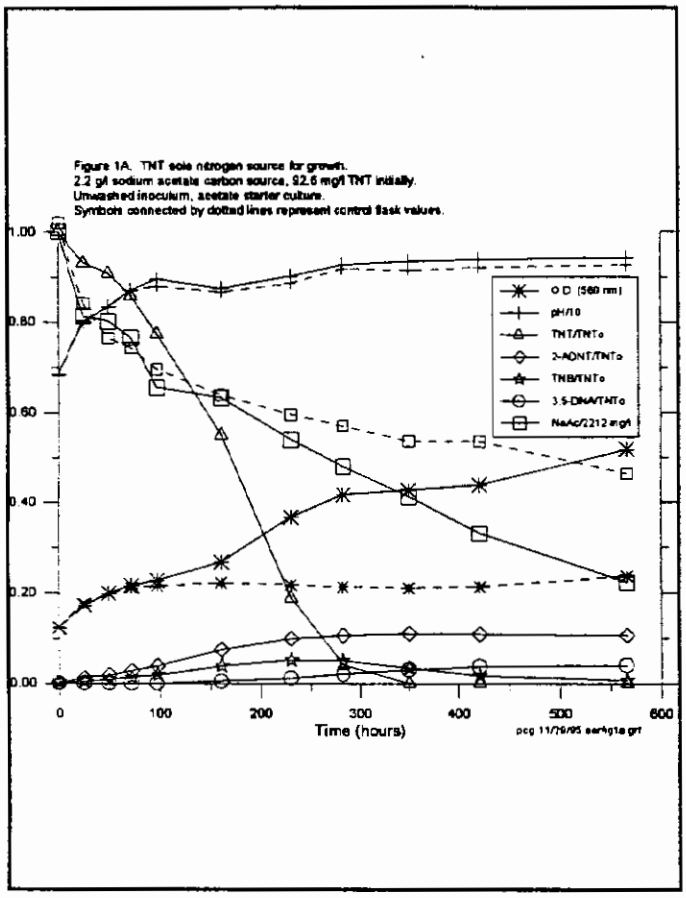
Figure 1A. TNT sole nitrogen source for growth.
2.2 g/l sodium acetate carbon source, 92.6 mg/l TNT initially.
Unwashed inoculum, acetate starter culture.
Symbols connected by dotted lines represent control flask values.
O D (560 nm)
pH/10
TNT/TNTo
2-ADNT/TNTo
TNB/TNTo
3,5-DNA/TNTo
NaAc/2212 mg/l
Time (hours)
pcg 11/29/95 aerfig1a.grf

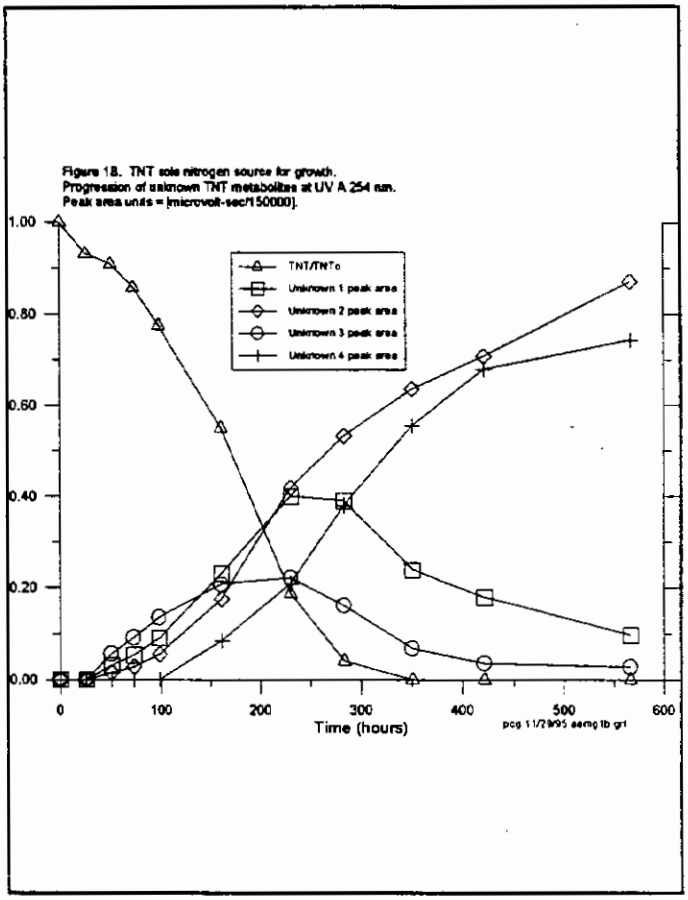
Figure 1B. TNT sole nitrogen source for growth.
Progression of unknown TNT metabolites at UV A 254 nm.
Peak area units = [microvolt-sec/150000].
TNT/TNTo
Unknown 1 peak area
Unknown 2 peak area
Unknown 3 peak area
Unknown 4 peak area
Time (hours)
pcg 11/29/95 aerfig1b.grf

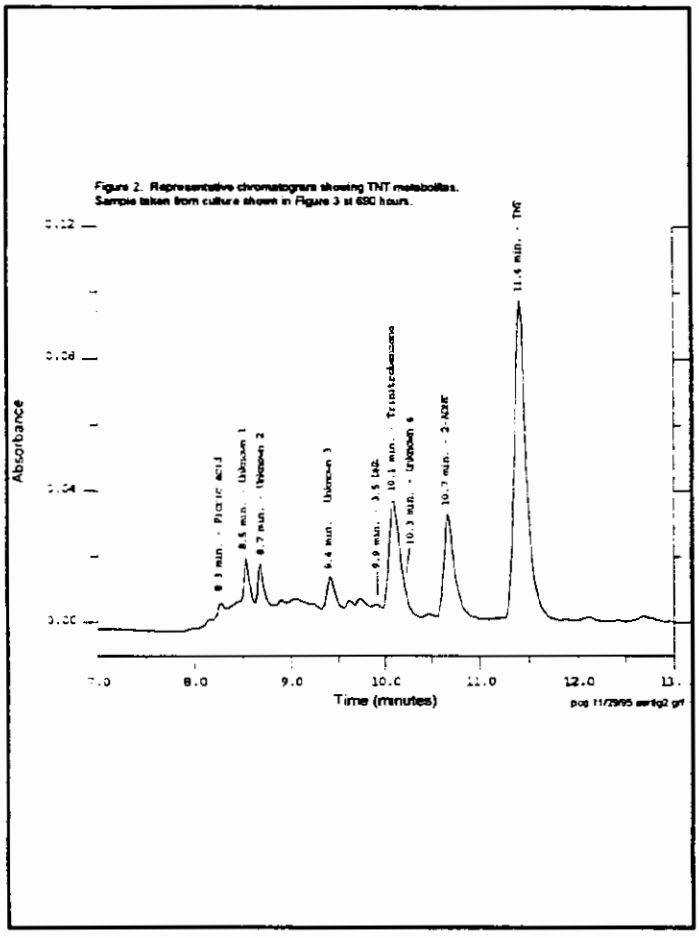
Figure 2. Representative chromatogram showing TNT metabolites.
Sample taken from culture shown in Figure 3 at 690 hours.
Absorbance
8.3 min. - Picric acid
8.5 min. - Unknown 1
8.7 min. - Unknown 2
9.4 min. - Unknown 3
9.9 min. - 3,5 DNA
10.1 min. - Trinitrobenzene
10.3 min. - Unknown 4
10.7 min. - 2-ADNT
11.4 min. - TNT
Time (minutes)
pcg 11/29/95 aerfig2.grf

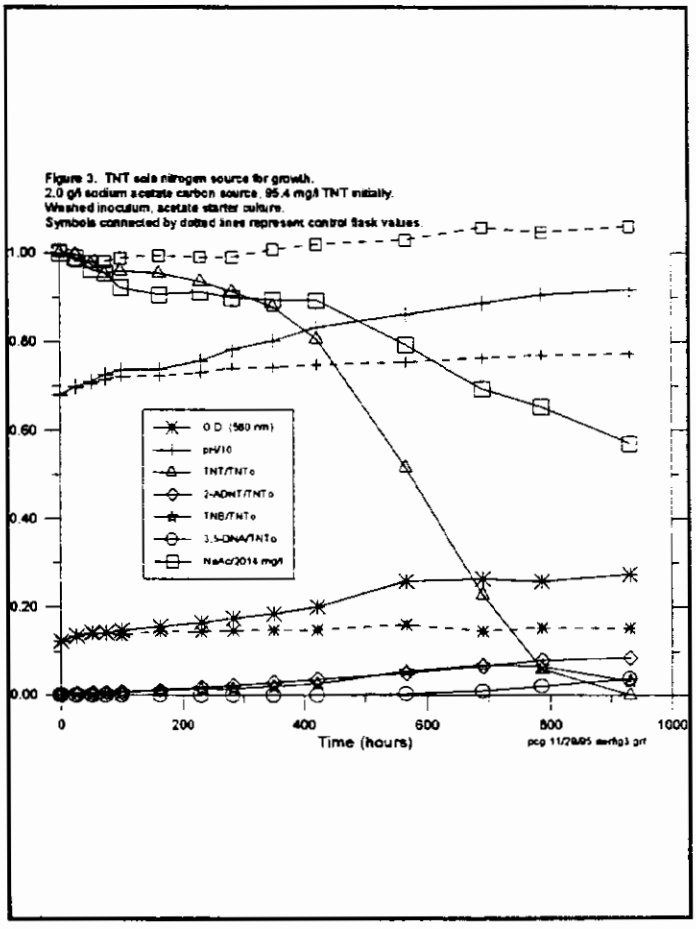
Figure 3. TNT sole nitrogen source for growth.
2.0 g/l sodium acetate carbon source, 95.4 mg/l TNT initially.
Washed inoculum, acetate starter culture.
Symbols connected by dotted lines represent control flask values.
O D (560 nm)
pH/10
TNT/TNTo
2-ADNT/TNTo
TNB/TNTo
3,5-DNA/TNTo
NaAc/2014 mg/l
Time (hours)
pcg 11/29/95 aerfig3.grf

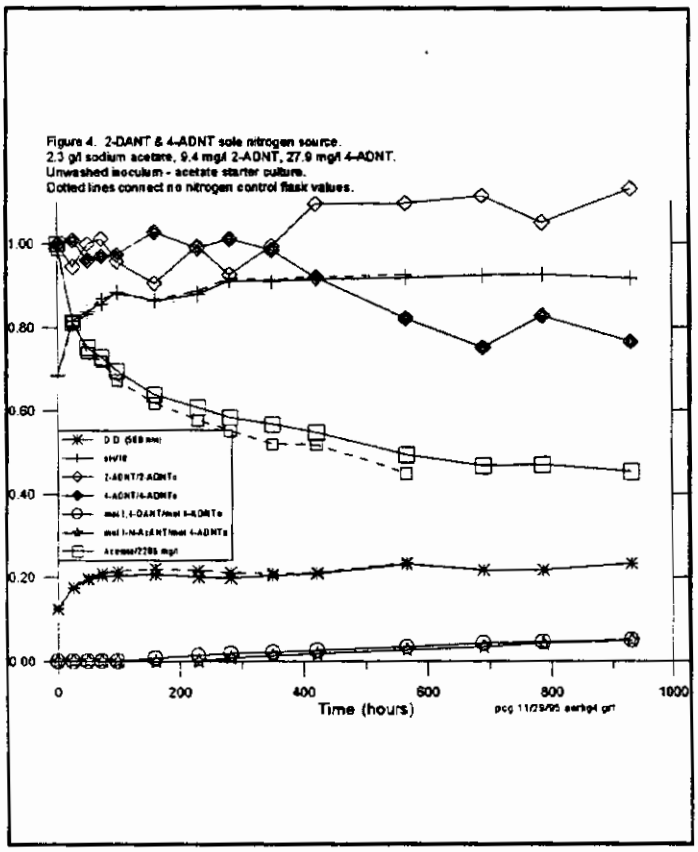

TABLE 1

Evidence for additional growth in the presence of TNT. Acetate carbon source, TNT sole nitrogen source. Unwashed cell inoculum experiment (Figure 1A,B).

Plate counts ± std. dev. (10^{-6} dilution, 5 replicate plates)

	291 hrs.	428 hrs.
A (with TNT)	175 ±50	171 ±14
B (no TNT)	134 ±74	139 ±21

Dry weights at 571 hours (entire flask used):

A	0.375 g/l
B	0.182 g/l

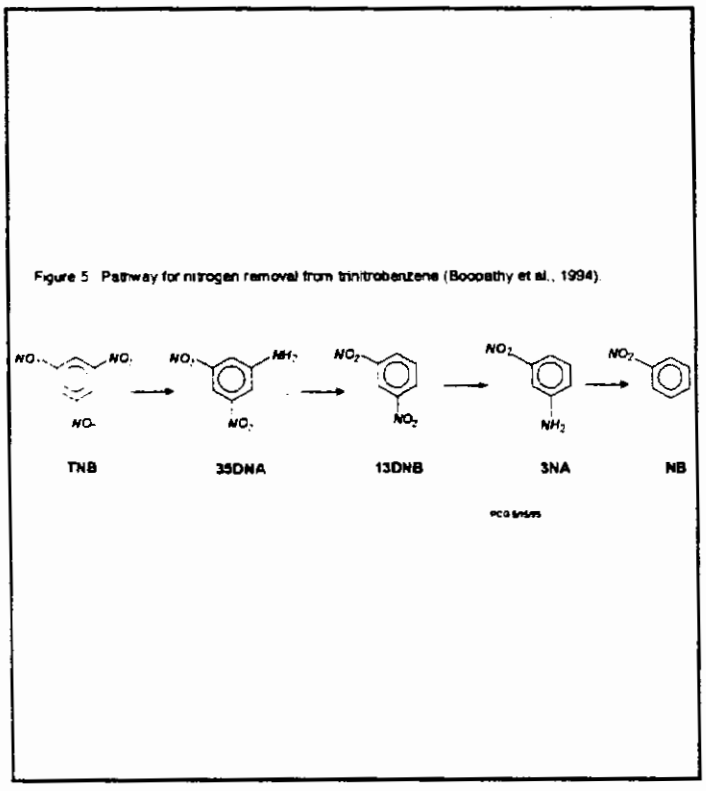

TABLE 2

Evidence for additional growth in the presence of TNT. Acetate carbon source, TNT sole nitrogen source. Washed cell inoculum experiment (Figure 3). All measurements taken at 933 hours after inoculation.

	Plate cnt ± std.dv.	Dry wt (g/l)	O.D. (560 nm)	Acetate (g/l)
With TNT	40.8 ±4.6	0.169	0.274	1.15
No TNT	13.4 ±8.0	0.112	0.153	2.13

Plate counts are for 10^{-6} dilution, 5 replicate plates. Dry weights were obtained by centrifuging the entire culture. Optical density values corrected for metabolite absorbance. Starting Acetate concentrations were 2.01, 2.03 g/l. Starting O.D. values 0.122, 0.123.

Biodegradation Studies of Chlorinated Organic Pollutants in a Chamber in the Presence of Alfalfa Plants

Muralidharan Narayanan[a], Lawrence C. Davis[b], and Larry E. Erickson[a]

Departments of [a]Chemical Engineering and [b]Biochemistry, Kansas State University, Manhattan, KS 66506-5102 (USA)

ABSTRACT

To investigate the influence of alfalfa plants on the fate and transport of volatile chlorinated compounds, two channels in a laboratory chamber were utilized. Bioremediation experiments were conducted in these two channels, each 35 cm deep, 1.8 m in axial length, and 10 cm wide, containing sandy silt soil and alfalfa plants. Plants were fed continuously with water contaminated with chlorinated compounds for more than one year. One channel was fed with 1,1,1 -trichloroethane (TCA) and chloroform in the entering water, each at a concentration of 100 μL/L of water; the other channel was fed with trichloroethylene (TCE) at a concentration of 200 μL/L of water. Daily phenol or acetate additions were made through recharging wells. The results were compared to earlier studies with TCA and TCE as contaminants in the inflow water to the channel where phenol solution had been previously fed as the inflow contaminated groundwater. The contaminant concentrations in the groundwater were measured using gas chromatographic headspace analysis technique. Observations indicated complete disappearance of phenol or acetate, presence of some chlorinated biodegradation intermediates, and significant concentrations of the parent compounds in the groundwater and soil-gas. FT-IR instrumentation was used to monitor the evapotranspiration losses of these chlorinated contaminants to the chamber atmosphere.

Key words: Vegetation, volatile organics, headspace analysis, biodegradation.

INTRODUCTION

Bioremediation. Trichloroethylene (TCE) is a suspected carcinogenic chlorinated aliphatic organic contaminant. This pollutant is most prevalent in the groundwater of contaminated Superfund sites. The safe drinking water concentration limit of TCE is about 5 μg/L (*1*). In groundwater, TCE could be anaerobically bioremediated either under methanogenic or denitrifying conditions. However, more toxic products may be produced. *In situ* aerobic cometabolic bioremediation of TCE to carbon-dioxide and water has also been demonstrated by several researchers (*1*).

Bioremediation in the Presence of Plants. Research is in progress to identify the role of plants in the bioremediation of TCE and other chlorinated pollutants in groundwater (*1-4*). Soil-ecosystems involving plant roots usually possess a wide spectrum of compounds including sugars, amino acids, carbohydrates, and essential vitamins that are exuded from the root tips. These energy and growth yielding substrates support a diverse variety of mixed microbial consortia in the root zone of the plants (rhizosphere) (*2-4*).

The objectives of this research were to investigate qualitatively the extent of biodegradation of TCE and TCA in the rhizosphere of alfalfa plants growing in a laboratory chamber and to simultaneously monitor the generation of any toxic biodegradation intermediates that might be formed during plant-based bioremediation. This paper is a follow-up of earlier work (*1, 5*) and discusses some of the recent progress towards the accomplishment of the above goals.

MATERIALS AND METHODS

Experimental Chamber. A chamber consisting of channels of dimensions 10 cm in width, approximately 1.8 m in axial flow length, and 35 cm in depth was employed for the study. The design and construction of the experimental setup was described previously (*1, 6*). Figure 1 shows the frontal view of the laboratory chamber when it is imagined to be axially extended. The channels were packed with sandy silt soil and alfalfa plants were established in the soil under laboratory conditions in June, 1992. A glass and aluminium enclosure 26 cm high was constructed above the ground level of the chamber for gas phase monitoring of the chamber.

Microbial growth occurred in the chamber in the presence of alfalfa plants during the feeding operation of the different pollutants in the feed water. Table I shows the various pollutants fed to the chamber along with their concentrations and feeding periods.

Analysis of Subsurface Chlorinated Compounds. Groundwater samples collected from inlet, four sampling wells, and outlet were immediately transferred to nominal 10 mL bottles and capped with a Pierce reacti-vial screw cap with mininert valves. The concentrations of these chlorinated hydrocarbons in the groundwater samples were then analyzed using a gas chromatographic headspace analysis technique which involved injecting 1 mL of the equilibrated headspace gas of the samples into a gas chromatograph (GC) fitted to a flame ionization detector.

Recharging. Primary substrates such as phenol or acetate were added to the channel soil through recharging wells located 20 cm from the inlet in order to support the cometabolic transformation of TCE (Fig. 1). Phenol at a concentration of 1 g/L was recharged for 120 days at a rate of 50 mL/day. The period of recharging phenol was from Sept. 1994 to Dec. 1994. Acetate at a concentration of 4.2 g/L is being recharged starting from May 1995 also at a rate 50 mL/day.

Table I. Feeding History of the Various Pollutants Introduced to the two Channels of the Chamber.

Channel #1			Channel #2		
Contaminant feed	Conc. in feed water	Feeding period	Contaminant feed	Conc. in feed water	Feeding period
Toluene	550 mg/L	6/92 - 5/93	Phenol	500 mg/L	6/92 - 5/93
Pure water	0	6/93 - 7/93	Pure water	0	6/93 - 7/93
1993 study					
Phenol	100 mg/L	7/93 - 11/93	(i) TCE	100 μL/L 200 μL/L	7/1 - 8/7/93 8/8 - 10/14/93
			(ii) TCA	100 μL/L 50 μL/L	7/1 - 7/24/93 7/25 - 10/14/93
Pure water	0	10/15 - 12/1/93	Pure water	0	10/15 - 12/1/93
1994 study					
(i) TCA (ii) $CHCl_3$	100 μL/L 100 μL/L	1/94 - 7/94	TCE	200 μL/L	1/94 - present
TCE	200 μL/L	8/94 - present			

Analysis of the Headspace using FT-IR Instrumentation. Gas phase monitoring of TCE and TCA that may be evapotranspired to the headspace of the chamber was done using the Fourier Transform Infra Red (FT-IR) instrument described previously (*1*). The FT-IR instrument was used also to search the IR spectrum of the headspace gas sample in order to determine the presence of any volatile intermediates formed during the biodegradation of TCE and TCA. Headspace gas samples of the enclosed chamber were also monitored immediately after harvesting the above-ground plant biomass to 5 cm from the soil surface. Comparison of the observed FT-IR spectra with corresponding standard spectra were also made.

Chloride Analysis in Soil and Groundwater. Soil samples were collected from different locations along the channel after the 1993 study. Accumulation of chloride in the soil samples as chloride salts in each gram of the dry soil sample was estimated. Groundwater samples were also

analyzed for dissolved chloride concentration (*1*). In September 1994, four blocks of rhizosphere soil of dimensions 4 x 4 x 4 cm were collected from the surface of the channels and similarly analyzed for accumulation of chloride (*1*).

Soil-Gas Analysis. Analysis of the soil-gas in the channel was performed by inserting several tubes into the channel soil. The cylindrical tubes were closed by a rubber septa from one end, while the other end was pierced through the soil to the desired depth. Soil-gas was then allowed to equilibrate with the gas in the tubes. After equilibration, samples of the gas were collected by inserting a syringe through the rubber septa of the tubes. The collected gas samples were then injected into the GC apparatus and analyzed.

Mesocosm Studies. In December 1994, the oven-dried blocks of rhizosphere soil (mentioned above), weighing about 450 g, were enclosed with 0.5 liters of water in 1-liter capacity sealed mesocosm. A septum was provided at the top for obtaining headspace gas samples. Anaerobic conditions were established in the container by replacing the headspace gas with nitrogen. Trichloroethylene and 1,1,1-trichloroethane (TCA) were injected in the container at 300 μL/L and 100 μL/L respectively. Headspace gas samples were then periodically collected and analyzed using the GC apparatus.

RESULTS

The flow processes in the plant growth chamber reached steady state in a few weeks from the time of introducing the contaminants. During steady state operation, the adsorbed concentrations of contaminants approached constant values; the biodegradation rates of the contaminants and growth rates of the microbes reached a plateau; and all transpiring plants became well-adapted to growth in the presence of the contaminants.

Analysis of Subsurface Groundwater. Groundwater concentration measurements for TCA, TCE and methane for the 1993 study period (see Table 1 for this period) were previously published (*1*). Gas phase measurements during the same period and chloride analysis following the study were also reported. By following the loss of TCE and generation of methane it appeared that methanogenic degradation of TCE was occurring in the saturated zone of the channel soil. Methanotrophic degradation of TCE through a cometabolic transformation was also occurring in the vadose zone of the soil. Upward movement of the dissolved solutes was greatly facilitated due to the evapotranspiration phenomenon associated with alfalfa plants (*1*).

Groundwater measurements during the 1994 study showed that TCE concentration trends at the various ports during steady state operation were similar to those in the 1993 study (Table II). However, two significant differences were observed. One was the disappearance of methane in

the groundwater (concentrations were below the detection limits; this is indicated by nd in Table II) and the other was appearance of some biodegradation intermediates in the recent study unlike the 1993 study. The retention time in the GC apparatus indicated that one of the TCE biodegradation intermediates observed may be 1,2 cis-dichloroethylene (1,2, c-DCE). This was independently confirmed with the FT-IR instrument.

It should be noted that during March of 1994, the chamber was inoculated with a proprietary microbial mixture (Bacterra) which introduced new organisms. It is not known how this might affect the metabolic pathways that predominate in the chamber.

Recharging. Phenol was recharged into each channel through the respective recharging well. The purpose of choosing phenol at 1 g/L concentration was to trigger methanogenic degradation in the channel soil by rapidly consuming the oxygen in the inflow water. Methanogenic conditions would then biodegrade TCE in the groundwater of the channel. However, results indicated that the concentration of TCE remained unchanged when compared to the 1993 study (Table II). Also, the appearance of some dissolved intermediates was observed. Methane in the groundwater was consistently below the detection limits of the GC apparatus during the 1994 study.

Acetate recharging was also undertaken to enhance the methanogenic population in soil. The effect of acetate on the groundwater concentration of TCE was also relatively insignificant. Concentrations of the intermediates and methane in the groundwater remained nearly unchanged during acetate recharging operation. Therefore, it was inferred that phenol or acetate failed to stimulate methanogenic degradation of TCE in the saturated zone of the soil.

Table II. Observations during the various treatment phases of the chamber.

Study (year)	TCE* (O/ I ratio)	Methane (outlet, mg/L)	Chlorinated Intermediates
with plants (1993)	0.73	14.4	nd
no plants (1994)	0.74	nd	observed
with plants (1994)	0.74	nd	observed
phenol recharge	0.80	nd	observed

* Concentration ratio of effluent to influent groundwater.

The only significant observations that could be drawn from the groundwater concentrations of the 1993 and 1994 studies are regarding the disappearance of methane and appearance of chlorinated intermediates as shown in Table II. Essentially, TCE was degraded anaerobically in both cases, whereas, in the 1993 study TCE was degraded by methanogenic populations. Our 1994 observations were consistent with other researchers who observed anaerobic degradation of TCE leading to the formation of toxic chlorinated intermediates.

Analysis of the Headspace gas. Previously, gas phase measurements showed accumulation of TCE in the headspace of the enclosed chamber. However, methane concentrations in the headspace were below the detection limits of the FT-IR instrument. Accumulation of TCE varied significantly with the evapotranspiration rates from the soil. Observed evapotranspiration rates of the enclosed system were usually 1/2 - 1/3 of their actual values when the chamber was open. Hence, estimates of volatilization of TCE indicated that at least 0.3 mmoles/day was accumulating in the chamber during the 1993 study. Recent observations indicated that the estimates of volatilization rates of TCE remained nearly unchanged during the recent study.

Chloride Analysis. Chloride measurements after the 1993 study indicated about 17% of TCE was biodegraded either cometabolically or by methanogenic degradation in the groundwater of the chamber. Blocks of soil (64 cm^3) collected from the surface of the channel soil in September of 1994 showed accumulation of chloride in both the channels. Estimates of chloride accumulation in the surface of channel #2 soil after the 1993 study and the 1994 study were not comparable. Table III shows a comparison of this data. The results during the 1994 study are consistent with our observations that methanogenic degradation was not occurring in the channel soil and hence chloride accumulation was lower. Trichloroethylene was predominantly degraded under anaerobic conditions to its chlorinated intermediates. This is unlike the 1993 study when TCE was biodegraded by methanogens to methane which eventually resulted in chloride accumulation in the channel soil. Channel #1 shows the biodegradation of other chlorinated compounds (TCE, TCA, and chloroform) during various treatment phases in the soil.

Table III. Comparison of chloride accumulation in the top 4 cm of surface soils.

	Chloride accumulation in the top 4 cm of surface soil (mg/kg)	
	1993 study	1994 study
Channel #1	215	1170
Channel #2	600	440

Soil-Gas Analysis. Analysis of the soil-gas samples showed qualitatively the appearance of

DCE and other products. Figure 2 shows the qualitative trends in the concentration of TCE and DCE in the channel, between 1st to 15th of July '95, during the acetate recharging period. The bar representing other compounds in Fig. 2 include all monochlorinated and non-chlorinated end products such as methane, ethane, ethylene, vinyl chloride, and chloroethane in the gas samples. As these organic compounds were unresolved at the operating GC temperature, they appeared as a single peak in the recorder. On comparison of samples obtained from the same depth it was seen that soil-gas closer to the recharging well generally showed lower concentrations of TCE and higher concentrations of DCE. This could be attributed to the active zone of anaerobic biotransformation created in the vicinity of the recharging well by the organisms that consumed acetate and oxygen. Anaerobic environments may have facilitated the conversion of some TCE to DCE in these samples. Soil-gas samples closer to the surface showed insignificant contaminant concentrations in the channel soil with plants. This may be due to rapid volatilization of these compounds from the surface soil into the atmosphere of the open chamber, as these contaminants are highly volatile in nature (*1*).

Mesocosm Studies. Studies carried out in mesocosm were entirely under anaerobic conditions. The data can be compared with the anaerobic degradation results occurring in the channel soil with alfalfa plants during the 1994 study. Mesocosm studies also showed the appearance of different chlorinated intermediates in the headspace gas samples. Figure 3 shows the appearance of different compounds on the recorder of the GC with varying temperature. It may be noted that there was a significant amount of DCE in the headspace gas and relatively insignificant amount of methane. Vinyl chloride was also observed in the gas sample. Comparing these results it is clear that only anaerobic conditions lead to the formation of DCE that was observed in the groundwater of the channel, while indigenous methanogens had relatively less activity. Therefore, it could be mentioned that during the recent study natural methanogenic degradation of TCE to methane and CO_2 failed to occur in the channel soil. At this point, it is, however, unconfirmed as to what could be the source of the methanogenic degradation of TCE in groundwater of the system during the earlier study.

CONCLUSIONS

Biodegradation studies of TCE carried out in the chamber during 1993 showed that about 17% of TCE was mineralized to chloride, methane, and other harmless end products. Estimates of volatilization rates indicated that at least 0.3 mmoles/day of TCE was lost to the headspace of the chamber. Significant amounts of methane and no other chlorinated intermediates of biodegradation were observed in the groundwater.

During the 1994 study, the concentration trends of TCE remained unchanged in the channel, when compared to earlier studies. However, no methane due to methanogenic biodegradation was found. Moreover, chlorinated intermediates, mostly 1,2 cis-DCE, were observed in the groundwater and soil gas of the chamber. This observation was found to be consistent with the mesocosm

studies performed separately. Acetate or phenol recharging to the system, in order to trigger methanogenic populations, were unsuccessful. Overall, the extent of TCE biodegradation was relatively lower during the recent study. This was confirmed by the lower amounts of chloride accumulation after the recent study. It is clear from the above conclusions that the results purport the need for more research in order to unravel the mechanism of stimulating and sustaining methanogenic degradation of TCE and the role of plants in this mechanism.

ACKNOWLEDGMENTS

This research was partially supported by the U.S. EPA under assistance agreements R-815709 and R-819653 to the Great Plains-Rocky Mountain Hazardous Substance Research Center for regions 7 and 8 under project 90-13 and an EPA grant (CR81-7790-01-1) to Drs. Fateley and Hammaker. It has not been submitted to the EPA for peer review and, therefore, may not necessarily reflect views of the agency and no official endorsement should be inferred. The U.S. Department of Energy, Office of Environmental Restoration and Waste management, Office of Technology Development and the Center for Hazardous Substance Research also provided partial funding. We thank V.P. Visser and R. Hoffmann for FT-IR gas phase measurements.

LITERATURE CITED

(1) Muralidharan, N., L.C. Davis, and L. E. Erickson, "Fate of Volatile Chlorinated Organic Compounds in a Laboratory Chamber with Alfalfa Plants," Environ. Sci. Technol., 29, 2437-2444 (1995).

(2) Anderson, T.A., E.A. Guthrie, and B.T. Walton, "Bioremediation in the Rhizosphere," Environ. Sci. Technol., 27, 2630-2636 (1993).

(3) Davis, L.C., M.K. Banks, A.P. Schwab, N. Muralidharan, and L.E. Erickson, "Plant Based-Bioremediation," In Bioremediation: Principles and Practice, Eds. S.K. Sikdar and R.L. Irvine, Technomic (in press) (1995).

(4) Erickson, L.E., M.K. Banks, L.C. Davis, A.P. Schwab, N. Muralidharan, K. Reilley, and J.C. Tracy, "Using Vegetation to Enhance *In situ* Bioremediation," Environ. Progress, 13, 226-231 (1994).

(5) Muralidharan, N., R.M. Green, L.C. Davis, and L.E. Erickson, "A Laboratory study of the Fate of Trichloroethylene and 1,1,1-Trichloroethane in the Presence of Alfalfa Plants," pp 110-118, Proceedings of the 24th Annual Biochemical Engineering Symposium, Ed. Robert H. Davis, Estes Park, Colorado, 1994.

(6) Muralidharan, N., "Experimental and Modeling studies of Bioremediation in the Presence of Alfalfa Plants," M.S. Thesis, Kansas State University, Manhattan, KS, 1994.

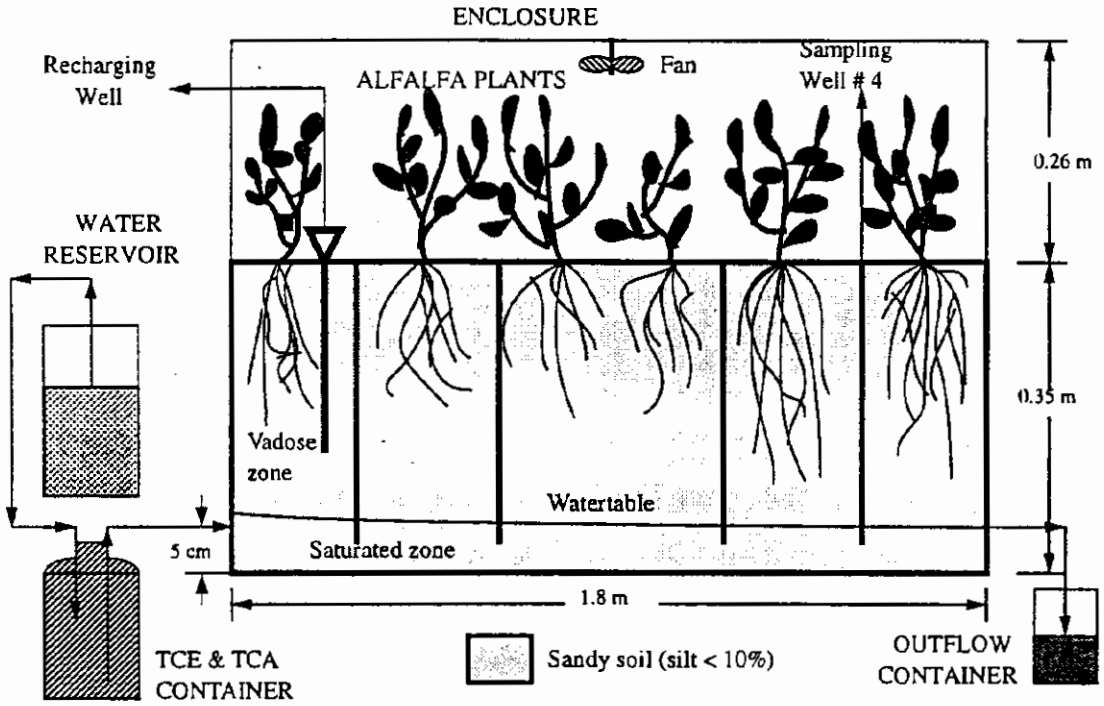

Figure 1. Schematic view of the axially extended experimental setup.

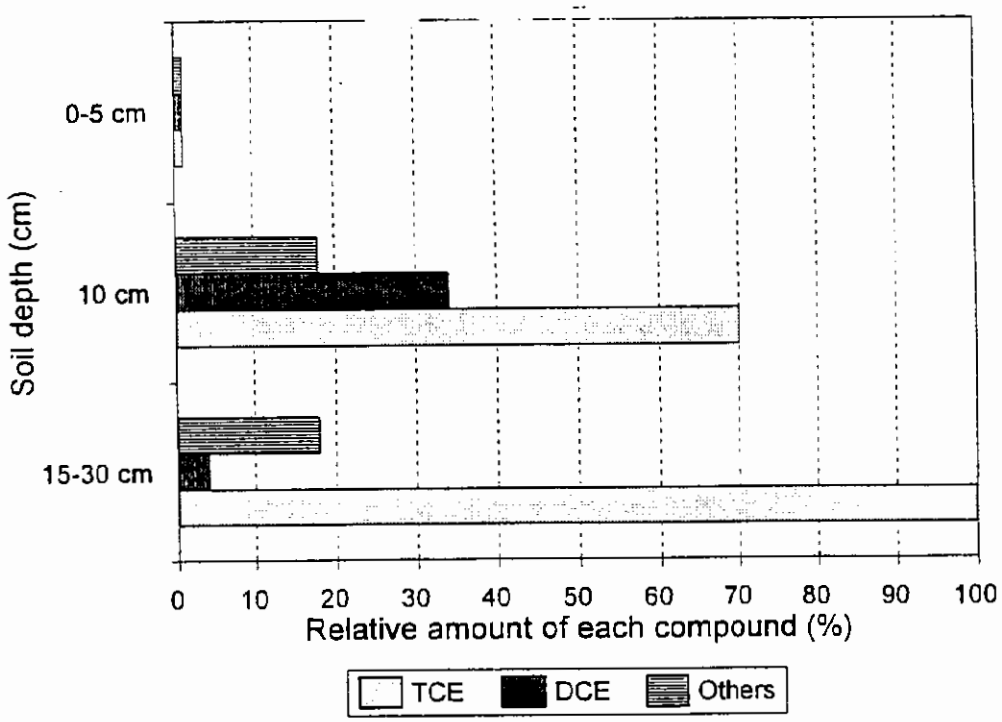

Figure 2. Qualitative detection of compounds following acetate recharging based on TCE peak height at greater than 15 cm being 100%. Others include methane, ethane, ethylene, and vinyl chloride.

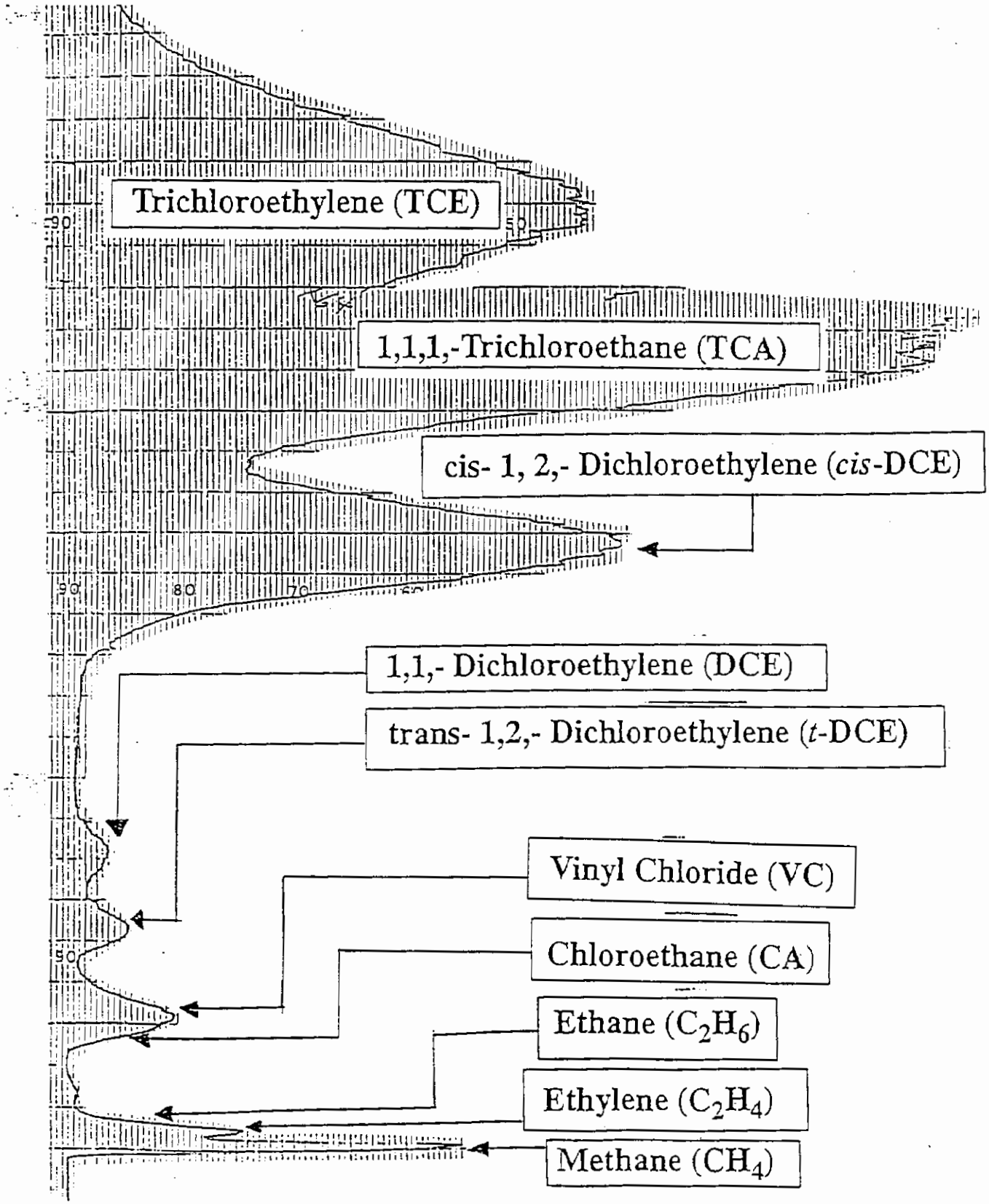

Figure 3. The compounds seen in the headspace of the mesocosm using gas chromatography.

SURFACTANT-ENHANCED REMEDIATION OF A NON-AQUEOUS PHASE CONTAMINANT IN SOIL

S.K. Santharam, L.E. Erickson, and L.T. Fan

Department of Chemical Engineering
Kansas State University
Manhattan, KS 66506-5102

INTRODUCTION

Remediation of sites contaminated with non-aqueous phase (NAP) organic compounds depends primarily on solubilization in pump-and-treat applications. Some of the contaminants, such as polycyclic aromatic hydrocarbons (PAHs), are sparingly soluble in water and tend to form a non-aqueous phase; these compounds also adsorb extensively to soil. Thus, it is very difficult to remediate such sites. In this work, an innovative remediation scheme is proposed to treat non-aqueous phase contaminants. The contaminant in the aquifer is flushed with a surfactant solution to a vegetated region and mineralized.

DESCRIPTION OF THE REMEDIATION SYSTEM

A contaminated aquifer in the saturated zone comprises the following phases: the aqueous phase, the NAP, and the soil solids. In conventional pump-and-treat systems, water is pumped through the aquifer to solubilize the contaminant. In the present work, a surfactant solution is flushed through the aquifer contaminated with a NAP compound. After solubilization, the solution is irrigated onto a vegetated zone where the contaminant is allowed to mineralize. The mineralization activity is assumed to take place in the first 30 cm of the soil. The vegetated zone is unsaturated; therefore, it comprises air, the aqueous phase, roots, and soil solids.

FLUSHING MODEL FOR THE AQUIFER

An equilibrium flushing model has been developed by Gandhi *et al.* (1994). The model assumes that the transport in the aquifer is such that phase and chemical equilibria prevail within the zone where flushing is applied. This includes sorption to solid surfaces, dissolution of the NAP, and biochemical oxidation; biodegradation is limited by the amount of oxygen supplied with each flushing. The model has been extended here to include the effects of surfactant on the flushing process.

First flushing

Initially, the total concentration of the contaminant in the aquifer is the sum of the contaminant present in the aqueous phase, adsorbed to soil organic matter, and existing in the non-aqueous phase; hence,

$$C_T = C_W \varepsilon_{W,1} + K_d C_W \rho_B + \rho_N \varepsilon_{N,1} \qquad (1)$$

As long as the NAP is present, the concentration of the contaminant in the aqueous phase, C_W,

equals its solubility in water, C_{sat}; when surfactant is also present, the solubility increases to C^*_W. In the first flushing, the aqueous phase saturated with the contaminant is flushed out through extraction wells. Thus, the mass fraction of the contaminant removed from the aquifer is given by

$$MF_{O,1} = \frac{C_W \varepsilon_{W,1}}{C_W \varepsilon_{W,1} + K_d C_W \rho_B + \rho_N \varepsilon_{N,1}} \tag{2}$$

The mass fraction remaining is

$$MF_{R,1} = 1 - MF_{O,1} \tag{3}$$

Second flushing

Contaminant

In the second flushing, the surfactant solution is pumped into the aquifer. A surfactant molecule consists of a hydrophilic head part and a hydrophobic tail part. When the concentration of surfactant in water exceeds a specific value, termed the critical micelle concentration or CMC, the molecules form clusters, i.e., micelles, with a strong hydrophobic nucleus, which tend to attract contaminant molecules. In soil-water systems, this results in a high concentration of the contaminant in the aqueous phase including micelles, C^*_W, and a low concentration of the contaminant adsorbed to soil (Liu *et al.*, 1991). As a result, the equilibrium partition coefficient for adsorption of contaminant to soil is reduced to $K_{d,surf}$.

The decrease in the aqueous concentration of contaminant due to biodegradation causes further dissolution of the NAP; the process continues until oxygen is completely consumed. The aqueous phase saturated with the contaminant is transported out of the aquifer through extraction wells. The decrease in the contaminant concentration attributable to biodegradation can be calculated from the stoichiometry of mineralization. The NAP blobs shrink due to the transfer of the contaminant into the aqueous phase. The mass balance for the contaminant after the second flushing is as follows:

$$K_d C_W \rho_B + \rho_N \varepsilon_{N,1} = K_{d,surf} C^*_W \rho_B + \rho_N \varepsilon_{N,2} + C^*_W \varepsilon_{W,2} + (S_o f / Y)\, \varepsilon_{W,1} \tag{4}$$

The left-hand side of this equation represents the total amount of contaminant present after the first flushing; and the right-hand side, the distribution of the contaminant after the second flushing. The porosity changes due to the dissolution of a fraction of the contaminant from the NAP, i.e., $\varepsilon_{N,2} < \varepsilon_{N,1}$ and $\varepsilon_{W,2} > \varepsilon_{W,1}$. When air, pure oxygen, or hydrogen peroxide is supplied to the aqueous surfactant solution pumped into the aquifer, the concentration of oxygen attains a value of 8 mg/L, 40 mg/L, or 100 mg/L, respectively. Since both the contaminant and surfactant are assumed to be simultaneously biodegraded, the fraction, f, is defined to indicate the proportion of oxygen consumed for the oxidation of contaminant.

For the i-th flushing, the total porosity is the sum of the NAP porosity and the water-phase

porosity, i.e.,

$$\varepsilon_T = \varepsilon_{N,i} + \varepsilon_{W,i} \tag{5}$$

By substituting i=1 and 2 into Equation (5) and combining the resultant expressions with Equation (4), the new porosity of the aqueous phase is obtained as

$$\varepsilon_{W,2} = \varepsilon_{W,1} \frac{[1 + (S_o f/Y\rho_N)]}{[1 - (C^*_W/\rho_N)]} + \frac{[K_{d,surf}C^*_W - K_d C_W]\rho_B}{[1 - (C^*_W/\rho_N)]\rho_N} \tag{6}$$

The amount of contaminant adsorbed to soil in the presence of surfactant ($K_{d,surf}C^*_W\rho_B$) is different from that in the absence of surfactant ($K_dC_W\rho_B$). This also contributes to the difference in the water phase porosity indicated by the second term in the right-hand side of Equation (6). Since the surfactant continues to enter, this term vanishes from the third flushing onwards.

The fraction of the contaminant removed in the second flushing is obtained by dividing the sum of the amount of the contaminant solubilized in the surfactant solution and the amount biodegraded with the total amount present after the first flushing, i.e.,

$$MF_{O,2} = \frac{C^*_W\varepsilon_{W,2} + (S_o f/Y)\varepsilon_{W,1}}{K_d C_W \rho_B + \rho_N \varepsilon_{N,1}} \tag{7}$$

Naturally, the mass fraction of the contaminant remaining in the aquifer after the second flushing is

$$MF_{R,2} = (1 - MF_{O,2})\, MF_{R,1} \tag{8}$$

Surfactant

As mentioned earlier, the surfactant enters the aquifer from the second flushing onwards. A portion of the total surfactant entering is adsorbed to soil; another portion is biodegraded; and the remainder leaves the aquifer. The mass balance for the surfactant, therefore, can be written as follows:

$$\varepsilon_{W,1}C_{u,a} = K_u C_{u,2}\rho_B + [S_o(1-f)/Y']\varepsilon_{W,1} + \varepsilon_{W,2}C_{u,2} \tag{9}$$

The concentration of the surfactant in the solution exiting from the aquifer is obtained from the above equation as

$$C_{u,2} = \frac{\varepsilon_{W,1}C_{u,a} - [S_o(1-f)/Y']\varepsilon_{W,1}}{\varepsilon_{W,2} + K_u\rho_B} \tag{10}$$

Flushings when NAP is present (3<P<Q)

Contaminant

The above treatment is applicable to subsequent flushings until the NAP disappears at the Q-th flushing. The NAP porosity, therefore, becomes zero, and the aqueous phase porosity equals

the total porosity in the Q-th flushing, i.e.,

$$\varepsilon_{N,Q} = 0 \quad \text{and} \quad \varepsilon_{W,Q} = \varepsilon_T \tag{11}$$

The general equations can be obtained for the P-th flushing between the third and Q-th, based on the equations and concepts presented above; they are given elsewhere (Santharam, 1996).

Q-th flushing

After the disappearance of the NAP, the concentration of the contaminant in the aqueous solution decreases; this is governed by the extent of biodegradation and sorption. The aqueous phase concentration is obtained from the following mass balance for the Q-th flushing.

$$K_{d,\,surf} C^*_{W,Q-1} \rho_B + \rho_N \varepsilon_{N,Q-1}$$

$$= K_{d,\,surf} C^*_{W,Q} \rho_B + C^*_{W,Q} \varepsilon_T + (S_o f/Y)\, \varepsilon_{W,Q-1} \tag{12}$$

The subscript, Q, is appended to the aqueous phase concentration of the contaminant to denote that the value varies from flushing to flushing. Solving Equation (12) for $C^*_{W,Q}$ yields

$$C^*_{W,Q} = \frac{K_{d,\,surf} C^*_{W,Q-1} \rho_B + \rho_N \varepsilon_{N,Q-1} - (S_o f/Y)\, \varepsilon_{W,Q-1}}{K_{d,\,surf} \rho_B + \varepsilon_T} \tag{13}$$

Flushings after disappearance of NAP (Z>Q)

Contaminant

The equations for this case are similar to those presented above; however, the NAP term, ε_N, is absent. When the contaminant concentration, $C^*_{W,Z}$, reaches the desired value in the aquifer, the flushings are stopped.

Surfactant

In some instances, the surfactant may be undesirable if present in groundwater, and hence, its concentration should be reduced. Once the NAP disappears, therefore, no surfactant is added in the solution entering the aquifer. For the Z-th flushing, the mass balance equation becomes

$$K_u C_{u,Z-1} \rho_B = \varepsilon_T C_{u,Z} + [S_o (1-f)/Y'] \varepsilon_T + K_u C_{u,Z} \rho_B \tag{14}$$

and thus, the concentration in the exit stream is

$$C_{u,Z} = \frac{K_u C_{u,Z-1} \rho_B - [S_o (1-f)/Y'] \varepsilon_T}{\varepsilon_T + K_u \rho_B} \tag{15}$$

RHIZOSPHERE BIODEGRADATION MODEL

The solution from the aquifer containing the solubilized contaminant and the surfactant is irrigated onto the vegetated zone. The contaminant and surfactant are allowed to mineralize in the root zone of the surface soil.

The details of the model development are given elsewhere (Santharam, 1996). The result-

ant model in terms of mass balances is presented below.

Contaminant

The rate of change of the total mass of the contaminant in the rhizosphere is expressed as

$$\frac{d}{dt}\{C(\theta + R_d R_{cf} + \rho K_d)\}$$

$$= F_R C_{in} - qT_{SCF} C - \frac{\mu_m}{Y_S}(\theta + R_d R_b + \rho K_b) C_b \frac{C}{K_{rsu} + C + C_u + C_r} \qquad (16)$$

The first term on the right-hand side of this equation is the mass flow rate of the contaminant entering the rhizosphere; the second term, the rate of contaminant uptake by plants; and the third term, the rate of biodegradation of the contaminant by the microorganisms. It can be seen from the microbial degradation term that the contaminant, surfactant, and root exudates all provide carbon for the degrading microorganisms.

Microbial Biomass

The rate of change of the total microbial biomass is expressed as

$$\frac{dC_b(\theta + R_d R_b + \rho K_b)}{dt} = F_R C_{b,in} + \frac{\mu_m (C + C_u + C_r) C_b (\theta + R_d R_b + \rho K_b)}{K_{rsu} + C + C_u + C_r}$$

$$- k_{ed} C_b (\theta + R_d R_b + \rho K_b) \qquad (17)$$

The first term on the right-hand side of this equation is the mass flow rate of biomass entering the rhizosphere; the second term, the growth rate; and the third term, the endogenous decay rate.

Root Exudates

The rate of change of the mass of root exudates is expressed as

$$\frac{d}{dt}\{C_r(\theta + R_d R_r + \rho K_r)\}$$

$$= q_r C_{rr} - qT_{SCFr} C_r - \frac{\mu_m}{Y_R}(\theta + R_d R_b + \rho K_b) C_b \frac{C_r}{K_{rsu} + C + C_u + C_r} \qquad (18)$$

The first term on the right-hand side of this equation is the rate of secretion from the roots; the second term, the rate of plant uptake; and the third term, the rate of biodegradation.

Surfactant

The rate of change of the total mass of surfactant in the rhizosphere is expressed as

$$\frac{d}{dt}\{C_u(\theta + R_d R_u + \rho K_u)\}$$

$$= F_R C_{u,in} - qT_{SCFu} C_u - \frac{\mu_m}{Y_U}(\theta + R_d R_b + \rho K_b) C_b \frac{C_u}{K_{rsu} + C + C_u + C_r} \qquad (19)$$

The first term on the right-hand side of this equation is the mass flow rate of surfactant entering the rhizosphere; the second term, the rate of surfactant uptake by plants; and the third term, the rate of biodegradation of surfactant by the microorganisms.

NUMERICAL SIMULATION

For simulation, Equations (16) through (19) are solvable numerically by the fourth-order Runge-Kutta method. Simulation can be conveniently stopped when the aqueous phase concentration of the contaminant in the aquifer attains 0.1 ppm. For demonstration, the volumes of the aquifer and rhizosphere are taken as 10 m^3 and 1000 m^3, respectively. Two pore volumes of the solution from the aquifer are flushed each day to the rhizosphere; this number is typical of field situations. Pyrene is chosen as the model compound. The initial NAP fraction is considered to be 0.5% in the aquifer, which corresponds to 1% saturation of the total porosity since the total porosity of the aquifer is assumed to be 50%. Typically, a surfactant concentration of 1 to 10 g/L is necessary to achieve significant solubilization of PAH compounds (Liu *et al.*, 1991; Tiehm, 1994). The flow rate from the aquifer, F_R, equals the evapotranspiration rate, q, thereby ensuring the constancy of the soil-water content in the rhizosphere; it is assumed to be 25% because the latter zone is unsaturated. Given elsewhere are the values of the constants for the simulation, the initial conditions in the aquifer and rhizosphere, and the concentrations of the material species in the inlet stream to the rhizosphere (Santharam, 1996).

RESULTS AND DISCUSSION

The results shown in Figures 1 through 3 correspond to 1% initial NAP saturation of pyrene equivalent to 63.55 kg in the aquifer volume considered. In Figure 1, the mass fraction of pyrene remaining, the fraction biodegraded in the aquifer, and the fraction flushed from the aquifer are plotted against the number of flushings. In Figure 1(a), the oxygen concentration is 8 mg/L corresponding to the aqueous solubility of oxygen in air. Note that only 12% of the pyrene is biodegraded and the remaining 88% is flushed out. In this case, the number of flushings, Q, required for the disappearance of the NAP pyrene, is 905, and it takes only 14 additional flushings to attain the contaminant concentration of 0.1 ppm in the aqueous phase. Figure 1(b) shows the effect of oxygen concentration on the number of flushings; increasing the oxygen concentration from 8 to 40 mg/L, by replacing air with pure oxygen, reduces the number of flushings from 919 to 668; the amount of pyrene biodegraded increases three-fold. In this case, Q=662, and merely 6 additional flushings are required to reduce the contaminant concentration from 13.5 ppm to 0.1 ppm.

Figure 2 illustrates the case when surfactant is not present ($C^*_W/ C_W=1$). Owing to its low solubility, only a small quantity (~1%) of pyrene is flushed out of the aquifer. It should be noted that since surfactant is absent, all of the entering oxygen is consumed for pyrene degradation only (f=1.0). Despite this increased oxygen consumption, it takes 274 additional flushings to remove all pyrene when compared to the case of flushing with surfactant solution. Without surfactant, the number of flushings is primarily dependent upon the concentration of oxygen. In this case, Q=927, and it takes 15 additional flushings after the NAP disappears to attain an aqueous phase pyrene concentration of 0.1 ppm.

It is assumed that three different surfactants, A, B and C, enter into the aquifer at concen-

trations of 1, 5 and 10 g/L, respectively; each of them has the same effect on the solubilization of pyrene (C^*_W/ C_W=100). The mass fractions of pyrene entering and subsequently remaining in the rhizosphere is plotted in Figure 3 for the surfactants, A and C; they are based on the amount originally present in the aquifer. It is evident that pyrene is readily biodegraded in the rhizosphere when $C_{u,a}$ =10 g/L (surfactant C); this may be attributable to the increase in the rate of consumption of pyrene by the relatively large rhizosphere microbial community, resulting from the increase in the availability of carbon contributed by the surfactant. In the case of surfactant A, pyrene accumulates in the rhizosphere, and a tailing effect is observed after the influx of the solution to the rhizosphere is stopped; the simulation is terminated when 99% of the inlet pyrene is removed. The mass fraction reaches to about 0.67 because it is based on the total initial amount of pyrene in the aquifer; this means that 67% of the total intial amount of pyrene in the aquifer is flushed out; see Figure 1. The abscissa is time, and therefore, 334 days corresponds to 668 flushings based on two flushings per day.

Numerous simplifying assumptions have been made in developing the proposed model. These assumptions render the model to predict the most optimistic case and thus, should provide a useful upper bound of the efficiency of the surfactant-enhanced pump-and-treat technology.

CONCLUSIONS

An innovative remediation scheme has been proposed for effective treatment of a non-aqueous phase (NAP) contaminant in an aquifer. Since solubility is a major problem associated with the remediation of this contaminant, surfactants are added to the flushing solution to stimulate solubilization and thereby reduce the number of flushings significantly. The solubilized contaminant is irrigated onto a vegetated zone and mineralized. The results reveal that the addition of surfactant can substantially accelerate bioremediation of contaminated sites. Increasing the oxygen concentration facilitates the removal of the organic contaminant. A combination of surfactant-enhanced pump-and-treat and vegetation is a promising and cost-effective scheme for remediation of the NAP contaminant in soil.

NOMENCLATURE

C	Aqueous phase concentration of the contaminant in the rhizosphere (mg/L)
C_b	Aqueous phase concentration of microbial biomass in the rhizosphere (mg/L)
$C_{b,in}$	Microbial biomass concentration in the solution entering the rhizosphere (mg/L)
C_r	Aqueous phase concentration of root exudates in the rhizosphere (mg/L)
C_{sat}	Aqueous phase solubility of the contaminant (mg/L)
C_u	Aqueous phase concentration of surfactant in the rhizosphere (mg/L)
$C_{u,in}$	Surfactant concentration in the solution entering the rhizosphere (mg/L)
$C_{u,a}$	Surfactant concentration in the solution injected into the aquifer (mg/L)
$C_{u,i}$	Surfactant concentration in the solution leaving the aquifer after the i-th flushing (mg/L)
C_w	Aqueous phase concentration of the contaminant in the aquifer (mg/L)
C^*_w	Aqueous phase (including micelles) concentration of the contaminant in the aquifer in the presence of surfactant (mg/L)
f	Fraction of the oxygen consumed for the mineralization of the contaminant

	(dimensionless)
F_R	Flow rate of the solution entering the rhizosphere from the aquifer (1/day)
K_b	Partition coefficient for the adsorption of microbial biomass to soil surfaces (L/mg)
K_d	Partition coefficient for the adsorption of the contaminant to soil surfaces (L/mg)
$K_{d,surf}$	Partition coefficient for the adsorption of the contaminant to soil surfaces in the presence of surfactant (L/mg)
k_{ed}	Decay rate constant for microbial biomass (1/day)
K_r	Partition coefficient for the adsorption of root exudates to soil surfaces (L/mg)
K_{rsu}	Saturation constant associated with the organic substrates, i.e., root exudates, contaminant, and surfactant (mg/L)
K_u	Partition coefficient for the adsorption of the surfactant to soil surfaces (L/mg)
q	Rate of extraction of soil-water by a plant's root system (1/day)
$q_r C_{rr}$	Root exudate loading factor (mg/L day)
R_b	Partition coefficient for the adsorption of microbial biomass to root surfaces (dimensionless)
R_{cf}	Plant's root concentration factor for the contaminant (dimensionless)
R_d	Root density in the soil (L/L)
R_r	Partition coefficient for the adsorption of root exudates to root surfaces (dimensionless)
R_u	Partition coefficient for the adsorption of surfactant to root surfaces (dimensionless)
S_o	Oxygen concentration in the solution entering the aquifer (mg/L)
T_{SCF}	Plant's transpiration stream concentration factor for contaminant (dimensionless)
T_{SCFr}	Plant's transpiration stream concentration factor for root exudates (dimensionless)
T_{SCFu}	Plant's transpiration stream concentration factor for surfactant (dimensionless)
Y_S, Y_R	Observed yield coefficient for microbial growth on contaminant and root exudates, respectively (mg/mg)
Y_U	Observed yield coefficient for microbial growth on surfactant (mg/mg)
Y	Stoichiometric coefficient for the mineralization of the contaminant (mg/mg)
Y'	Stoichiometric coefficient for the mineralization of the surfactant (mg/mg)

Greek

$\varepsilon_{N,i}$	NAP volume fraction after the i-th flushing(L/L)
ε_T	Total porosity of the soil in the aquifer (L/L)
$\varepsilon_{W,i}$	Aqueous phase volume fraction in the aquifer after the i-th flushing(L/L)
μ_m	Maximum specific growth rate (1/day)
ρ	Bulk density of the soil in the rhizosphere (mg/L)
ρ_B	Bulk density of the soil in the aquifer(mg/L)
ρ_N	Density of the NAP contaminant (mg/L)
θ	Soil-water content in the rhizosphere (L/L)

REFERENCES

1. Gandhi, P., L.E. Erickson, and L.T. Fan, "A Simple Method to Study the Effectiveness of Bioremediation Aided, Pump-and-Treat Technology for Aquifers Contaminated by Non-Aqueous Phase Liquids. I. Single Component Systems," Journal of Hazardous Materials, 39, 49-68, 1994.
2. Liu, Z., S. Laha, and R.G. Luthy, "Surfactant Solubilization of Polycyclic Aromatic Hydrocarbon Compounds in Soil-Water Suspensions," Water Science and Technology, 23, 475-485, 1991.
3. Santharam, S.K., "A Modeling Study of the Role of Vegetation and Surfactants in Remediating Soil Contaminated with Polycyclic Aromatic Hydrocarbons," M.S. Thesis, Kansas State University, Manhattan, KS, 1996.
4. Tiehm, A., "Degradation of Polycyclic Aromatic Hydrocarbons in the Presence of Synthetic Surfactants," Applied and Environmental Microbiology, 60:1, 258-263, 1994.

ACKNOWLEDGMENT

This research was partially supported by the U.S. EPA under assistance agreement R-819653 to the Great Plains-Rocky Mountain Hazardous Substance Research Center. It has not been submitted to the EPA for peer review and, therefore, may not necessarily reflect views of the agency and no official endorsement should be inferred. The Center for Hazardous Substance Research also provided partial funding.

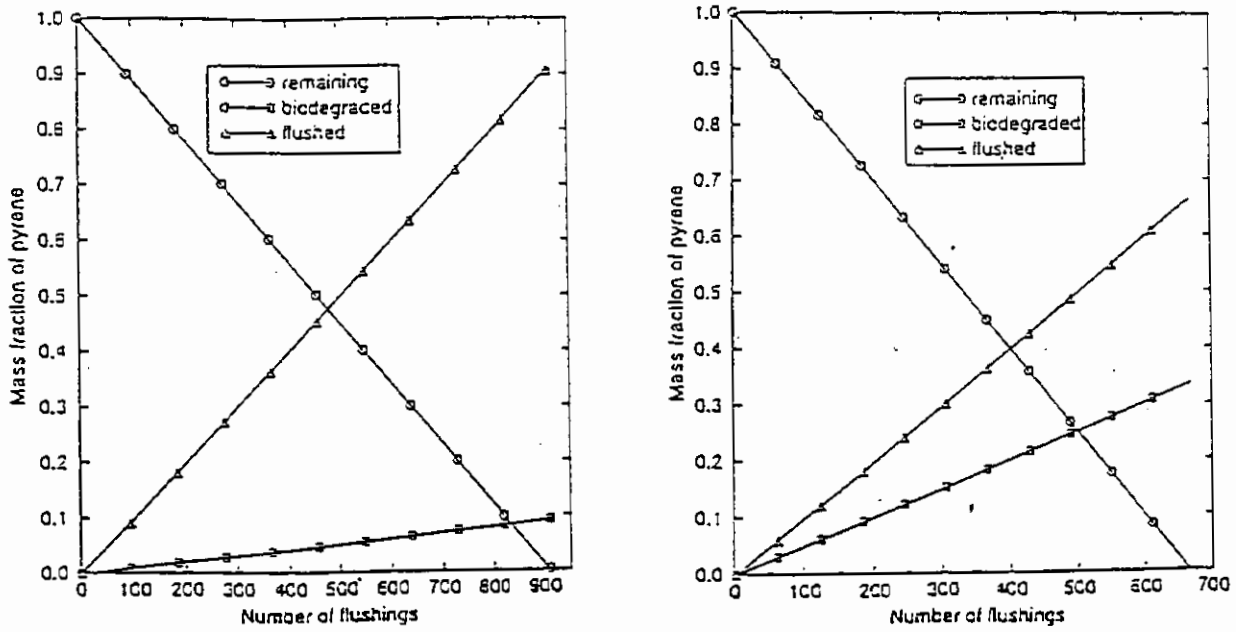

Figure 1. Mass fraction of pyrene remaining in the aquifer, biodegraded in the aquifer, and flushed from the aquifer: (a) S_o=8 mg/L, f=0.5, and C^*_W/C_W=100; (b) S_o=40 mg/L, f=0.5, and C^*_W/C_W=100.

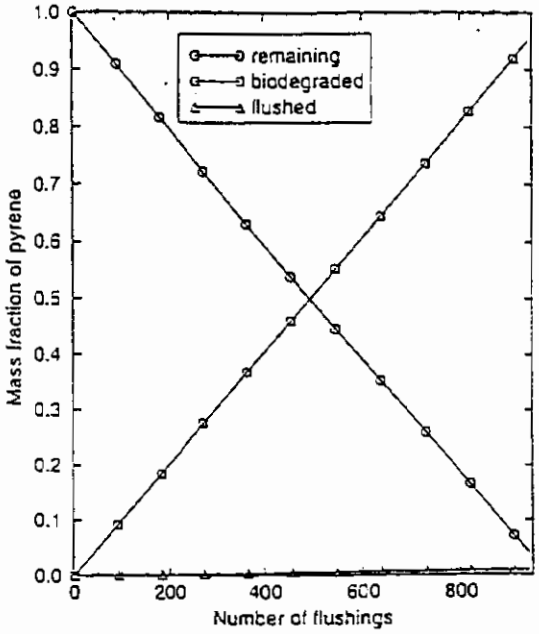

Figure 2. Mass fraction of pyrene remaining in the aquifer, biodegraded in the aquifer, and flushed from the aquifer: S_0=40 mg/L, f=1.0, and C^*_W/C_W=1.

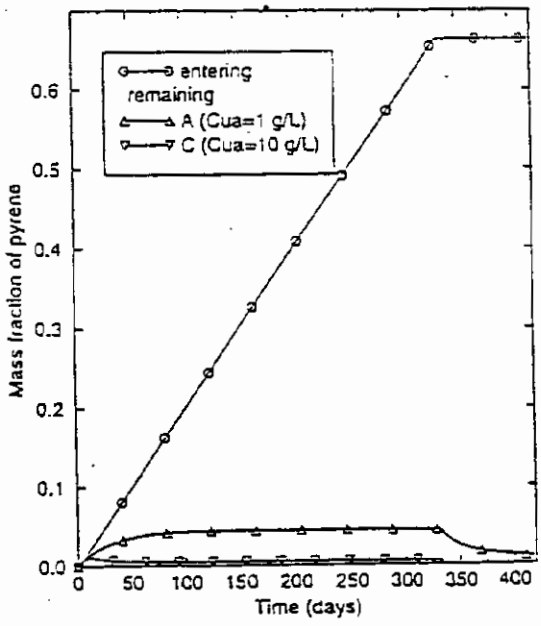

Figure 3. Mass fractions of pyrene entering and subsequently remaining in the rhizosphere for two surfactants, A and C; they are based on the amount originally present in the aquifer: S_0=40 mg/L, f=0.5, and C^*_W/C_W=100.

The Binding of T7 RNA Polymerase to Double-Stranded DNA

Barry Vant-Hull, Larry Gold, and Robert H. Davis
University of Colorado at Boulder

Introduction

The Central Dogma of Molecular Biology (DNA sequences are transcribed into RNA sequences, which are translated into sequences of amino acids to form proteins) has been accepted for over three decades. However, recent advances in our understanding of nucleic acids, especially RNA, have led us to abandon an idea which is implied, though not implicit, in the Central Dogma: that nucleic acids are merely carriers, or "tapes" of information, while proteins assume conformational "shapes," to do such interesting things as catalyze reactions, serve as hormones and antibodies, act as structural supports, etc. It is now known that nucleic acids are also capable of forming interesting structures which allow many functions analogous to proteins, such as reaction catalysis and specific binding to target molecules[1].

Because such capabilities suggest possibilities such as pharmaceuticals and diagnostics, interest in nucleic acid oligomers has risen dramatically over the past decade both academically and industrially. Unfortunately, nucleic acids are very expensive to synthesize either chemically or enzymatically, and both techniques have drawbacks. Chemical synthesis allows a high degree of control over the product, such as base modification at any position (used to protect against nucleases, or to add functionality), but becomes very inefficient for long oligomers. Enzymatic transcription actually becomes more efficient for longer sequences, but modifications are limited by what the polymerase will accept, and transcription requires the added expense of a RNA polymerase and a DNA template[2].

This project originally looked at ways of increasing the efficiency with which the DNA template and the RNA polymerase are used. The RNA polymerase used for this study is a 99 kD monomeric protein from T7 bacteriophage, a virus which infects *E. coli*. The DNA template is chemically synthesized. The DNA template is retained in the reaction vessel for reuse through several transcription reactions by attachment to a solid support[3]. The RNA polymerase is retained by its affinity for the DNA. In the course of investigating the binding of the polymerase to DNA in order to possibly increase its retention, a number of other biological questions have surfaced and have been pursued.

Retention of T7 RNA Polymerase

Background and Theory

Transcription of RNA requires three components: NTPs (nucleotide triphosphates), a DNA template, and RNA polymerase. NTPs consist of the four bases ATP, CTP, GTP, and UTP, which are the building blocks of RNA. The DNA template codes for the RNA sequence, but necessarily includes a non-coding region called a promoter, which the polymerase recognizes. The RNA polymerase is the enzyme which catalyzes the condensation of NTPs into RNA, producing pyrophosphates as a waste product. T7 RNA polymerase is the polymerase of choice, due to its small size, stability, and high activity[4].

Figure 1 schematically describes the transcription process. T7 RNA polymerase first binds to the promoter region of the template. The promoter region is a site that the polymerase recognizes with high specificity, but which does not code for RNA. In the presence of the initiating NTP (GTP), the polymerase melts apart an approximately 15-base region of a double-stranded template, and begins to polymerize the NTPs into RNA. After an initial, abortive phase, in which short, 2 to 8 base RNA oligomers are transcribed, the polymerase moves into the elongation phase, in which NTPs are polymerized into RNA according to the sequence encoded in the DNA template, until the reaction terminates when the RNA polymerase literally runs off the end of the template[4].

The template may be immobilized[3], as shown in Figure 2, in which a biotin molecule, linked to the "top" strand upstream of the promoter, binds to streptavidin, which is attached to a solid support, such as microspheres. Because these microspheres may be separated out by centrifugation or other means, the DNA template may be recovered after a transcription reaction and reused. The affinity of RNA polymerase for the template causes some of it to be retained as well, when the DNA is recovered. Thus, it too may be reused.

Figure 3 illustrates a possible realization of this strategy. After a transcription reaction is complete, the microspheres to which the DNA is immobilized are separated by centrifugation, retaining some of the polymerase as well. The supernatent, which contains the RNA product, unused NTPs, and unbound polymerase, is removed. Fresh buffer containing NTPs is added to resuspend the microspheres, and transcription is reinitiated, without addition of either DNA or polymerase.

This strategy is demonstrated in Figure 4, using two different concentrations of a DNA template for an RNA inhibitor of HIV reverse transcriptase. At 2 hour intervals, 90% of the supernatent was removed and

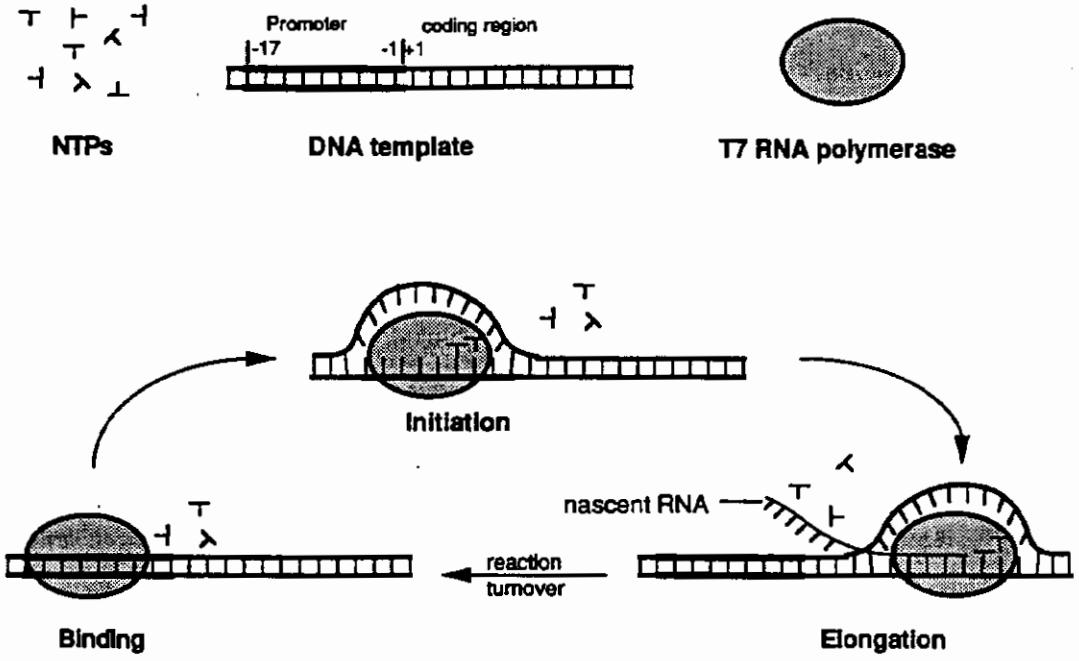

Figure 1 Transcription of RNA by T7 RNA polymerase.

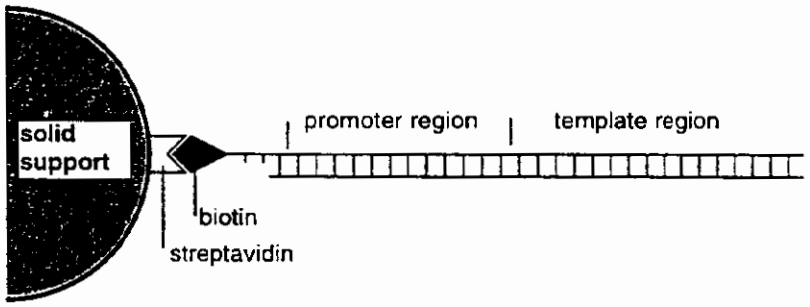

Figure 2 Strategy for immobilization of DNA template.

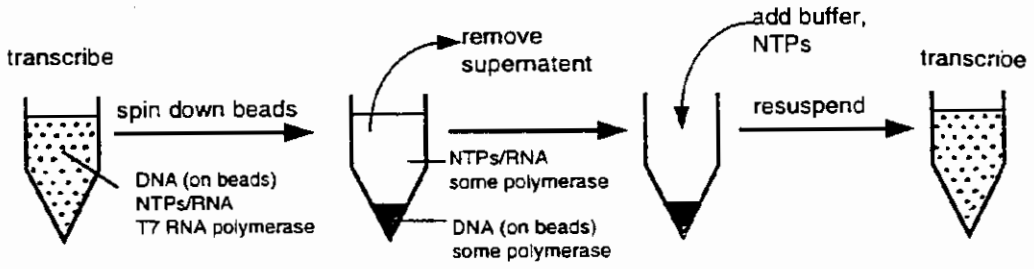

Figure 3 Strategy for repeated rounds of RNA transcription without addition of DNA or polymerase between rounds. The DNA is retained by its immobilization on beads. RNA polymerase is retained through its affinity for the immobilized DNA.

replaced with fresh buffer and NTPs. Though the rates drop, indicating that T7 RNA polymerase is being lost, it is clear that transcription activity is retained through several rounds.

Mathematical Modeling

The following mathematical description is helpful for predicting the behavior of this system. When the NTPs are well in excess of their K_m values, transcription may be described by the simple model below[9]:

$$P + T + NTPs \underset{koff}{\overset{kon}{\rightleftharpoons}} PT + NTPs \xrightarrow{kcat} P + T + RNA \qquad (1)$$

where, *P* = uncomplexed T7 RNA Polymerase, *T* = uncomplexed immobilized DNA Template, and *PT* = the transcriptionally active Polymerase:Template complex.

Since the concentration of NTPs are saturating, the production of RNA may be expressed as

$$\frac{d[RNA]}{dt} = k_{cat}\ [PT]\ . \qquad (2)$$

Because only complexed polymerase is retained in the reaction vessel, the concentration of polymerase:DNA complex in one round becomes the total concentration of polymerase in the following round: $[PT]_n = [P_{tot}]_{n+1}$. Assuming the pseudo-steady-state condition for the complex *PT*, algebraic manipulation of the mass-action equations, implied by equation 1, yields

$$[P_{tot}]_{n+1} = \frac{1}{2}\left([P_{tot}]_n + [T_{tot}] + K_m - \sqrt{([P_{tot}]_n + [T_{tot}] + K_m)^2 - 4[P_{tot}]_n[T_{tot}]}\ \right) \qquad (3)$$

where

$$K_m = (k_{off} + k_{cat}) / k_{on}\ .$$

Test of Model

Figure 5 shows the results of the test of the above model for polymerase retention. Multiple rounds of transcription were performed using the strategy described above, but stopping the reaction before it plateaued in order to see steady-state kinetics. Three different concentrations of immobilized DNA were used with an intial T7 RNA polymerase concentration of 0.4 μM.

The rates from the experiment of Figure 5 were found by least-squares fit, and plotted against round number in Figure 6. The data were fit by the method of least squares, to the model described above using the Solver feature on Microsoft Excel™, in order to find the Michaelis-Menton constant and the reaction rate constant. The result of this fit is displayed as a broken line for clarity. The model appears to fit the data quite well. Though transcriptional activity is retained through several rounds, it is clear that only about half of the polymerase is retained from round to round. It would be desirable to find some way to retain more of the polymerase. Otherwise, the addition of fresh polymerase would be needed between rounds.

Selection of Double-Stranded DNA for Binding to T7 RNA Polymerase

Systematic Evolution of Ligands by EXponential enrichment[5] is a technique which we believed would allow us to find double-stranded DNA sequences which would bind to T7 RNA polymerase with high affinity — thus retaining more polymerase. Figure 7 describes the technique schematically.

A pool of DNA is chemically synthesized which contains a randomized region of bases between two fixed regions, which are necessary for amplification. Double-stranded DNA with high affinity for T7 RNA Polymerase is found by repeated cycles of selection and amplification. Selection of DNA with high affinity for polymerase is achieved by mixing the DNA pool with polymerase, then separating the bound DNA from the unbound by electrophoresing the mixture across a polyacrylamide gel. The mobility of the bound DNA is reduced relative to the unbound DNA. This retarded band of DNA may be excised from the gel, and the DNA eluted and amplified by PCR to generate a pool of DNA enriched for T7 RNA polymerase binders.

After several rounds of SELEX, the pool is cloned and sequenced, generating a set of sequences such as is seen in Figure 8 (these sequences were actually taken from rounds 13 and 14). The underlined sequences represent common sequence motifs. By convention, only one strand of double-stranded DNA is shown, in the 5' to 3' direction. The second strand is understood to run in the opposite direction, and to have a sequence complementary to the one shown (where A pairs with T, and C pairs with G). Thus, when looking for common motifs, the reverse complement of each sequence must be examined as well. For example, compare the double-underlined sequences in clone 76 with clone 102.

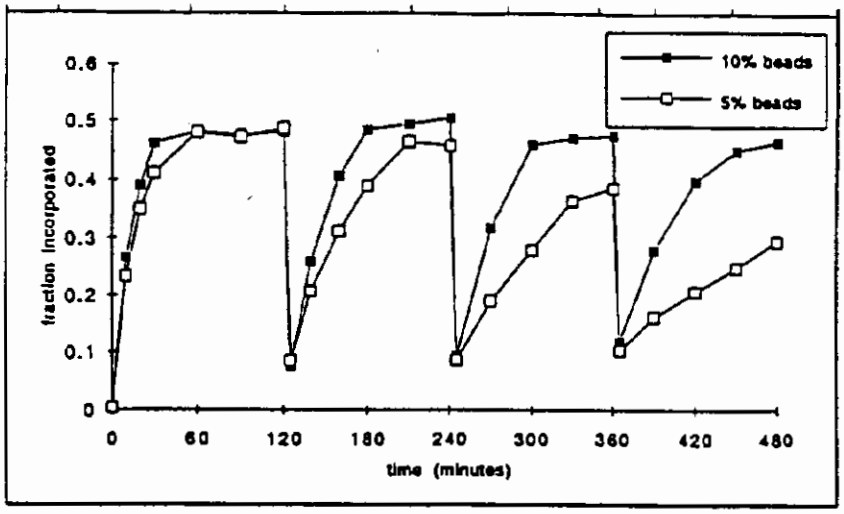

Figure 4 Demonstration of ability to retain T7 RNA polymerase and DNA template through four rounds of transcription. Neither was added after initiating the first reaction.

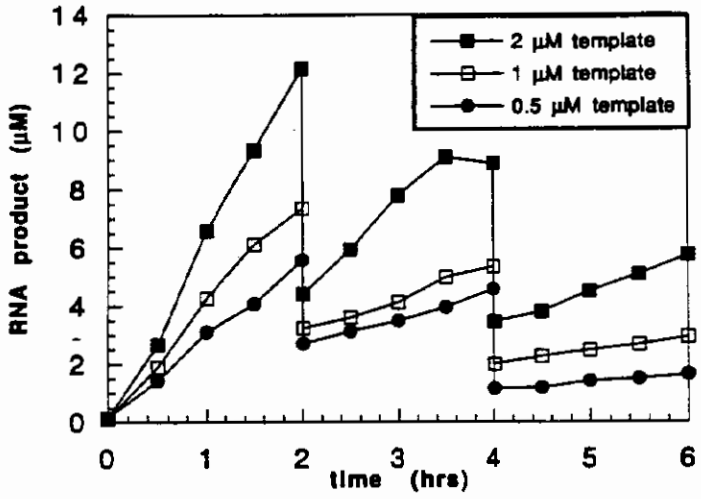

Figure 5 Experiment to test the validity of the mathematical model of polymerase retention, described in the text, over three rounds of transcription. The DNA was immobilized on magnetic microspheres, allowing removal of all the supernatent.

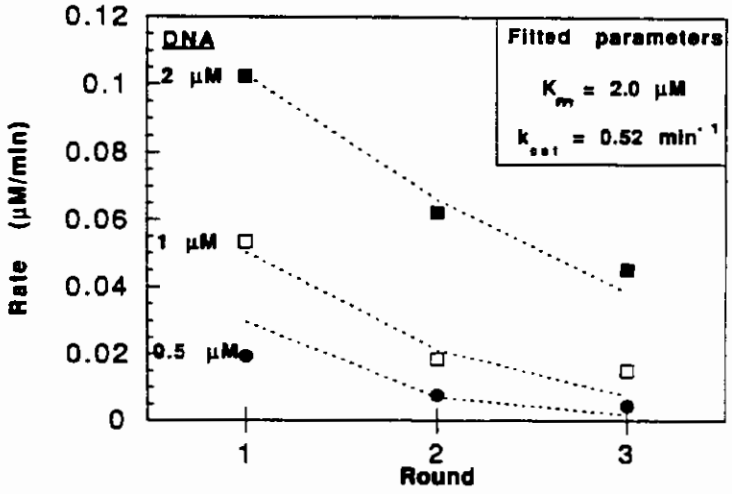

Figure 6 Rates of RNA transcription derived from Figure 5 are plotted against round number. The broken lines represent a least-squares fit to the data according to the model described in the text, in which k_{cat} and K_m are varied.

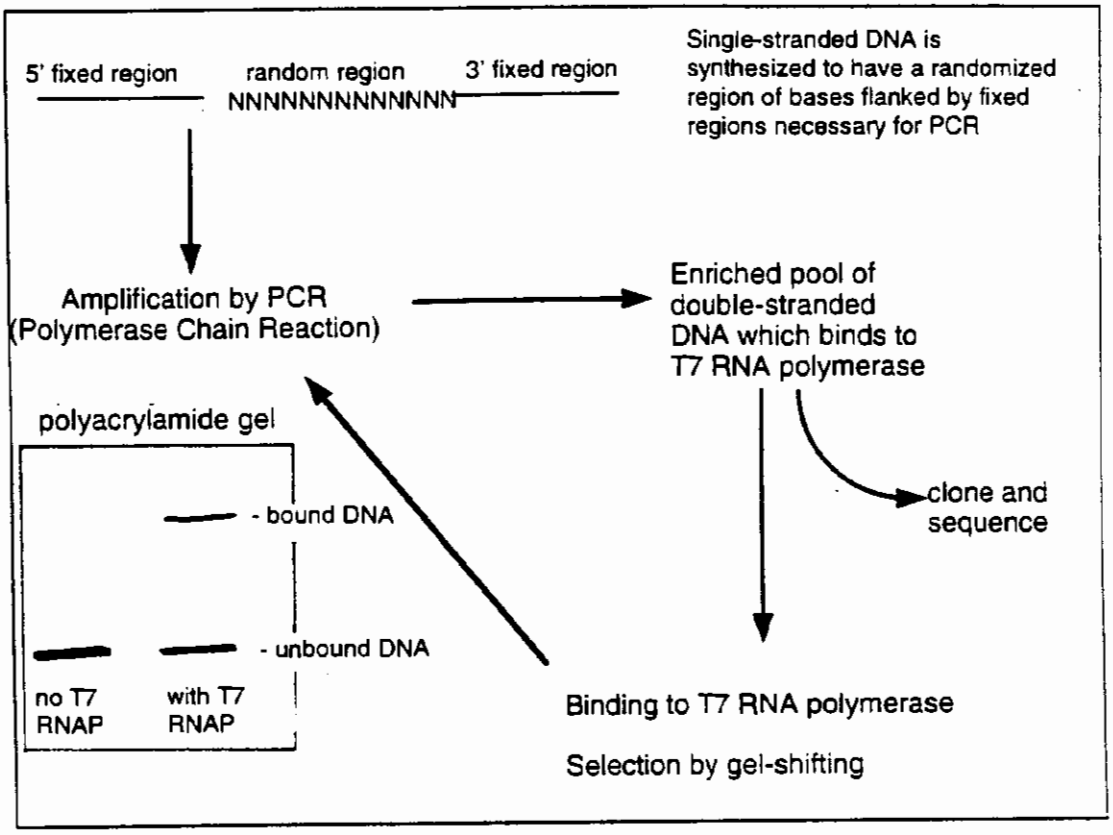

Figure 7 Systematic Evolution of Ligands by EXponential enrichment. Schematic of technique used to find double-stranded DNA sequences which bind with high affinity to T7 RNA polymerase.

	5' fixed region	random region	3' fixed
4>	gaataaacgctcgag	AATTCCGCTGGGCTCCAATAATTGATAGGCCATACCTATCAA	ttcgacagga
6>	aataaacgctcgag	ATTAATTTTAGTACAGTAGTGTGCCTGTCTCCGCCCCCGTG	ttcgacagga
15>	aataaacgctcgag	AACTCATCCTCTTACGACTCACCCCGCCCTACCCACCCGTTG	ttcgacagga
16>	taaacg tcgag	AAAGTATTATCTTAATAAGTGGTCCGTACTTAGATTTTCTAT	ttcgacagag
17>caagaataaacgctcgag		AATCAGTATACCGTCAATTACAGTGTCCTACGACTCACGTGT	ttcgacagga
18>caagaataaacgctcgag		AATTATCACCTTATTATGCAGGGACGCTAGCTGTACTTGGC	ttcgacagga
23>caagaataaacgctcgag		AAGGTCTCGTCCAATCAGAGGTCTCAAAATAAGGTGATATTT	ttcgacagga
27>caagaataaacg tcgag		AACTACCGATTGATAGGTTTTGCCTATTAATCCCCTTTATCA	ttcgacagga
41>caagaataaxcxatcgag		AAACGXGATTGATAGGTAAAACCTATCAATCATTTGTATTCCC	ttxgaca
52>caagaataaacgctcgag		AATACGTGACTTCGGAGGGGGGGTCTGGGGGATCTCCCGTG	ttcgacagga
76>caagaataaacgatcgag		AATAGAGCGCATGACTTCTGAATTACGTGAGTCGTATTAAT	ttcgacagga
79>caagaataaxcxatcgag		AAATACGTGAGTCGTATTAATCCXGTTTTGCTCGTCTAAATG	ttcgacagga
81>caagaataaacgctcgag		AAATTTTATCACCTTGTGATAAAAATTGAAGTGCATTCAATC	ttcgacagga
91>caagaataaacxctcgag		AAACGCGATTGATAGGTAGAACCTATCAATCATTTCTATTCC	ttcgacagga
96>caagaataaacgxtcgag		AACTCACCCTCTTACGACTCACCCGCCCTACCCACCCGTTG	ttcgacagga
98>caagaataaacxatcgag		AATTTAAAAGCTGTAGAGCCTTGGCCTCCTTATCGATTCAC	ttcgacagga
102>aagaataaxcxctcgag		AACGTAGGATATGAAATCTGAAATTAATACGACTCACGTGA	ttxcgacagg
103>aagaataaacgctcgag		AGGGGCTCTGAAGGTACGATTAATAGGTATGACCTATCAAC	ttcgacagga
116>aagaataaacgctcgag		AAAAAAAATCATCTTACACAAGCACCTTATGAGAGCTCTCCC	ttcgacagga
141>aagaataaacgctcgag		AATGGCTATTATACTTTTTATCACCTTATTATGTGATATCCC	ttcgacagga

Figure 8 Example of sequences found after several rounds of selection for affinity for T7 RNA polymerase. The double-underlined sequences are members of Motif I, the single-underlined sequences are members of Motif II, and the dotted underlined sequences are members of Motif III.

Examination of the pool of selected sequences reveals that there are some sequence motifs which show up often, indicating that they have been selected for their affinity for T7 RNA polymerase. The sequence motifs we found are shown in Figure 9.

Characterization of Sequence Motifs

The sequence motifs found should be characterized on the basis of their binding to T7 RNA polymerase, their presence (or absence) and location in both the T7 and *E. coli* genomes, and — regardless of their existence or lack thereof *in vivo* — their biological activity *in vitro*, including the ability to promote, inhibit, or terminate transcription by T7 RNA polymerase.

Affinities for T7 RNA Polymerase

The dissociation constants of the selected motifs were found by binding a vanishingly small amount of radioactively labeled DNA with varying concentrations of T7 RNA polymerase. The binding reactions were filtered through nitrocellulose filters, which bind proteins, but not DNA. The amount of radioactivity retained on the filter is taken to be equivalent to the amount of DNA bound. Plotting the fraction of DNA bound against polymerase concentration yields a characteristic sigmoidal curve, where the dissociation constant is equal to polymerase concentration at the inflection point[10].

The following double-stranded oligos were used to represent the motifs in Figure 10:

Pstop (Motif I) - 5' AAATTAATACGACTCACGTAATTC 3'
Crux (Motif II) - 5' GTCGA GATTGATAGGT AGA ACCTATCAATC GTTCG 3'
Wutzit (Motif III) - 5' GTAA TTATCACCTTATTAT GTAG 3'

The following Kd's were found:	Pstop:	120 ± 14 nM
	Crux:	782 ± 166 nM
	Wutzit:	511 ± 77 nM
	Random Pool:	~10,000 nM

The errors represent one stardard deviation of uncertainty, due to the scatter in the data. In all cases, at least a 10-fold increase in binding over the random pool was achieved.

Genetics of T7 Bacteriophage

In order to decide whether the sequence motifs found above are biologically relevant, it is necessary to gain an understanding of the life cycle of T7 bacteriophage. The diagrams in Figures 11 and 12 were taken directly from Dunn and Studier [1983] (reference 6).

The protein coat of T7 encloses the 39,936 base-pair double-stranded DNA genome of the bacteriophage. All of the approximately 50 genes of T7 are transcribed in the same direction, and by convention this direction is taken to be "left" to "right". The left end of the genome is injected into the *E. coli* first, and it is likely that transcription of the genes is to some extent controlled by the entry of the genome into the bacterium, as the T7 proteins generally appear in order from left to right during infection (Figure 11).

The Class I, or "early" genes are generally transcribed by *E. coli* RNA polymerase, which is inactivated after the synthesis of T7 RNA polymerase. Class II and Class III genes are transcribed by T7 RNA polymerase. There are 17 T7 promoters in the genome — 10 of which are Class II and 5 of which are Class III. The remaining two promoters are known as "replication promoters" and are located at the extreme left and right ends of the genome. They do not transcribe any protein-producing genes (aside, perhaps, from the assumed gene 19.5 - for which no protein has been isolated). They are known to be necessary for the replication of the genome, but it is not clear what roles they play.

The regions where the replication promoters are found are known as the "concatamer junction regions" (see Figure 12). During replication of the genome, T7 genomes are found linked head to tail in long concatamers. Though the concatamer junction regions do not contain genes (aside from gene 19.5), they are somehow necessary for the processing of the genome during replication, and contain structurally interesting sequences such as short repeats, hairpins, cruciform structures, and exact repeats between the left and right ends of the genome.

Motif I - Promoter Fragments

There can be no doubt that Motif I sequences are promoter fragments[6]:

```
                      -21                        +1
wild-type Class III    AAAT TAATACGACTCACTATA GGGAGA
Selected Homology      ARAT TAATACGACTCACGTRW TTY
```

Motif I

```
R15mI(25X)   ATCC TCTTACGACTCACCCCG CCCTAC
c15-41       AAAT TAATACGACTCACGTGA Tttcga
c14-17       AGTG TCCTACGACTCACGTGT ttcgac
c14-76       aaAT TAATACGACTCACGTAA TTCAGA
c14-79       GGAT TAATACGACTCACGTAT TTctcg
c14p1-2      AAAT TAATACGACTCACGTAA Tttcga

homology     ARAT TAATACGACTCACGTRW TTY
```

Motif II

```
13-5*>  tcgagAAACGC   GATTGATAGGT   AGA  ACCTATCAATC   ATTTCTATT
13-27>  gaaCTCTTGAT   TATTGATAGGT   TTT  ACCTATCAATA   CTCGCTttc
13-34>  cgctcgagaaA   GATTGATAGGT   TAT  ACCTATTAATG   GTTAGGACG
13-36>  aTACTATACTC   GA TAATAGG    TAT   CCTATTC      GTTCACGAT
14-41*> tcgagAAACGX   GATTGATAGGT   AAA  ACCTATCAATC   ATTTGTATT
14-4>    GGGCTCCAAT   AATTGATAGGC   CAT  ACCTATCAAtt   cgacaggag
14-27>  tcgaAACTACC   GATTGATAGGT   TTT  GCCTATTAATC   CCCTTTATC
14-103> TCTGAAGGTAC   GATTAATAGGT   ATG  ACCTATCAA C   ttcgacagg
14-73>  AACAGGATTTC   G TTGATAGGT   TTT  AACTATCAATC   CTTTTTxxc
14-88>  tattctatt     gcTTAATAGGT   TTT  A CTATCAAT    actttcgca
14-113> TGCTCTCATAC    ATTGATAGGC   TCT  G CTATTAATC   CTttcgaca
14-114> gAACATGGTTC   GTTTGATAGGT   GCA  GCCTATCAATC   TTCTTACtt
14p1-9> CATCGTCGCAA   GATTGATAGGT   GGG  GCCTATCAATG   ttcgacagg
14p1-13>ATTAAATGCCG   AATTGATAGGT   TTT  ACCTATCAATC   GTACCttcg
14p2-12>AGCCGGCACAT   ACTTGATAGGT   TTC  G CTATCAATC   ttcgacagg

homolgy>              RATTGATAGGT   WWW  RCCTATCAATC
```

Motif III

```
13-18>  GAGAA TTATCACCTTATTAT GCAG
13-20>  ATTTT TTATCACTGTTATAG GAAA
13-23>  GAAAA ATATCACCTTATTTT TGAG
13-25>  GAATT TTATCACCTTATTAT ATCC
13-31>  AAAAA TTATCACCTTAATAT GTGA
13-41>  ACTTT TTATCACCTTATTAT GTGA
13-45>  AGAAT TTATCACCTTAATAA GTAG
14-81>  AAATT TTATCACCTTGTGAT AAAA
14-86>  XATTT TTATCACCTTATTAT ATTX
15- 3>  CAATT TTATCACCTTATTAT GTCA

hcmology> WWW TTATCACCTTATTAT R
```

Figure 9 Alignments and homologies of the three sequence motifs found. Lower case letters represent fixed regions. R = A or G; Y = C or T; W = A or T.

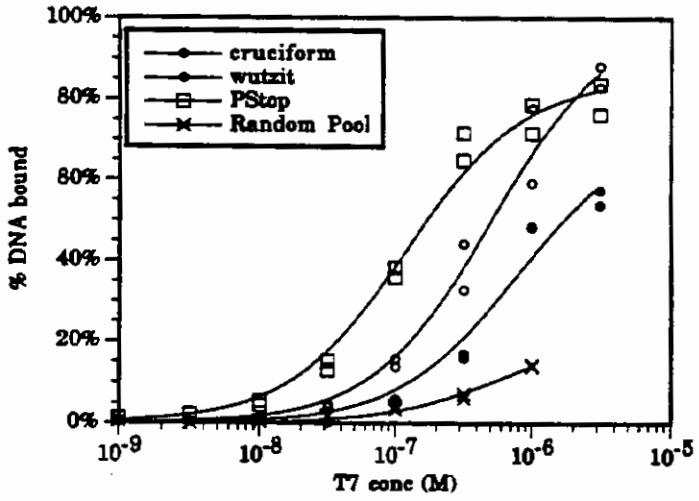

Figure 10 Binding curves for the original random pool, and Motifs I, II, and III.

The underlined sequences here and elsewhere in the text represent regions of homology (similarity). Following conventional notation, R = A or G, Y = C or T, W = A or T.

This result is not surprising — in fact we would be concerned if selection for binding of double-stranded DNA to T7 RNA polymerase did not yield the one sequence motif the polymerase is known to recognize. As it is, it serves as a good check on the technique. It is not clear, however, why the selected sequences should disagree with the wild-type sequences in the downstream region of the promoter.

The affinities of the following promoter-type sequences were examined by nitrocellulose filter binding:

```
PStop:      5'  AAAT TAATACGACTCACGTAA TTC 3'                120±14 nM
Prom:       5'  AAAT TAATACGACTCACTATA CTG 3'                 39± 4 nM
LZ2:        5' CTAGG TAATACGACTCACTATA GCGAC... 3'(53-mer)   454±22 nM
```

Seemingly, both the 5' "AAAT" and the 3' "TATA" have strong effects on binding. It is possible that selection by gel-shifting missed the 3' TATA sequence because binding to this sequence causes a conformational change which further retards the complex. Note that the natural, wild-type promoter sequence has the highest affinity for T7 RNA polymerase. Though it is clear that Motif I sequences (with some modification at the 3' end) are capable of promoting transcription, no such ability was found for either Motif II or Motif III. It is, of course, possible that some sequence modification could lend them such ability.

Motif II - Cruciform DNA?

Palindromic DNA often has biological significance, involved in such functions as cutting by restriction enzymes, crossing-over events during meiosis, and control sites in operons. Because the two arms are capable of base-pairing with eachother, Motif II could be conformed either as fully double-stranded DNA or as a cruciform structure. It is likely that two polymerase molecules would bind the site simultaneously, with protein-protein interactions between the two molecules stabilizing the complex — much in the way of the binding of restriction enzymes.

Motif II shows up in two interesting places — in the control region of an *E. coli* gene[7], and in the right concatamer junction[8]. Whether these occurrences are truly interesting, possessing biological relevance, or merely coincidental, is a question that will have to await further research.

It makes sense that T7 RNA polymerase should somehow regulate the biology of *E. coli*. It is among the first proteins made during infection, just when regulation of the host is of primary importance, and because of strong selective pressure on phages to streamline their genomes, it is likely that many phage proteins will serve dual functions. Unfortunately, it is not at all clear why T7 should wish to regulate this particular gene: a gene for adhesion fimbria, in a strain of *E. coli* that causes diarrhea in pigs in Belgium[7].

Neither is it clear whether the sequence in the concatamer junction shares enough homology to be significant. However, its location makes far more sense, as T7 RNA polymerase is known to interact with the concatamer junction during genome replication[12].

```
Motif II consensus>   GATTGATAGGT TTT ACCTATCAATC
F17 fimbria gene>     GATTGATAGCT TTT ACCTATCAAAT
concatamer junction>     GATAGG  CCAT CCTATCA
```

Motif III - a terminator?

Motif III shows up twice in the T7 genome - in the left concatamer junction, about 300 base pairs downstream of the left replication promoter - and in the right concatamer junction, about 100 base pairs downstream of the right replication promoters. Though neither of these promoters transcribe RNA which codes for protein, there is no doubt that both transcribe RNA, though the function of this RNA is unknown. Since these both transcribe RNA, it is not unreasonable that some sort of transcription terminator should be found downstream. Though none is definitely known at this time, at least one group of investigators found evidence for a terminator which they tentatively placed within ten base-pairs of the Motif III sequence located in the right concatamer junction[11].

```
Motif III consensus>   WWW TTATCACCTTATTAT R
 right concat junct>   TTA GTATCACCTTAACTT AAGG
  left concat junct>   TTT GTTTCACCTTATGTG CCGT
```

Do these sequence motifs inhibit transcription?

Transcription reactions were run in the presence and absence of 10 μM of double-stranded oligos having the sequences of Motif I (PStop), II (Crux), or III (wutzit). The template (LZ2) and polymerase concentrations were 1 μM, and NTP concentrations were 1 mM each. The RNA transcribed is a 30-mer.

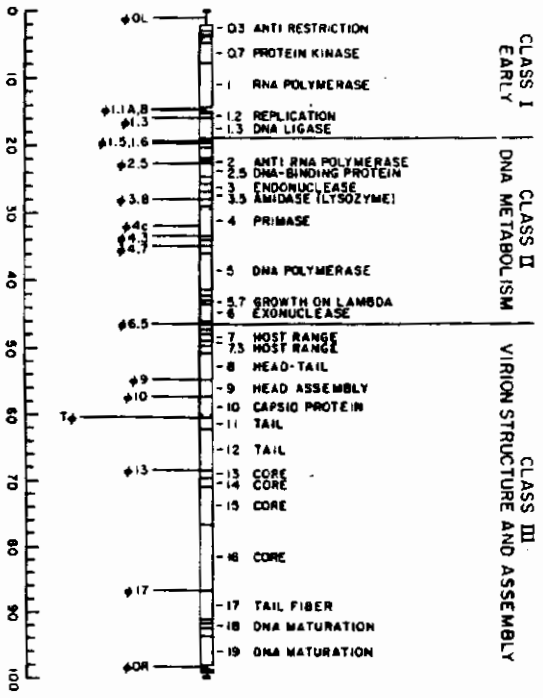

Figure 11 Genetic and physical map of bacteriophage T7 DNA. The positions of terminal repetition (filled boxes), the T7 genes (open boxes) and the promoters (φ) and terminator (Tφ) for T7 RNA polymerase are drawn to scale, according to their position in the nucleotide sequence. Where something is known about gene function, the gene number and function are indicated. (Figure and caption adapted from reference 6).

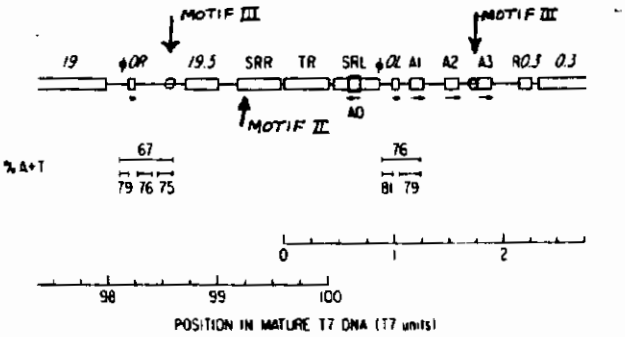

Figure 12 Concatamer junction of bacteriophage T7 DNA. The arrangement of sequence elements between the coding sequences of genes 19 and 0.3 is shown. The locations of the single copy of the terminal repetition (TR) and of the arrays of short, repeated sequences (SRR and SRL) near the right and the left ends of mature T7 DNA are indicated. The leftward minor promoter for *E. coli* RNA polymerase (A0) lies within SRL. The positions of the strong early promoters (A1, A2, and A3) and of the first RNase III cleavage site (R0.3) are also indicated.The φOR and φOL promoters for T7 RNA polymerase, and their associated A/T-rich sequences, apparently serve as origins of replication in the T7 DNA. Arrows indicate the direction of transcription from the promoters. Sites with high sequence homolgy to Motif II and III are indicated. (Figure and caption adapted from reference 6).

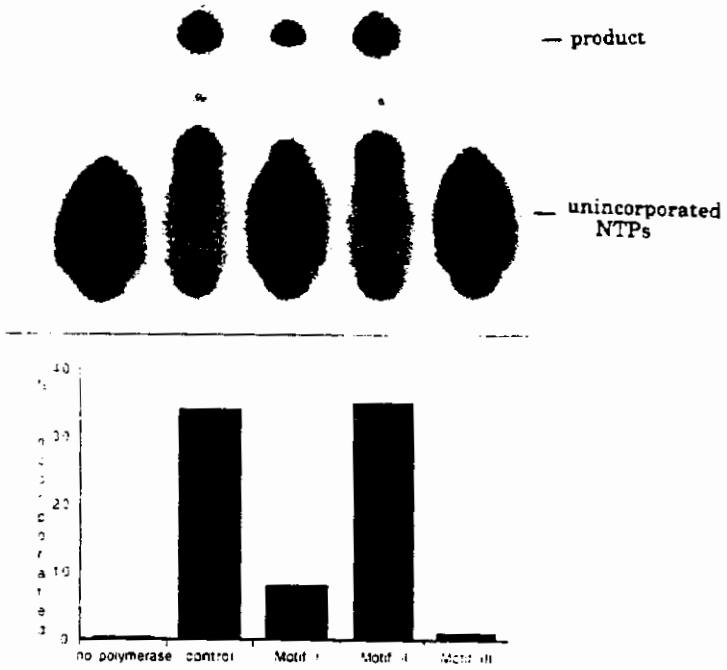

Figure 13 Inhibition of transcription by the three selected sequence motifs, at a concentration of 10 μM.

Reactions were run at 37° for 10 minutes, at which time they were quenched with formamide, heated to 90° for five minutes, then electrophoresed on a 12% denaturing polyacrylamide gel.

As is seen in Figure 13, Motif I, which as a promoter sequence should compete with the promoter on the template, has a significant effect, as expected. Motif II (cruciform structure) has no discernible effect. The truly amazing result is that of Motif III, which nearly completely inhibits transcription. This lends credence to the idea that this sequence serves as a terminator.

Conclusions

The following conclusions may be reasonably drawn from this work so far:

- T7 RNA polymerase may be partially retained in a transcription reactor by its affinity for immobilized DNA template
- The T7 promoter is the double-stranded DNA sequence with the highest affinity for T7 RNA polymerase
- T7 RNA polymerase may also serve a regulatory funtion during T7 infection
- The Motif III sequence strongly inhibits transcription
- T7 RNA polymerase may have up to three binding sites for dsDNA
  1) A catalytic site for transcription
  2) A site for host regulation during infection
  3) A site which serves to inhibit transcription
- Retention of T7 RNA polymerase by an immobilized DNA template could be increased by manipulating the DNA sequence to increase its affinity for the polymerase

All of these conclusions will be investigated in further detail in the months ahead.

This work was supported by NeXstar Pharmaceuticals, Inc., the Whitaker Foundation, the National Institutes of Health, and the W.M. Keck Foundation.

References

1) Gold LM, Polisky B, Uhlenbeck O, Yarus M: **Diversity of Oligonucleotide Function.** *Annual Reviews of Biochemistry* 1995, **64**:763-797.

2) Davis RH: **Large-scale oligoribonucleotide production.** *Current Opinion in Biotechnology* 1995, **6**:213-217.

3) Marble HA, Davis RH: **RNA Transcription from Immobilized DNA Templates.** *Biotechnology Progress* 1995, **11**:393-396.

4) Milligan JF, Uhlenbeck OC: **Synthesis of small RNAs using T7 RNA polymerase.** *Methods in Enzymology* 1989, **180**:51-62.

5) Tuerk C, Gold LM: **Systematic evolution of ligands by exponential enrichment: RNA ligands to bacteriophage T4 DNA polymerase.** *Science* 1990, **249**:505-510.

6) Dunn JJ, Studier FW: **Complete Nucleotide Sequence of Bacteriophage T7 DNA and the Locations of T7 Genetic Elements.** *Journal of Molecular Biology* 1983, **166**:477-535.

7) Lintermans P, Deboeck F, Bertels A, Schlicker C, Vandekerckhove J, Van Damme J, Van Montagu M, De Greve H: **Isolation and Nucleotide Sequence of the F17-A Gene Encoding the Structural Protein of the F17 Fimbriae in Bovin Enterotoxigenic *Escherichia coli*.** *Infection and Immunity* 1988, **56**(6):1475-1484.

8) Chung Y-B, Nardone C, Hinkle DC: **Bacteriophage T7 DNA Packaging: III. A "Hairpin" End Formed on the T7 Concatamers May be an Intermediate in the Processing Reaction.** *Journal of Molecular Biology* 1990, **216**:939-948.

9) Martin CT, Coleman JE: **Kinetic Analysis of T7 RNA Polymerase-Promoter Interactions with Small Synthetic Promoters.** *Biochemistry* 1987, **26**:2690-2696.

10) Tuerk C, Eddy S, Parma D, Gold L: **Autogenous Translational Operator Recognized by Bacteriophage T4 DNA Polymerase.** *Journal of Molecular Biology* 1990, **213**:749-761.

11) Golomb M, Chamberlin M: **A Preliminary Map of the Major Transcription Units Read by T7 RNA Polymerase on the T7 and T3 Bacteriophage Chromosomes.** *Proceedings of the National Academy of Science USA* 1974, **71**(3):760-764.

12) Chung Y-B, Hinkle DC: **Bacteriophage T7 DNA Packaging: II. Analysis of the DNA Sequences requiered for Packaging Using a Plasmid Tranduction Assay.** *Journal of Molecular Biology* 1990, **216**:927-938.

Improvement of RNA Transcription Yield Using a Fed-Batch Enzyme Reactor

Jeffrey A. Kern and Robert H. Davis
Department of Chemical Engineering
University of Colorado
Boulder, CO 80309-0424

Abstract

Exciting discoveries in RNA research have led to increased demands for RNA, both for research purposes and for potential commercial applications. Our goal has been to develop effective strategies for efficient large-scale production of RNA by *in vitro* transcription with T7 RNA polymerase. Due to the high cost of the reaction components (T7 RNA polymerase, DNA template, and nucleotide triphosphates (NTPs)), the focus has been on methods of retaining DNA template and T7 RNA polymerase for repeated use, as well as on determining optimal operating conditions and methods for efficient incorporation of NTPs into full-length RNA product. We have performed experiments to obtain a thorough understanding of the dynamics of *in vitro* transcription reactions, especially of the factors which affect the yield of full-length RNA product. Transcription yields were found to be limited by high ionic strength, byproduct accumulation, and decreasing pH in the reaction. Our results suggest that significant improvements in productivity could be obtained by using a semi-continuous (fed-batch) system in which the nucleotide triphosphates, magnesium, and potassium hydroxide are added as the reaction progresses. Since hydrogen ions are produced at a rate which is proportional to the rate of NTP consumption, the rate of addition of NTPs can be set at a fixed ratio to the rate of addition of potassium hydroxide. Thus, the rate of NTP, magnesium, and KOH addition can be adjusted to maintain optimal pH and reactant concentrations throughout the course of the reaction, resulting in increased productivity of full-length RNA product.

INTRODUCTION

In recent years, remarkable discoveries have been made relating to the properties of RNA molecules. It is now known that certain RNA molecules, referred to as ribozymes, have the ability to catalyze RNA cleavage and joining reactions(1). Another important development is SELEX (Systematic Evolution of Ligands by EXponential enrichment)(2), a technique in which RNA molecules with very high binding affinity for specific proteins, or other targeted molecules(3), are selected for and enriched from a general pool. Based upon these discoveries, there is believed to be great potential for the design of RNA molecules for commercial applications.

The above cited recent developments have resulted in increased demands for the production of RNA molecules. Current methods of RNA production are inefficient and expensive. Specified RNA molecules of limited size (typically less than 40 nucleotides in length) may be produced by organic chemical synthesis (4). The cost of this method increases with the length of the RNA molecule. A more economical approach for the production of larger RNA molecules (greater than 20 nucleotides) is the *in vitro* transcription method described by Milligan and Uhlenbeck (5). As depicted in Figure 1, T7 RNA polymerase catalyzes the formation of RNA molecules via transcription from a DNA template. The coding region of the DNA is preceded by a T7 RNA polymerase promoter region. Transcription is initiated by the binding of T7 RNA polymerase to its promoter. For production of RNA molecules less than about 70 nucleotides, DNA templates constructed from synthetic oligonucleotides are typically used. Only the T7 promoter region, placed immediately upstream of the coding sequence, is required to be double-stranded (6). For longer sequences of RNA, it is desirable to use plasmid DNA templates. The template sequence is

Figure 1: Schematic of RNA transcription. An RNA polymerase enzyme adds nucleotides to the elongating RNA transcript, using the genetic code provided by the DNA template.

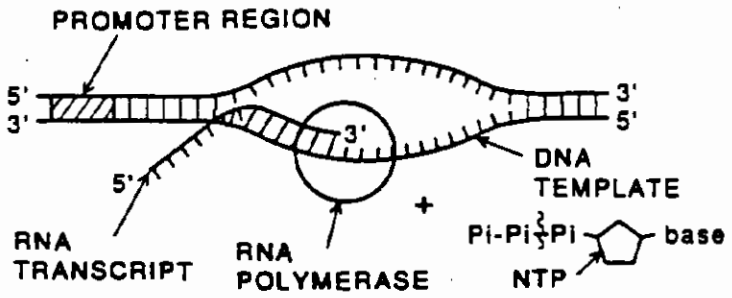

cloned into a plasmid immediately downstream from a T7 promoter. The plasmid is then produced in *E. coli*, purified, and linearized with a restriction enzyme.

Bacteriophage T7 RNA polymerase has become the system of choice for *in vitro* transcription. The gene for this highly efficient 99 kD monomeric enzyme has been cloned into a recombinant vector(7), making it readily available through overexpression in transformed *E. coli*.

In transcription, a large fraction (commonly 80 to 90%) of initiation events do not proceed to full-length product, terminating instead prematurely to produce abortive transcripts. Most abortive transcripts are two to six nucleotides in length. During initiation of transcription at the *lac* UV5 promoter, *E. coli* RNA polymerase cycles to produce oligonucleotides (abortive transcripts) of 2 to 6 nucleotides(8). This synthesis occurs without dissociation of the enzyme from the promoter. Production of a long RNA transcript is then essentially an escape from this cycling reaction. This process, termed abortive cycling, has also been characterized for transcription with T7 RNA polymerase(9). It was found that, after incorporation of eight bases, the unstable initiated complex undergoes a transition to a highly processive ternary complex. The abrupt transition to a more processive complex could be explained by a conformational change in the protein which converts it to an altered form with higher processivity. The relative competition between dissociation and elongation during abortive cycling has been shown to be influenced by the particular sequence of the RNA message(9).

In vitro transcription has commonly been used by researchers as a tool to produce sufficient quantities of RNA for various biochemical studies(5, 10). Current transcription protocols use batch reactions, in which the DNA template, polymerase, and nucleotide triphosphates (NTPs) are incubated in transcription buffer. Upon completion, the RNA is extracted, and the DNA, polymerase, and unincorporated NTPs are discarded. Thus, there is much potential for improvement of this process. One strategy has been to immobilize the DNA template onto agarose beads via biotin-streptavidin linkages. This has been shown to provide a very effective means of retaining the DNA template for repeated use(11). It is also expected that binding of T7 RNA polymerase to the promoter region of the template, along with non-specific binding to other regions of the template, may serve to retain at least a portion of the polymerase along with the DNA template.

The focus of the research presented here is on developing a thorough understanding of the dynamics of *in vitro* transcription which affect the yield of the desired RNA product. The yield is determined by the extent of incorporation of NTPs into RNA transcripts, and the fraction of the transcripts which are of full length, rather than of nonproductive abortive transcripts. Thus, the factors which limit incorporation of NTPs were examined, and methods for minimizing abortive transcription have been sought. Studies to date have indicated that significant improvement in productivity could be achieved through the use of a fed-batch reaction system.

The bulk of the work to date has been performed with DNA template which encodes a dodecamer molecule: 5'-pppGpGpCpGpCpUpUpGpCpGpUpC-3'. This molecule transcribes very efficiently relative to other sequences. This may in part be due to the lack of adenosine residues. The molecule's small size, three-base composition, and efficiency of transcription simplifies analysis; it therefore is a good system for the initial studies. Under optimized conditions, dodecamer yields of as high as 3.6 mg/mL (prior to any purification) have been obtained.

MATERIALS AND METHODS

DNA Templates

The oligonucleotides used in these studies were purchased from Macromolecular Resources (Colorado State Unversity, Fort Collins, CO). As shown below, the annealed oligonucleotides gave a DNA construct which consisted of a single-stranded RNA-coding region (underlined), preceded by the 17-base-pair double-stranded T7 promoter region.

Dodecamer Template

```
5'-AAT  TCT  AAT  ACG  ACT CAC TAT A                    -3'
3'-       GA  TTA  TGC  TGA GTG ATA TCC GCG AAC GCA G -5'
```

Enzymes

T7 RNA polymerase was prepared by Erika Theim, in Steve Schultz' lab at the University of Colorado, from an *Escherichia coli* strain carrying an overproducing plasmid, which has the T7 RNA polymerase gene (7). The enzyme was stored at -20°C in 100 mM NH_4Cl, 50 mM ethylenediaminetetraacetic acid (EDTA), 1 mM dithiothreitol (DTT), 10 mM Tris-HCl (pH 8.6 at 20°C), and 50% (v/v) glycerol. Inorganic pyrophosphatase was purchased from Sigma.

Transcription Reactions

Transcription reactions were performed at 30°C in total volumes of 20 to 30 µL containing 40 mM TRIS[1], pH 8.0; 5 mM DTT; 1 mM spermidine HCl; 0.01% triton X100; and magnesium salts, NTPs, DNA, and T7 RNA polymerase concentrations as indicated in the results. Approximately 0.2 mCurie/mL of γ^{32}P-GTP or α^{32}P-UTP was included to radiolabel the RNA transcripts which formed. Samples were collected from the reactions at various times by removing 2 µl and quenching into 8 µl formamide. Transcription products were separated from unincorporated nucleotides by electrophoresis of the samples on 20% polyacrylamide gels. A Molecular Dynamics PhosphorImager was used to quantify the radiolabeled RNA transcripts and the unincorporated label on the gel. The use of γ^{32}P-GTP results in labeling of the RNA at only the 5' terminus, thus allowing RNA transcript concentrations to be calculated on a molar basis:

$$(1) \qquad [RNA]_j = \frac{C_j * GTP_{init}}{\sum_{i=1}^{I} iC_i}$$

with
- $[RNA]_j$: Concentration of RNA of band j
- C_j: Counts in band j
- GTP_{init}: Initial GTP concentration
- C_i: Total counts from bands of RNA containing i guanosine residues

This method requires a knowledge of the identities of the abortive transcript bands. The identities of most of the bands appearing from transcription with the dodecamer DNA template were

[1] Abbreviations: TRIS, ; DTT, dithiothreitol; PEG, polyethylene glycol; PP_i, inorganic pyrophosphate

determined through examination of abortive transcript patterns from reactions containing various combinations of NTPs.

For analysis of abortive transcription, termination efficiencies (TEs) were calculated for individual transcripts, based on initial rates of formation. The TE of a transcript of n nucleotides was calculated as follows:

(2) $$TE_n = \frac{dRNA_n/dt}{\sum_{i=n}^{N} dRNA_i/dt}$$

Transcription rates were determined from samples taken within the initial rate period of the reaction. The data (obtained from phosphorimaging) were analyzed using Microsoft Excel to calculate transcription rates (by linear regression). Uncertainties were determined, based on 90% confidence intervals.

Manual Fed-Batch Reactions

In fed-batch reactions, additions of an NTP feed solution and a potassium hydroxide feed solution were made at pre-determined times, to a reaction with initial volume of 100 µL. The NTP feed contained the required nucleotide triphosphates, as well as $Mg(OAc)_2$ and T7 transcription buffer. The additions were planned such that, after each addition, the NTP concentrations, magnesium concentrations, and pH, would be returned to their initial values. The timing of additions was determined based upon the expected rate of NTP consumption (from previous batch reaction data) and the desired amount of NTP depletion in-between additions. A Microsoft Excel spreadsheet was used to calculate the required concentrations of components in the feed solutions, the addition volumes, and the timing of additions. Fed-batch reactions were set up and initiated as described in the section above. At the pre-determined addition times, pre-determined volumes of each of the feed solutions were added to the reaction. Since hydrolysis of RNA under basic conditions was a concern, the KOH solution was pipetted onto the side wall of the tube, and the reaction was mixed well by vortexing. Samples were collected throughout the course of the fed-batch reactions. The loss of volume due to sampling was taken into account when calculating the addition volumes.

RESULTS AND DISCUSSION

Understanding the Dynamics of Transcription Reactions

Each nucleotide addition results in the formation of an inorganic pyrophosphate ion ($PP_i \equiv P_2O_7^{4-}$), and the release of a proton:

(3) $$(RNA)_n + MgNTP \leftrightarrow (RNA)_{n+1} + MgP_2O_7^{2-} + H^+$$

The association constants of magnesium to NTPs(13), and to PP_i(14) are such that these components can be assumed to have one Mg^{++} bound under the reaction conditions used. The release of a proton with each nucleotide addition was found to result in a substantial decrease in the pH (Figure 2), with pH in some reactions dropping near the lower limit for T7 RNA polymerase activity(12).

Inorganic pyrophosphate (PP_i) is believed to inhibit transcription. This was tested directly by including 10 mM tetrasodium pyrophosphate in some transcription reactions. An interesting result was the finding that, while PP_i greatly inhibits production of full length product, it has much less inhibitory effect on the production of abortive transcripts (see Figure 3). Thus, as PP_i concentration increases, production of full length RNA is inhibited, but NTPs continue to be incorporated non-productively into abortive transcripts. Therefore, in order to obtain large yields of RNA, it is critical to have some mechanism for the removal of PP_i.

Figure 2: pH change in transcription reactions. Measurements were made using pH paper for five transcription reactions. Reactions A thru E contained 6 U/mL PPase. Initial GTP concentrations were 20 mM for reactions A and B, and 10 mM for reactions C thru F.

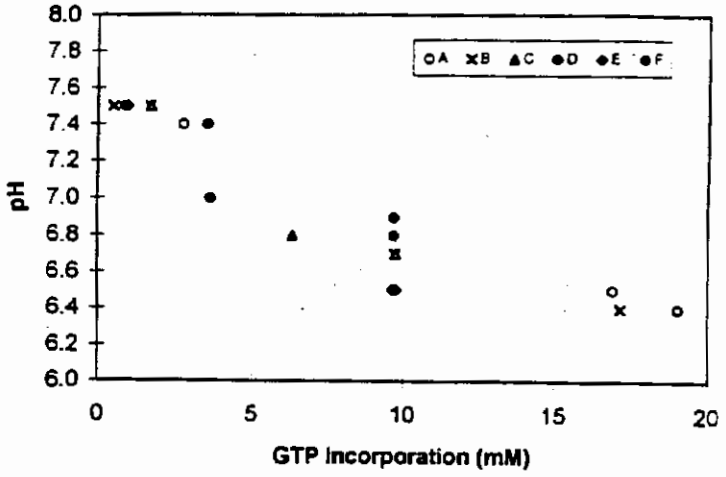

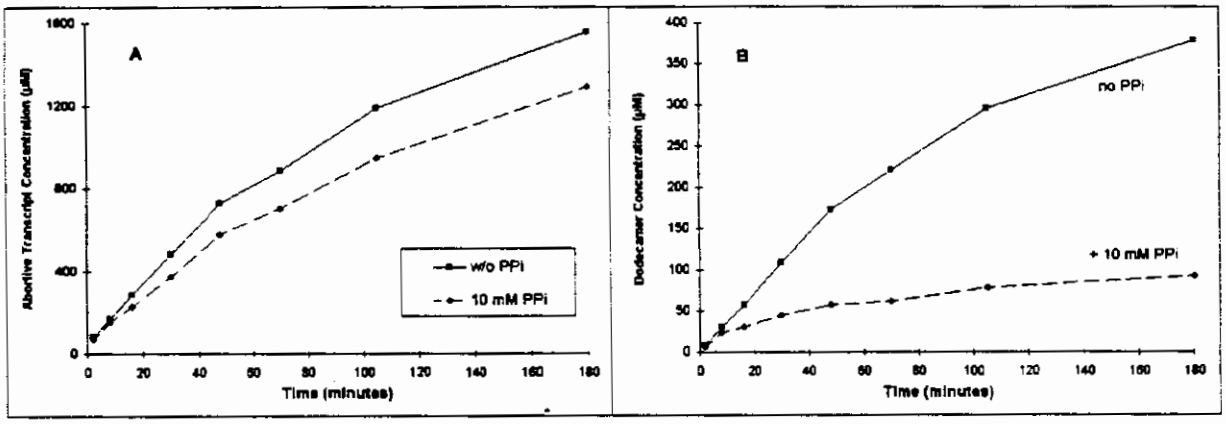

Figure 3: Effect of 10 mM PP_i on transcription. Both transcription reactions were performed with 7 mM each NTP (CTP, GTP, and UTP) and 45 mM $MgCl_2$. (A) production of abortive transcripts. (B) production of full-length product (dodecamer).

One method for achieving PP_i removal is by precipitation with magnesium. Inorganic pyrophosphate combines with magnesium to form an insoluble complex(15) which appears as a white precipitate:

(2) $$Mg^{2+} + MgP_2O_7^{2-} \rightarrow Mg_2P_2O_7$$

The effects of magnesium concentration on transcription rate and yield of RNA were examined as shown in Figure 4. The transcription rate was observed to decrease with increasing magnesium acetate concentration. However, the final yield of full length RNA was higher at the higher magnesium concentrations. These results are interpreted to indicate that, at insufficiently high magnesium concentrations, PP_i eventually builds up in the reaction and limits production of full length RNA. The decreasing rate with increasing $Mg(OAc)_2$ concentration is probably the result of ionic strength effects. These results suggest a potential benefit of adding magnesium in a fed-batch mode. This would take advantage of the higher transcription rate at low $Mg(OAc)_2$ concentration, and yet allow a high yield of full length RNA to be obtained.

Transcription reactions have commonly been performed with magnesium in the form of $MgCl_2$. We have found that T7 RNA polymerase is much less sensitive to increasing $Mg(OAc)_2$ or MgGlutamate concentration than to increasing $MgCl_2$ concentration (Figure 5). The use of acetate instead of chloride allows the use of higher magnesium concentration with less sacrifice of transcription rate.

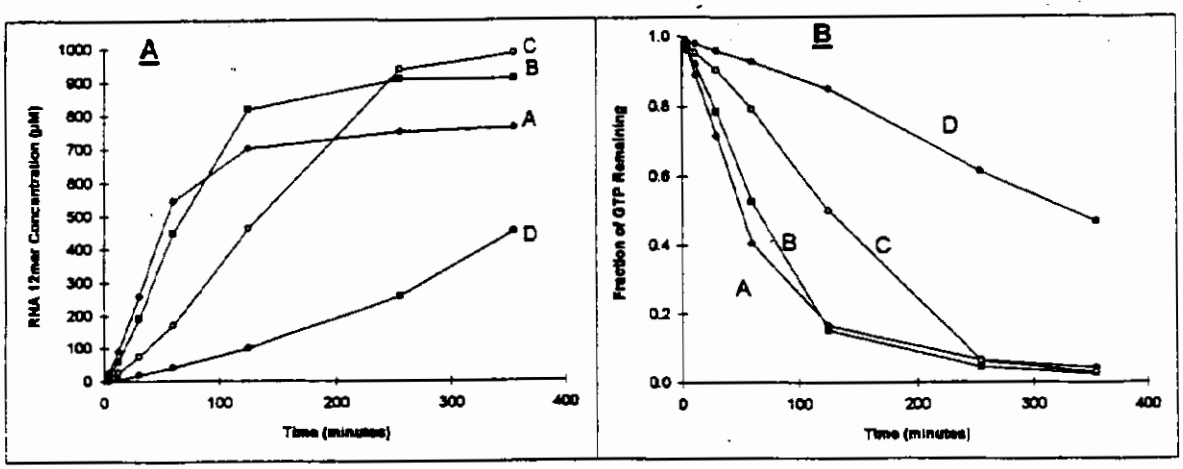

Figure 4: Varying $Mg(OAc)_2$ concentration. Reactions were performed with 10 mM GTP, 8 mM CTP, 6 mM UTP, 0.4 μM T7 RNA polymerase, 0.5 μM dodecamer DNA template, and $Mg(OAc)_2$ concentrations of 44, 60, 84, and 124 mM for reactions A thru D respectively. (A) production of full-length product (dodecamer), (B) depletion of GTP.

Figure 5: $Mg(OAc)_2$ versus $MgCl_2$. Transcription reactions for the production of the 28mer pseudoknot RNA were performed with a stoichiometric ratio of NTPs: 2 mM GTP, 1.2 mM CTP, 1.8 mM ATP, and 0.6 mM UTP; and with $Mg(OAc)_2$ and $MgCl_2$ concentrations varying from 25 mM to 80 mM. The initial rates of UTP incorporation into total RNA transcripts and into 28mer product were measured and plotted versus magnesium concentration as shown.

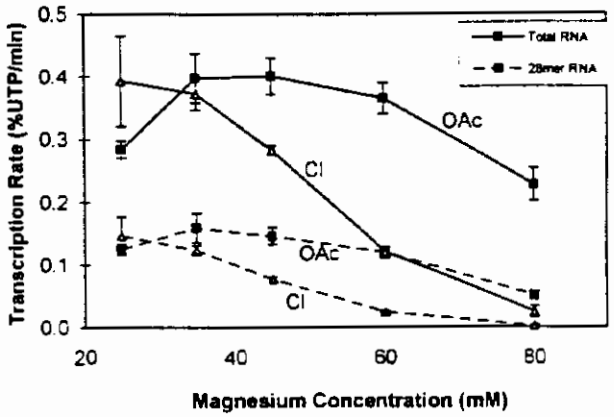

An alternative method for removing inorganic pyrophosphate is the use of inorganic pyrophosphatase (PPase), an enzyme which hydrolyzes pyrophosphate to phosphate:

(3) $$MgP_2O_7^{2-} + H_2O \xleftrightarrow{PPase} 2HPO_4^{2-} + Mg^{2+}$$

We have found that PPase effectively removes PP_i from the reaction as it forms. A potential advantage of using PPase is that it reduces the requirement for magnesium, thus avoiding high ionic strengths which lower the transcription rate.

Abortive Transcription

The parameters which seem to have the most effect on abortive transcription are the concentrations of individual NTPs. Detailed analysis of the effects of varying individual NTP concentrations on abortive transcription from the dodecamer DNA template was performed as shown in Figure 6. In general, formation of individual abortive transcripts was reduced with increasing concentration of the NTP which follows in the sequence. In addition, at high NTP concentrations, there was an overall increase in abortive transcript formation with increasing NTP concentration. The total effect of UTP and CTP concentration on abortive transcription is shown in Figure 7. With additional experiments (not shown here), optimal NTP concentrations for the dodecamer were determined to be approximately 6 mM GTP, 2 mM CTP, and 6 mM UTP. At these optimal NTP concentrations, as much as 60% of the NTPs are incorporated into full-

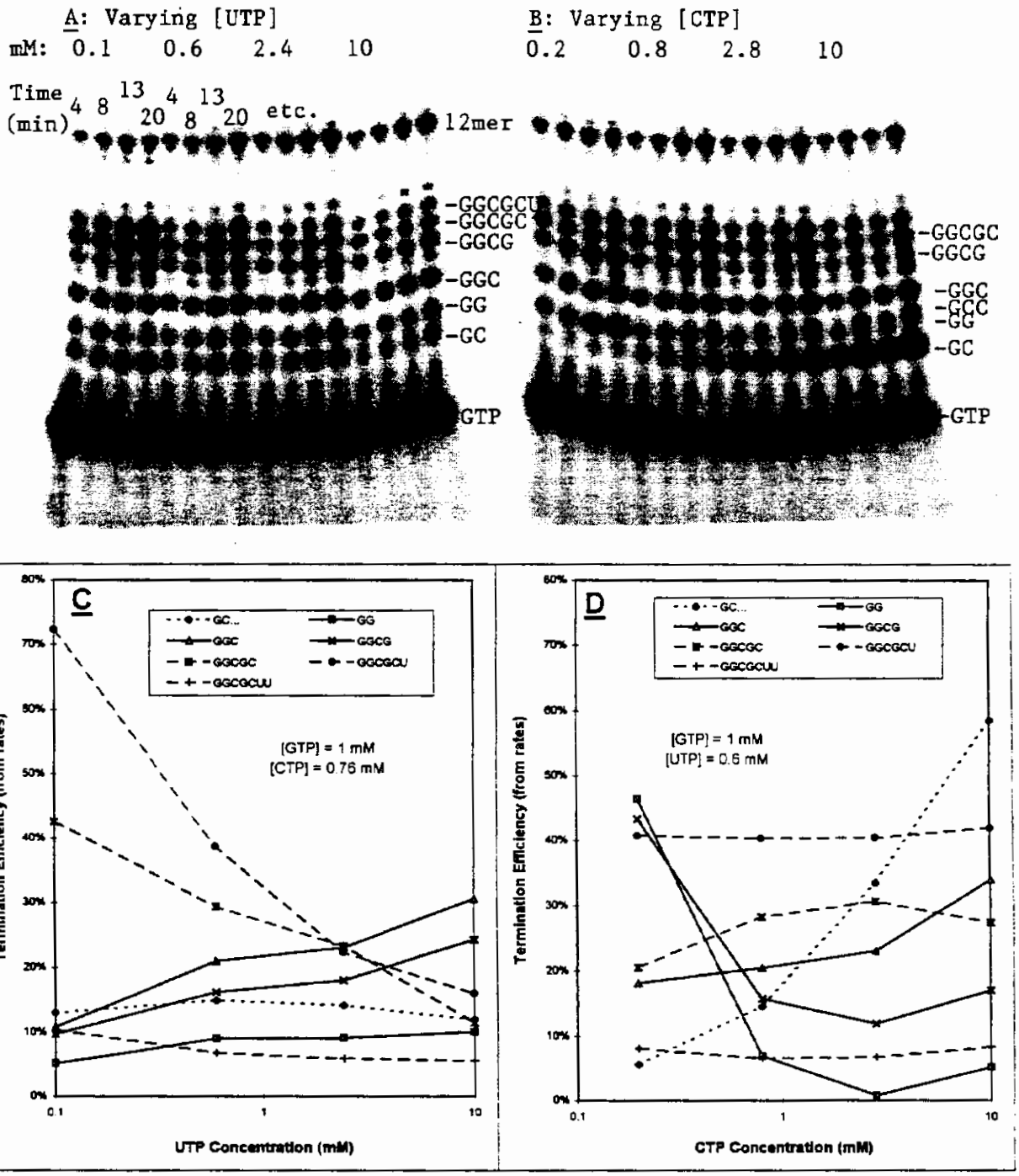

Figure 6: Effect of individual NTP concentrations on abortive transcription from the dodecamer DNA template. Transcription reactions were performed with 0.15 μM T7 RNA polymerase, 0.19 μM dodecamer DNA template, 30 mM $Mg(OAc)_2$, 1 mM GTP, and varying concentrations of CTP and UTP. (A) and (B): 20% acrylamide gels of reactions with varying UTP (A), and CTP (B). Estimated band identities are as indicated. (C) and (D): Termination efficiencies, defined as the percentage of transcripts at a given position which terminate rather than get elongated, as calculated based upon the initial rates of formation of the RNA transcript bands.

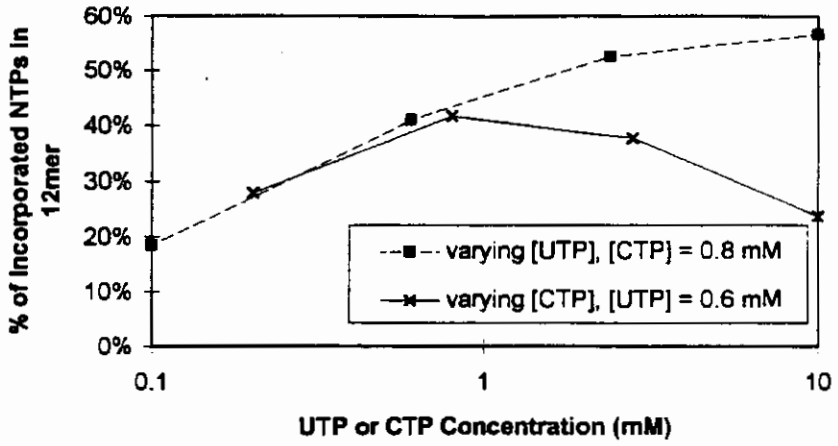

Figure 7: Total effect of UTP and CTP concentration on abortive transcription. For the reactions described in Figure 6, the percentage of incorporated NTPs which was incorporated into full-length product (rather than abortive transcripts) is plotted.

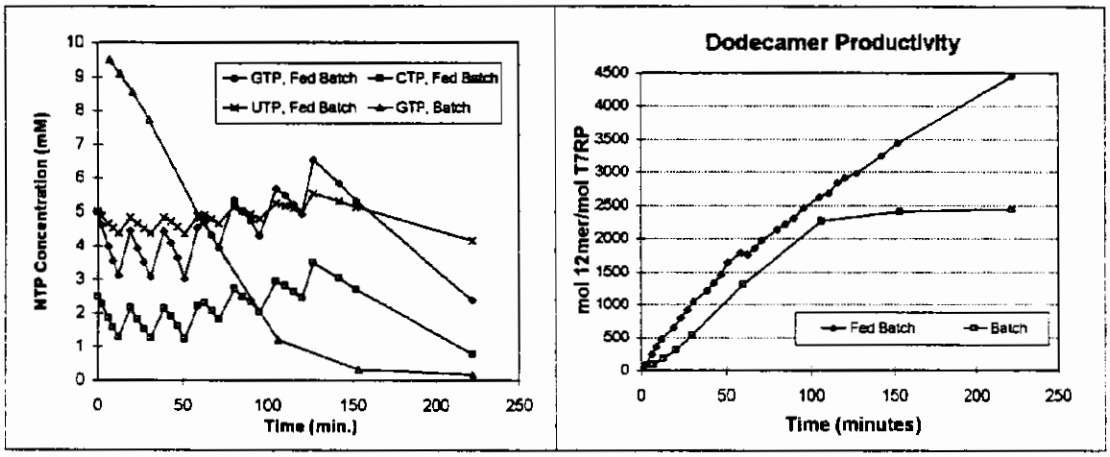

Figure 8: Fed-batch experiment. Additions of NTP and KOH feed solutions were made with the goal of maintaining the GTP concentration between 5 and 3 mM. Addition times were based upon reaction rates predicted from previous batch experiments. Samples were collected over the course of the reaction, electrophoresed on acrylamide gels, and analyzed by phosphorimaging. (A) NTP concentrations were maintained near optimum over the course of 6 additions; (B) comparison of dodecamer productivity for batch and fed-batch reactions.

length product, compared to about 40% when equimolar NTPs are used. The improvement is due primarily to the reduction of incorrectly initiated pppGpC... transcripts upon lowering of CTP concentration. These findings suggest that there could be benefit to using a fed-batch reactor, as this would allow the NTP concentrations to be maintained near their optimum for minimization of abortive transcription.

Fed-Batch Reaction Experiments

Since hydrogen ions are produced stoichiometrically in the reaction, the addition of NTPs and magnesium can be correlated to the addition of KOH necessary to maintain a constant pH. This hypothesis was tested for the production of the dodecamer by performing reactions in which two feed solutions, one of KOH, and the other a mixture of NTPs, magnesium, and transcription buffer, were added periodically to the reaction. As shown in Figure 8, these studies indicate that significant improvements in the yield of RNA produced per mole of polymerase or DNA may be possible with

a fed-batch system. The batch reaction which was performed for comparison was carried out at conditions determined to be optimal for maximal batch production of dodecamer RNA.

Proposed Fed-Batch Reactor System

An automated fed-batch reactor system, as depicted in Figure 9, is being assembled in our lab. Addition of KOH will be continually adjusted to maintain a constant pH, and the NTPs and $Mg(OAc)_2$ will be added at a fixed ratio to the KOH. The reactor will consist of a 10 mL Amicon stir-cell. The stir cell can be operated with as little as 1 mL of fluid. A solid-state microelectrode will be mounted to allow constant measurement of the pH of the reaction mixture. When the pH falls below a set value, a pH controller will send a signal to a relay which will activate a dual syringe pump. The syringe pump will be loaded with two syringes containing the feed solutions. Constant mixing of the stir cell will prevent localized high alkalinity upon addition of the KOH, thus preventing possible hydrolysis of the RNA. An additional signal from the pH controller will be output to a computer, so that the status of the syringe pump will be recorded during the course of a reaction. The recorded data will be used to calculate the total feed solution added to the reactor after any given amount of time, thus allowing detailed analysis of the fed-batch reaction.

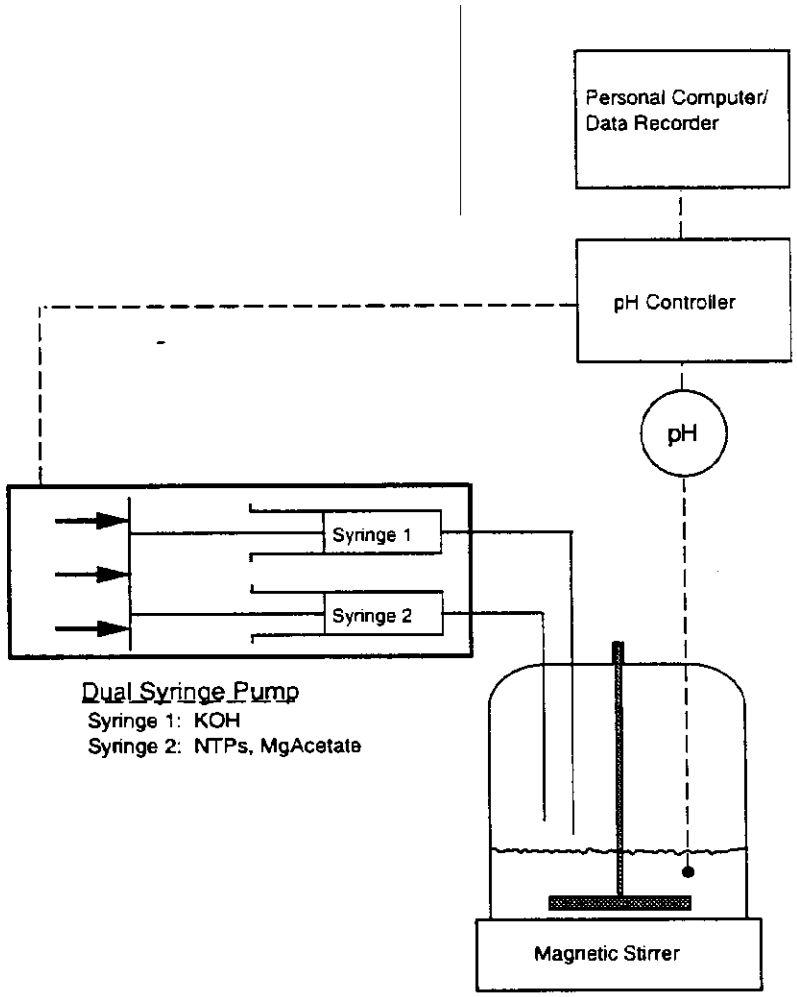

Figure 9: Proposed fed-batch reactor system. The pH, free magnesium concentration, and NTP concentrations will be maintained constant by the controlled addition of feed solutions of potassium hydroxide, and a mixture of NTPs and $Mg(OAc)_2$.

ACKNOWLEDGEMENTS

This work was supported by grants from the Colorado RNA Center and the Whitaker Foundation. Appreciation is expressed to Elizabeth White and Dina Svaldi for their assistance with the experiments.

REFERENCES

1. Cech, T. R. (1987) The chemistry of self-splicing RNA and RNA enzymes, *Science* **236**:1532-1539
2. Tuerk, C., and Gold, L. (1990) Systematic evolution of ligands by exponential enrichment: RNA ligands to bacteriophage T4 DNA polymerase, *Science* **249**:505-510
3. Jenison, R. D., Gill, S. C., Pardi, A., and Polisky, B. (1994) High-resolution molecular discrimination by RNA, *Science* **263**:1425-1429
4. Vinayak, R., Anderson, P., McCollum, C. and Hampel, A. (1990) Chemical synthesis of RNA using fast oligonucleotide deprotection chemistry, *Nucleic Acids Research* **20**:1265-1269.
5. Milligan, J. F., and Uhlenbeck, O. C. (1989) Synthesis of small RNAs using T7 RNA polymerase, *Methods in Enzymology* **180**:51-62
6. Milligan, J. F., Groebe, D. R., Witherell, G. W., and Uhlenbeck, O. C. (1987) Oligoribonucleotide synthesis using T7 RNA polymerase and synthetic DNA templates, *Nucleic Acids Res.* **15**:8783-8798
7. Davanloo, P., Rosenberg, A. H., Dunn, J. J., and Studier, F. W. (1984) Cloning and expression of the gene for bacteriophage T7 RNA polymerase, *Proc. Natl. Acad. Sci. USA* **81**:2035-2039
8. Carpousis, A. J. and Gralla, J. D. (1980) Cycling of ribonucleic acid polymerase to produce oligonucleotides during initiation in vitro at the *lac* UV5 promoter, *Biochemistry* **19**:3245-3253
9. Martin, C. T., Muller, D. K., and Coleman, J. E. (1988) Processivity in early stages of transcription by T7 RNA polymerase, *Biochemistry* **27**:3966-3974
10. Krieg, P. A. and Melton, D. A. (1987) In vitro RNA synthesis with SP6 RNA polymerase, *Meth. in Enzymol.* **155**:397-415
11. Marble, H. A. and Davis, R. H. (1995) RNA transcription from immobilized DNA templates, *Biotechnol. Prog.* **11**:393-396
12. Oakley, J. L., Strothkamp, R. E., Sarris, A. H., and Coleman, J. E. (1979) T7 RNA polymerase: promoter structure and polymerase binding, *Biochemistry* **18**:528-537
13. Nanninga, L. B. (1961) The association constant of the complexes of adenosine triphosphate with magnesium, calcium, strontium, and barium ions, *Biochim. Biophys. Acta* **54**:330-338
14. Volk, S. E., Baykov, A. A., Duzhenko, V. S., and Avaeva, S. M. (1982) Kinetic studies on the interactions of two forms of inorganic pyrophosphatase of heart mitochondria with physiological ligands, *Eur. J. Biochem.* **125**:215-220
15. Budavari, S. (1989) The Merck Index: An encyclopedia of chemicals, drugs, and biologicals, 11th ed., Merck: Rahway, New Jersey, U.S.A.

Bioprocessing of Sweet Sorghum with *in situ* Produced Enzymes

G. Szakacs, M. Pecs, Technical University Budapest, Hungary
J. Sipocz, I. Kaszas, Pannon Agrarian University, Hungary
S.R. Decker, J.C. Linden, R.P. Tengerdy, Colorado State University

Summary

The *in situ* enzymes from *Gliocadium* sp. TUB-F-498 were produced on the extracted sweet sorghum pulp by a six day solid substrate fermentation (SSF) with a yield of 4.5 IU/g DW cellulase, 400 IU/g DW xylanase and 0.5 IU/g DW acetyl xylan esterase (AXE). Applications of 2% of the fermented material to fresh sweet sorghum had cellulase and xylanase levels equivalent or superior to levels found in the commercial enzymes Celluclast and Viscozyme Novo® at the 0.025% application rate normally used in enzyme assisted ensiling (ENLAC). ENLAC using *in situ* produced enzymes preserved 80% of the sugar content of sweet sorghum and facilitated its extraction by counter-current diffusion.

The integrated bioprocessing scheme for production of ethanol from sweet sorghum is shown in Figure 1. The *in situ* production of enzymes on recyclable substrates may reduce bioprocessing costs significantly. In this ENLAC process, the cost of the *in situ* enzymes is estimated to be about $0.12/MT substrate, compared to $9.50/MT for the commercial enzymes, a cost reduction of near 80 fold.

Methods

Solid Substrate Fermentation (SSF)

The substrate for SSF was the sweet sorghum pulp resulting from the counter-current diffusion of ensiled sweet sorghum. The pulp was supplemented with basal salt solution (Mandels and Reese, 1966) to 30% DM content, sterilized, inoculated with TUB-F-498 or other fungi (10^6 spores/g DW substrate), and packed loosely into plastic cups (33g/100 mL). Air was supplied through perforations in the top and sides of the cup and incubated for six days at 30°C in a 99.9% relative humidity chamber. The contents of each cup was extracted with 50 fold excess of water containing 0.1% Tween-80 and enzyme activities in the filtrate were measured. Five fungal species were assayed for enzyme production by SSF. The results are shown in Table 1 and indicate that TUB-F-498, *Gliocladium* sp. was the best enzyme producer under the given conditions. Growth and enzyme production kinetics are given in Figure 2.

Enzyme Assisted Ensiling

Chopped sweet sorghum was mixed with supplements and packed into 200 mL Mason jars with tight-fitting lids. Samples were taken at 15 and 60 days and analyzed for dry matter and reducing sugar content. Reducing sugar concentration was determined by the DNSA method of Miller (1959). Supplements to ensiling included none (control), lactic acid bacteria (LAB), Viscozyme Novo® (0.075% v/w) + LAB, and *in situ* enzyme (*Gliocladium* TUB F-498, 2% w/w) + LAB. The LAB were added at 10^5 CFU/g sorghum. The initial sugar content of the chopped sweet sorghum was 364 g/kg DM at a DM content of 31.4% (w/w). The results presented in Table 2 indicate the applicability of *in situ* enzymes to ENLAC.

Table 1. Comparison of fungi for enzyme production in solid substrate fermentation.

Strain	DM %	Cellulase IU/g DM	Xylanase IU/g DM
Trichoderma reesei RUT C30	31.5	3.1	240.9
Trichoderma hamatum TUB F-105	30.4	2.7	217.0
Trichoderma sp. TUB F-482	30.9	3.4	142.3
Trichoderma sp. TUB F-486	31.0	2.9	141.1
Gliocladium sp. TUB F-498	29.7	4.6	400.0

Table 2. Conservation of sugar content in ENLAC.

Treatment	Reducing sugar g/kg DM		DM %
	15 days	60 days	
Untreated sweet sorghum	201.1	25.0	21.3
Control silage	235.9	47.5	25.3
Silage + LAB	232.2	106.7	26.6
Silage + Viscozyme +LAB	336.6	280.6	23.7
Silage + *in situ* enzyme + LAB	350.1	290.5	23.0

Native Acetylated Xylan Production

Native acetylated xylan from birchwood was used as the substrate for AXE. The standard alkaline extraction of hemicellulose from wood results in the cleavage of the acetyl esters from the hemicellulose. Chemically reacetylating the extracted xylan results in a different acetylation pattern of the xylan from the native wood tissue. To avoid this, holocellulose was prepared from birchwood and then extracted with DMSO to remove the hemicellulose fraction, which was termed native acetylated xylan.

Holocellulose was prepared from birchwood flour (40-60 mesh) by the acid chlorite method (Timmel, 1965), as modified by Herbert A. Schroeder (personal communication). Three hundred grams of flour was exhaustively extracted with ethanol:xylene (2:1) and then air dried. The wood was then suspended in 5 ℓ of water at 60-70°C. This mixture was acidified with 33 mL acetic acid, followed by the addition of 100 g of sodium chlorite. The acetic acid and sodium chlorite additions were repeated at 20, 60, 120 and 210 mins, for a total of five

additions. The material was then stirred at room temperature overnight, filtered, washed extensively with water and air dried, yielding holocellulose.

To improve hemicellulose recovery, the holocellulose was saturated in 5% ethanolic monoethanolamine, washed twice with 95% ethanol, twice with ether and then air-dried. Two liters of DMSO was added and the mixture was stirred overnight at room temperature and filtered. The DMSO extraction was repeated twice and the pooled extracts were added dropwise to four volumes of 95% ethanol containing 3% (v/v) acetic acid. The precipitate was removed by centrifugation and the resuspended in 95% ethanol 1% acetic acid. The centrifugation and resuspension was repeated using 95% ethanol, absolute ethanol (twice) and ether (twice). The recovered hemicellulose was then vacuum dried at room temperature and ground in a glass mortar and pestle (Bouveng and Lindberg, 1965, modified by Schroeder).

Enzyme Assay Procedures

Cellulase and xylanase activities were determined by the method of Ghose (Ghose, 1987). Acetyl xylan esterase activity was assayed on native acetylated xylan. Five milliliters of an acetyl xylan suspension (3.75 g/L in 20 mM phosphate buffer pH 6.5) was incubated with 1.0 mL of enzyme preparation in a shaking incubator at 37°C, 150 rpm. One milliliter of 1.8M NaOH was added to one vial and 1.0 mL of phosphate buffer was added to a second vial as positive and negative controls. Samples (0.5 mL) were taken at 0, 30, 60, and 120 min. The samples were filtered through a 0.45 μm Acrodisc, 13mm diameter membrane filter (Gelman). Acetic acid was determined on a Hewlett Packard 1084B HPLC using an HPX-87H organic acid column (BioRad) at 65°C with 0.008N H_2SO_4 as the mobile phase and a Waters R401 refractive index detector.

Enzyme Storage Stability

The enzyme preparations to be assayed were stored for one month under a variety of conditions and then extracted with 0.1% (v/v) Tween 80 in water at 37°C, 150 rpm for 60 min. The storage conditions were as follows: I) 4°C, II) -20°C, III) freeze dried, and IV) air dried. The results are shown in Table 3.

Table 3. Enzyme activity in stored *in situ* produced enzyme extracts.

Storage	mg/mL Protein	$\frac{\mu mol\ Acetate}{min \cdot mL}$	AXE IU/mg protein	FPA IU/mL	FPA IU/mg protein
Initial	ND	ND	ND	0.23	ND
4°C	0.528	0.0328	0.0621	0.18	0.34
-20°C	0.369	0.0368	0.0997	0.21	0.55
freeze dried	0.316	0.0340	0.1076	0.18	0.57
air dried	0.362	0.0322	0.0890	0.22	0.61

Discussion

Comparison of Commercial and *in situ* Enzyme Costs for Enzyme Assisted Ensiling.

NOVO Celluclast 1.5L, a commercial cellulase, has a cellulase activity of 80 IU/mL and a cost of \$12.00/ℓ. This results in a cost of \$1.5 x 10^{-4}/IU. Viscozyme 120L, a commercial pectinase and hemicellulase, has a cost of \$26.00/ℓ. At the recommended loading level of 0.025% (v/w) (Weinberg *et al* 1990), the enzymes costs for the Celluclast and Viscozyme are \$3.00/MT and \$6.50/MT biomass respectively.

Celluclast:
$$\frac{250\ mL}{MT} \times \frac{\$12.00}{1000\ mL} = \frac{\$3.00}{MT}$$

Viscozyme:
$$\frac{250\ mL}{MT} \times \frac{\$26.00}{1000\ mL} = \frac{\$6.50}{MT}$$

Total commercial enzyme cost: \$9.50/MT

A 2% addition of the *in situ* enzyme source to the substrate would provide 27,000 IU/MT cellulase and 900,000 IU/MT xylanase, more than the activity level of the 0.025% commercial enzyme addition. The cost of *in situ* enzyme production is approximately \$6.00/MT, based on commercial composting costs. This gives an enzyme cost for ENLAC of \$0.12/MT.

$$\frac{\$6.00}{MT} \times 0.02 = \frac{\$0.12}{MT}$$

Comparison of Commercial and *in situ* Enzyme Costs for Simultaneous Saccharification and Fermentation.

The recommended cellulase loading for simultaneous saccharification and fermentation is 7.0 IU/g cellulose. At \$1.5 x 10^{-4}/IU, this results in a cost of \$1050.00/MT cellulose for commercial enzyme (NOVO Celluclast 1.5L). The *in situ* produced enzyme had a maximum activity of 4.5 IU/g DM. At \$6.00/MT and 30% DM substrate, this results in a cost of \$31.11/MT cellulose.

Novo Celluclast 1.5L:
$$\frac{\$1.5 \times 10^{-4}}{IU} \times \frac{7\ IU}{g\ cellulose} \times \frac{10^6\ g\ cellulose}{MT cellulose} = \frac{\$1050.00}{MT cellulose}$$

in situ enzyme:
$$\frac{1.0\ g\ DM}{4.5\ IU\ cellulase} \times \frac{7.0\ IU\ cellulase}{1\ g\ cellulose} \times \frac{10^6\ g\ cellulose}{MT cellulose} \times \frac{1.0\ MT DM}{3 \times 10^5\ g\ DM} \times \frac{\$6.00}{MT biomass} = \frac{\$31.11}{MT cellulose}$$

For simultaneous saccharification and fermentation of a lignocellulosic substrate containing 30% (w/w) cellulose and 30% DM, the appropriate cellulase levels can be achieved by mixing *in situ* enzyme and substrate in a 1:2 ratio. This yields a mix of approximately 30% DM which can be further diluted with nutrient solution to reach the simultaneous saccharification and fermentation target of 10% solids.

$$\frac{10^6\ g\ substrate}{MT substrate} \times \frac{300000\ g\ DM}{10^6\ g\ substrate} \times \frac{0.3\ g\ cellulose}{1.0\ g\ DM}$$

$$\times \frac{7\ IU}{1.0\ g\ cellulose} \times \frac{1.0\ g\ in\ situ\ enzyme}{1.35\ IU} = \frac{466667\ g\ in\ situ\ enzyme}{MT substrate}$$

Storage study

The *in situ* enzyme fermentum was stored for one month under different conditions in order to determine the effects of storage on enzyme activity. Units of activity per milliliter remained fairly constant under the different storage conditions for both AXE and cellulase. However, increased protein content after storage at 4°C yielded a decreased specific activity for both enzymes. The protein levels in the frozen, air dried and freeze dried samples remained similar, as did the specific activities of these samples.

Conclusions

Cellulose is the most abundant renewable carbon source in the world, making up about 50% of all plant biomass. Because of it's intimate association with lignin and hemicelluloses such as xylan, it is relatively inaccessible to most organisms. Certain fungi have solved this problem through expression of complex and complimentary cellulase and xylanase enzyme systems. These enzymes work in synergy to breakdown lignocellulosic substrates and convert them to carbon and energy sources. The xylanase system of fungi is composed of multiple enzymes, including endoxylanases, β-xylosidase, various debranching enzymes (arabinofuranosidase, glucuronidase), and esterases (acetyl xylan-, coumaroyl- and feruloyl esterase). Because of the high degree of acetylation of some xylans, it is thought that AXE is one of the initial enzymes in the xylan degradation pathway. By removing some acetyl groups, other enzymes gain easier access to their respective substrate sites. Coumaroyl and feruloyl esterases detach xylan from the lignin matrix, loosening the cell wall structure and allowing access to cellulases and other xylanase enzymes.

Different plant materials contain different types and amounts of hemicelluloses. Different fungi have adapted themselves to grow on these different substrates. Use of different fungal strains and mixtures of fungal strains to produce *in situ* enzymes is a promising way of tailoring enzyme production to substrate composition at individual biomass processing facilities. In this mixed culturing, synergistic interactions may further enhance enzyme productivity.

We have shown that commercial enzymes are far more costly than *in situ* enzyme production. The estimate of enzyme cost for ENLAC was $9.50 per MT of biomass, compared to $0.12 per MT of biomass for *in situ* produced enzyme. For simultaneous saccharification and fermentation, the costs for commercial and *in situ* enzyme were $1050.00 and $31.11 per MT

cellulose, respectively. The methods used to generate these enzymes are simple, inexpensive and similar to techniques used for hundreds of years for industries such as composting and soy sauce production. Storage of the enzyme for at least 60 days is easily accomplished by simply air drying the fermentum. Low capital equipment investment and low-tech procedures make *in situ* enzyme production an attractive alternative to expensive commercial enzymes.

Literature Cited

- Bouveng, H.O. and Lindberg, B. 1965. In: "Methods in Carbohydrate Chemistry", R.L. Whistler, ed., Vol. V, pp. 147-149, Academic Press, N.Y.

- Ghose, T.K. 1987. Measurement of cellulase activities. Pure and Appl. Chem. 59:257-268.

- Mandels, M. and Reese, E.T. 1966. In: "Methods in Enzymology", E.F. Newfeld and V. Ginsburg, eds., Vol. VII, pp 607-615, Academic Press, N.Y.

- Miller, G.L. 1959. The use of dinitrosalicylic acid reagent for determination of reducing sugars. Anal. Chem. 31:426-428

- Timmel, T.E. 1965. In: "Methods in Carbohydrate Chemistry", R.L. Whistler, ed., Vol. V, p. 135, Academic Press, N.Y.

- Weinberg, Z.G., Linden, J.C. and Tengerdy, R.P. 1990. Recovery of protein and chlorophyll from alfalfa by simultaneous lactic acid fermentation and enzyme hydrolysis. Enzyme Microbiol. Technol. 12:921-925.

Figure 1. Integrated bioprocessing of sweet sorghum.

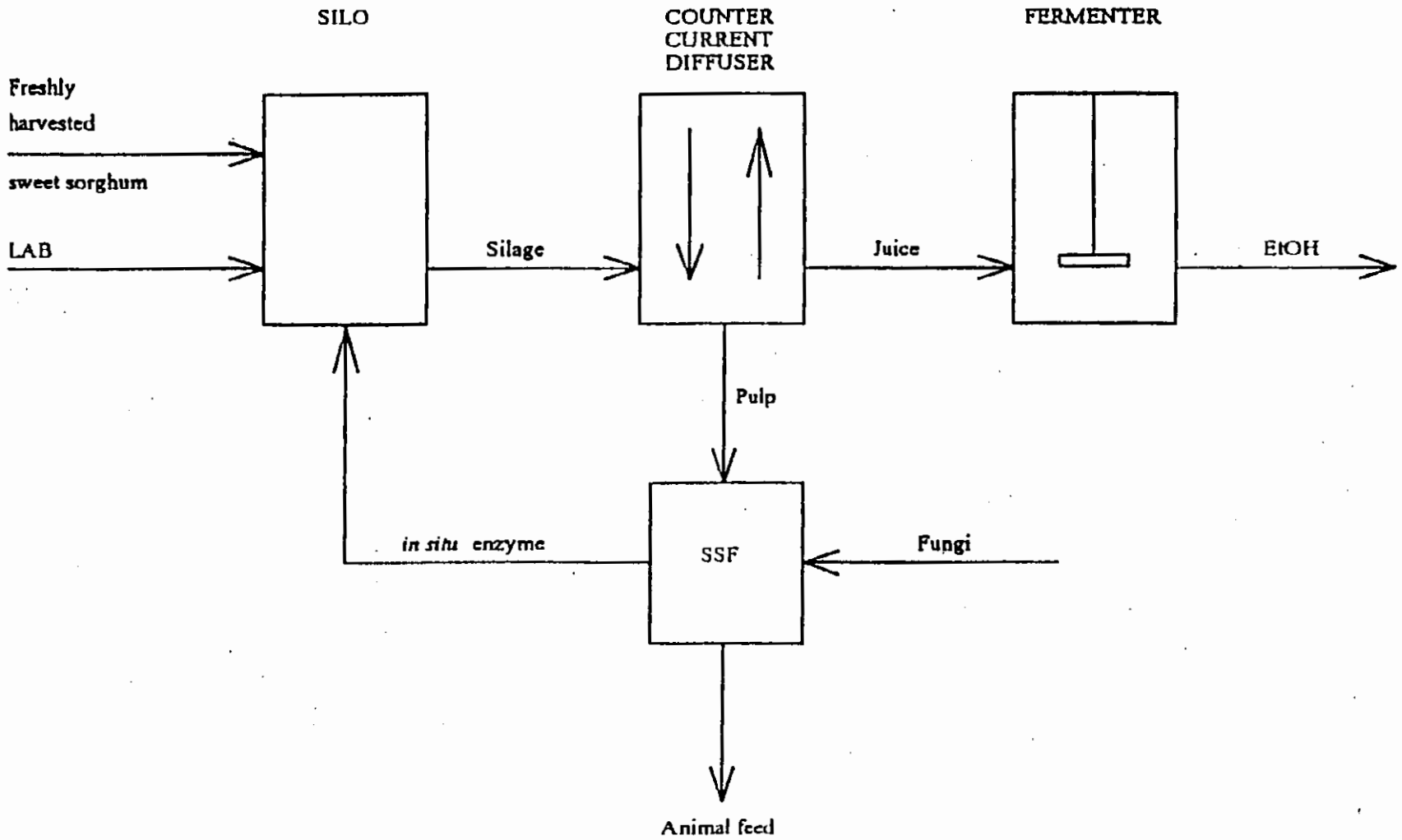

Figure 2. Kinetics of growth and enzyme production by *Gliocladium* sp. TUB F-498.

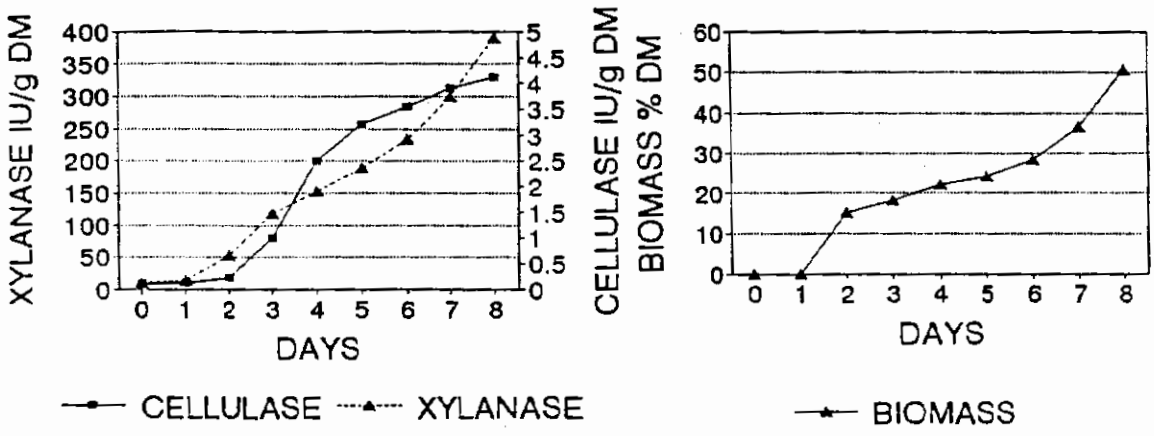

The Effect of Shear Stress and P-selectin Site Density on the Rolling Velocity of White Blood Cells

Brad Forlow and Matthias Nollert

Department of Chemical Engineering and Materials Science, The University of Oklahoma, Norman, OK

One of the most important functions of the immune response system is the recruitment of white blood cells to areas of infection or tissue damage. White blood cells first leave the central stream of flowing blood and roll along activated endothelial cells lining the blood vessel wall. Figure 1 shows the inflammatory response process. Once white blood cells roll on the endothelial cell surface, they adhere tightly, allowing them to emigrate between endothelial cells into the areas of infection or tissue damage. The rolling of white blood cells is a receptor-mediated process and occurs by receptor bonds forming at the leading edge of the cell and breaking at the trailing edge of the cell. The receptor molecules responsible for white blood cells coming out of circulation and rolling along endothelial cells are P-selectin, expressed on activated endothelial cells, and its high affinity ligand, P-selectin glycoprotein ligand-1 (PSGL-1), constitutively expressed on white blood cells. The process of white blood cell emigration is responsible for successful host response to infection or tissue injury. However, this process can be potentially harmful and contributes to various diseases and inflammatory disorders. Understanding the molecular basis of this mechanism by studying the biochemical and biophysical aspects of the process could lead to new therapeutic approaches for controlling the intensity and specificity of the immune response.

The biochemical and biophysical mechanisms involved in the rolling event due to P-selectin and PSGL-1 can be studied in vitro using simplified systems. The first simplified system that is being used is cells rolling over a planar lipid bilayer containing a receptor molecule. The cells used are HL-60 cells since they have monocyte-characteristics and express PSGL-1. They are bigger than white blood cells; however, they are very easy to grow in media which prevents having to draw blood for each experiment run. The planar lipid bilayers are composed of phosphatidylcholine with either a high concentration of P-selectin (approximately 150 sites/μm^2) or a low concentration (less than 25 sites/μm^2). Another simplified system that will be used is liposomes containing a receptor molecule rolling on a planar lipid bilayer containing the counter-receptor. Using a planar lipid bilayer containing the receptor molecule allows the interaction between P-selectin and PSGL-1 to be studied without cellular influences and other possible signaling events that could occur. Also, liposomes and lipid bilayers give a system in which the parameters that possibly affect the rolling mechanism can be controlled. The parameters that will be varied include wall shear stress, receptor site density (# molecules/area), receptor lengths, receptor flexibilities, and receptor lateral mobilities. The initial experiments studied the role P-selectin site density and shear stress increases had on the number of cells adhering to the surface and the rolling velocity of the cells that adhered to the surface.

The P-selectin/PSGL-1 interaction was studied using three indirect ways to measure the force of the bond: attachment assays, detachment assays, and rolling velocity experiments. For attachment assays, five or more sites were viewed on a bilayer and the number of cells adhering to the surface was counted. This was done for a high and a low P-selectin site density and three different shear stresses. Rolling velocities were calculated from the cells that adhered and rolled on the bilayer surface at the varying shear stresses. Detachment assays were used as an indirect measure of the force required to remove a cell once attached. Cells initially attach at a low flow rate. They were then subjected to increases in shear stress every 30 seconds. The number of cells remaining at the end of the 30 seconds were counted.

The attachment assays, rolling velocity experiments, and the detachment assays are all done under flow using a flow chamber that mimics the flow of blood through the body. The type of flow chamber used is shown in Figure 2. The lipid bilayer is formed on a supercleaned glass slide and attached to the chamber by an applied vacuum. The HL-60 cells enter the chamber at a controlled flow rate from a syringe pump. The height of the flow channel is created by the gasket material sealed between the chamber and glass slide. The flow experiments are viewed using phase contrast microscopy. An inverted phase contrast microscope is used with a video camera to record the experiments. The video images can be sent to a computer and analyzed using a commercial software program.

Results

Attachment Assays. Attachment assays were run at shear stresses of 1.0, 3.0, and 5.0 dynes/cm^2 on a bilayer containing P-selectin at approximately 150 sites/μm^2 to determine if the force would affect the number of cells adhering to the bilayer surface. Figure 3 shows the results of the attachment assays. The number of cells adhering to the surface were counted at various sites from independent experiments. The number of adherent cells were totaled and divided by the number of fields of view that were analyzed to give and average number of cells adhering per field of view. At 1.0 dynes/cm^2, an average of 16.6 (+/-10) cells adhered per field of view. However, when the shear was increased to 3.0 dynes/cm^2 only 4.9 (+/-5) cells per field of view attached. At 5.0 dynes/cm^2 the number of cells adhering was 5.2 (+/-3) cells per field of view.

Rolling Velocity Data. Rolling velocities were calculated for numerous cells at the varying shear stresses. The calculated rolling velocities for the cells at shear stresses of 1.0, 3.0, and 5 dynes/cm^2 on a bilayer containing approximately 150 sites/μm^2 are shown in Figure 4. The data shows that the cells rolled with a wide range of velocities. However, the average rolling velocity at the different shear stresses varied little (see Figure 5).. At 1.0 dynes/cm^2 the average rolling velocity was 15.0 μm/s and the average rolling velocities at 3.0 dynes/cm^2 and 5.0 dynes/cm^2 were 18.4 μm/s and 16.2 μm/s, respectively.

Detachment Assays. Detachment assays were done to give an indirect measurement of the amount of force required to remove the cells once attached. Figure 6 shows the

detachment assay data which only represents two independent experiments, but shows the expected trend. Cells attach at flow rate of 0.1 dyne/cm^2 and are counted to give an initial number attached. They are then subjected to an increase in shear every 30 seconds. The number of cells remaining at the end of the 30 second interval are counted.

Attachment Assays and Rolling Experiments at Low P-selectin Site Density. Attachment assays and rolling velocity experiments were also attempted at varying shear stresses on a bilayer containing P-selectin at a site density of less then 25 sites/μm^2. However, at this site density of P-selectin a different type of attachment was observed. Instead of rolling, transient attachment was seen up to approximately 1.0 dynes/cm^2. Transient attachment is defined as a cell attaching (sticking) to the surface then releasing at the hydrodynamic velocity without moving (rolling) while on the bilayer surface.

Discussion

Attachment assays run at varying shear stresses on a bilayer containing P-selectin at approximately 150 sites/μm^2 indicate the force (shear stress) is a parameter that affects cell adherence. As the force was increased a noticeable decrease occurred in the number of cells that attached to the bilayer. Rolling velocities were calculated for the same cells at the varying shear stresses. The average velocities that were calculated at shear stresses of 1.0, 3.0, and 5.0 dynes/cm^2 indicate that the increasing force does not greatly affect how fast the cells roll on the bilayer surface. This indicates the rolling velocity is instead controlled by the on-off rates of the receptor bonds. These flow experiments indicate we are capable of reproducing the rolling event in a simplified in vitro system. Attachment assays, detachment assays, and rolling velocity data are useful to obtain information on the P-selectin/PSGL-1 interaction under flow conditions. Using simplified systems to study P-selectin and PSGL-1 receptor interactions should help determine the mechanism and parameters which control the rolling of white blood cells on the endothelial surface.

Acknowledgments. I would like to thank Dr. Rodger McEver, Dr. Kevin Moore, Dr. Kamala Patel, and Cindy Carter of the Cardiovascular Biology Research Program at the Oklahoma Medical Research Foundation in Oklahoma City. Thank you providing the HL-60 cells and P-selectin and for your technical assistance in experimental procedures used in this project.

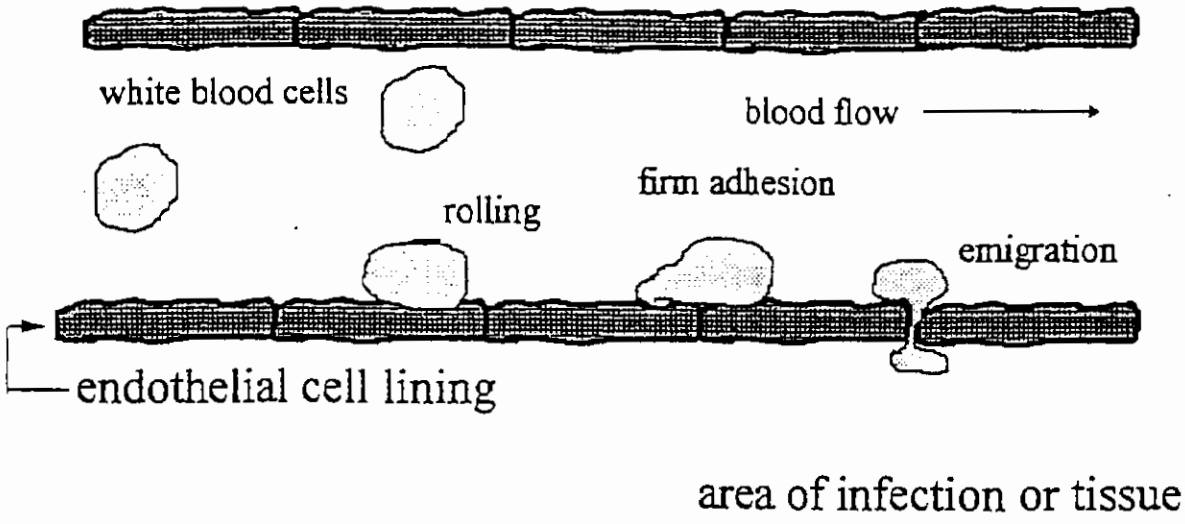

Figure 1: Inflammatory Response Process. White blood cells come out of circulating blood by receptor molecule interactions allowing them to roll on the endothelial cell surface. After white blood cells roll, they become firmly attached to the blood vessel wall. This allows them to then emigrate into the area of infection or injury.

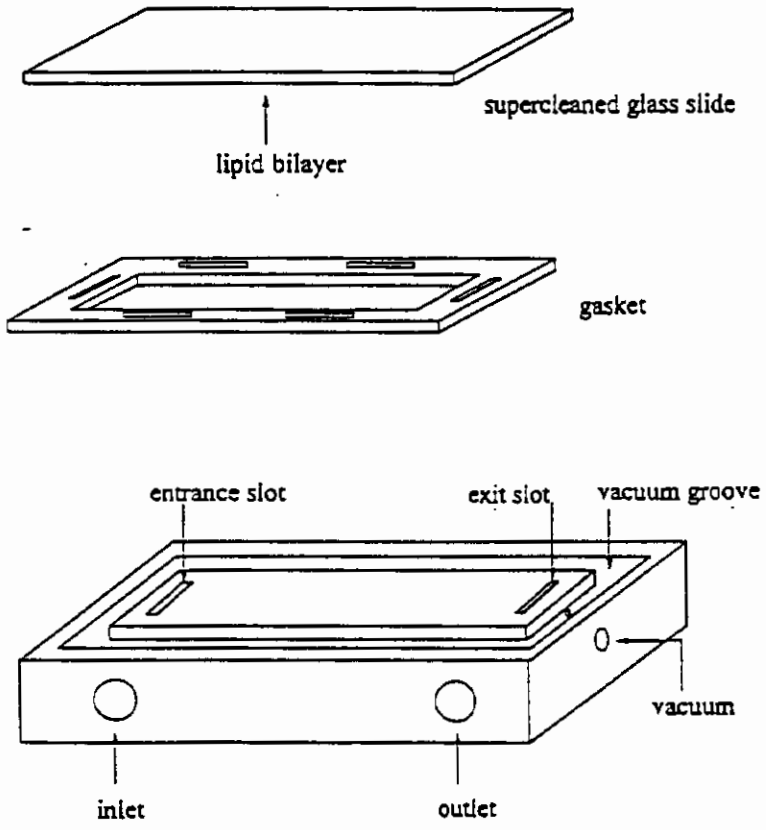

Figure 2: Flow Chamber. A lipid bilayer is placed on a glass slide and attached to the flow chamber by an applied vacuum. The height of the flow channel is provided by a gasket material. The cells enter the flow chamber at a controlled rate using a syringe pump. The experiments done with the flow chamber are viewed by phase contrast microscopy with a video camera allowing the experiments to be taped and analyzed at a later time.

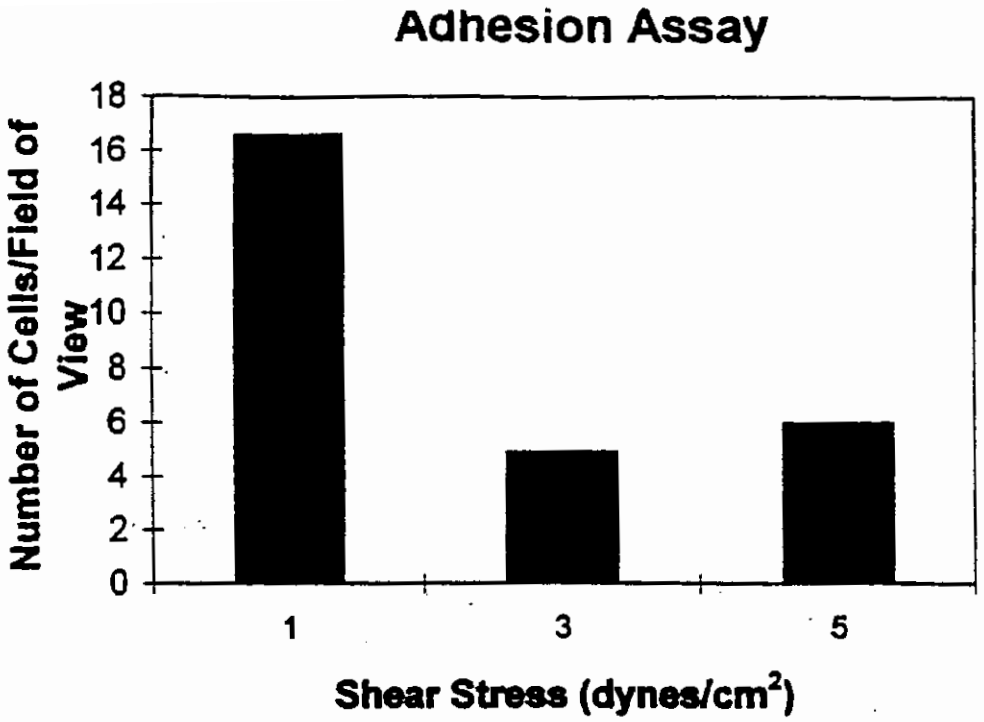

Figure 3: Attachment Assay. The number of cells adhering to the surface were counted at various sites from independent experiments. The number of adherent cells were totaled and divided by the number of fields of view that were analyzed to give an average number of cells adhering per field of view. The attachment assays were run at shear stresses of 1.0, 3.0 and 5.0 dynes/cm^2. As the shear increased the number of cells adhering per field of view decreased from 16.6 at 1.0 dynes/cm^2 to 4.9 and 5.0 at 3.0 dynes/cm^2 and 5.0 dynes/cm^2, respectively.

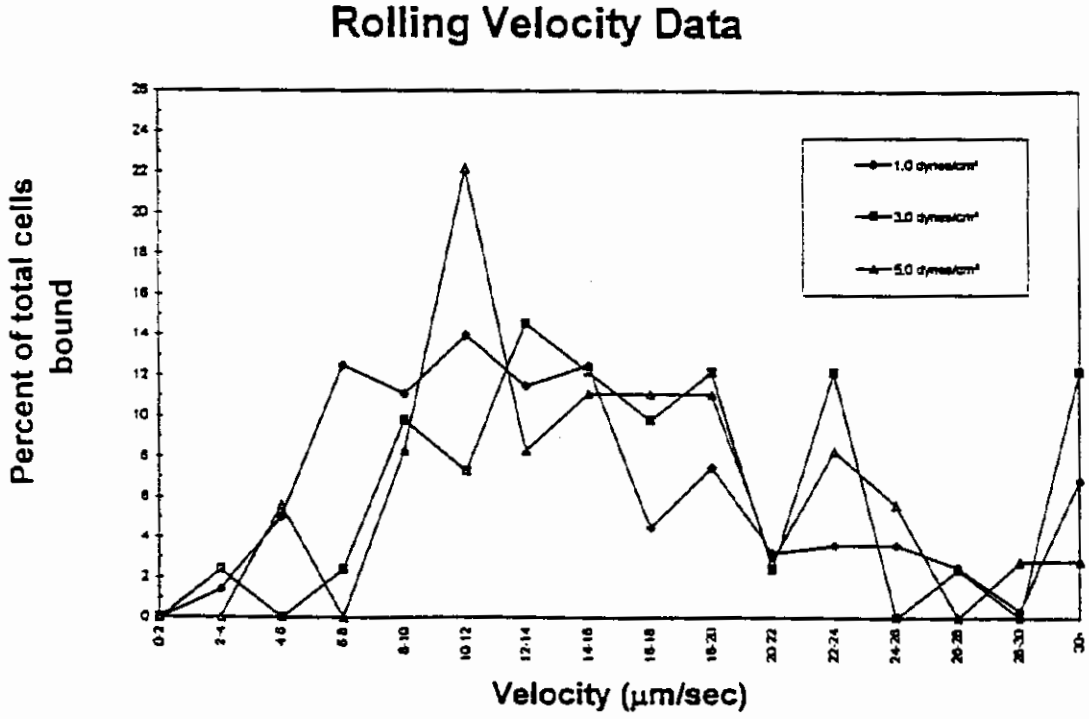

Figure 4: Rolling Velocity Data. The rolling velocity of adhering cells was calculated for numerous cells at the varying shear stresses. For 1.0 dynes/cm^2 the data represents velocities of 279 cells from 6 experiments (17 sites, 40 fields of view). For 3.0 dynes/cm^2 the data represents 41 cells from 4 different experiments (8 sites, 10 fields of view). For 5.0 dynes/cm^2 the data represents 36 cells from 2 different experiments (4 sites, 7 fields of view). For each shear stress, the cells roll with a wide range of velocities.

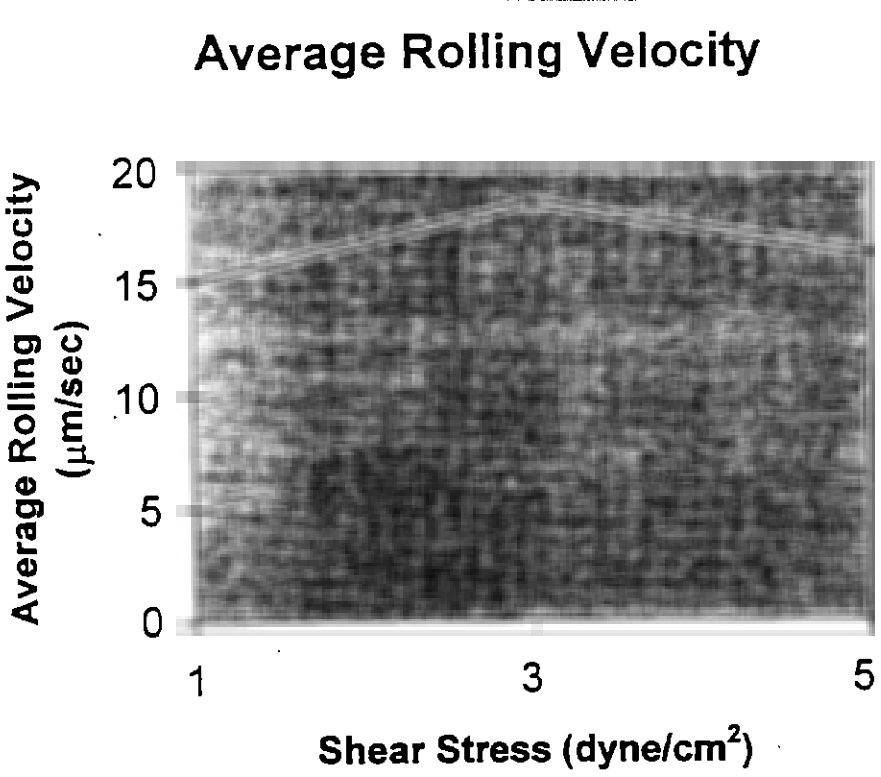

Figure 5: Average Rolling Velocity. The average rolling velocity was calculated for the data shown in Figure 4. At 1.0 dynes/cm^2 the average rolling velocity was 15.0 μm/s. For 3.0 and 5.0 dynes/cm^2, the average rolling velocities were 18.4 μm/s and 16.2 μm/s, respectively. Figure 4 shows cells rolling at a wide range of velocities; however, the average rolling velocity of the cells at the different shear stresses vary little.

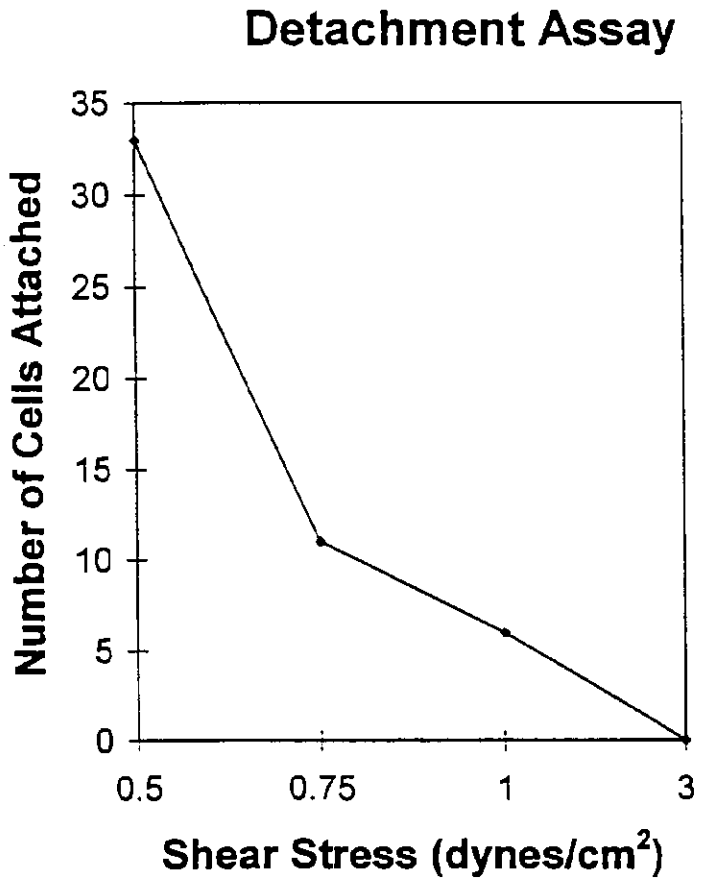

Figure 6: Detachment Assay. Cells were initially allowed to adhere to the surface at 0.1 dynes/cm^2. The shear was then increased in stage increments every 30 seconds. After the 30 second time interval, the number of cells remaining adhered were counted. The data presented represents 2 independent experiments.

The Effects of Polyethylene Glycol and Dextran on the Lyophilization of Human Hemoglobin

Martin C. Heller and Theodore W. Randolph
Department of Chemical Engineering, University of Colorado, Boulder, CO 80309

Abstract

Recombinant human hemoglobin was lyophilized in the presence of varying concentrations of polyethylene glycol (PEG) and dextran. The dried samples were characterized using Fourier-transform infrared (FTIR) spectroscopy, differential scanning calorimetry and reconstituted met-hemoglobin content. Lyophilization in the absence of excipients induces significant changes in the amide I region of the FTIR spectra. The addition of PEG or dextran causes an observable mitigation in the conformational change, although all samples experienced high levels of met-hemoglobin formation. Calorimetry of freeze-dried samples suggest two different crystalline PEG populations, a possible consequence of liquid-liquid phase separation. Phase separation may also explain observable differences in physical appearance of the cake structure.

Introduction

Lyophilization, or freeze-drying, is often a desired processing step for protein products that are not sufficiently stable in liquid formulations. Properly freeze-dried proteins are generally less susceptible to shipping and handling stresses and have improved shelf-lives. Most proteins, however, are acutely sensitive to lyophilization, and the inherent stresses of freezing and drying can cause irreversible damage to a protein, manifested as structural denaturation and aggregation upon rehydration. Thus, efforts must be made to preserve a protein's biological activity upon reconstitution by mitigating the stresses of freeze drying in order to gain the benefits of a freeze dried product. A wide variety of solutes, including sugars, polyols, amino acids, and other polymers, offer thermodynamic stabilization to proteins in liquid, aqueous solutions through the preferential exclusion mechanism of Timmasheff and co-workers.[1] Protection of proteins during freezing by such additives has also been explained by this universal thermodynamic mechanism.[2] In short, stabilizing solutes are preferentially excluded from the surface of a protein (zone of exclusion), raising the chemical potential of the protein. This zone of exclusion is larger, however, for denatured, unfolded protein, resulting in a larger transfer free energy for the denatured state, thus favoring the native, compact protein (see figure 1).

It stands to reason that the preferential exclusion mechanism is no longer directly applicable during drying because the requisite thermodynamic arguments rely strongly on the presence of the protein's hydration shell. A number of co-solutes (e.g., polyethylene glycol) which demonstrate high effectiveness as cryoprotectants are not necessarily effective as stabilizers during drying.[3] There is, however, an accumulation of additives, many of them carbohydrates, that have been empirically identified to protect labile proteins

during lyophilization. Despite many suggestions, the exact mechanism of protection during drying is unclear. Some researchers[4,5] contend that proteins are mechanically immobilized in the glassy solid matrix of the dried state, thus preventing protein unfolding by restricting translational and relaxation processes. Others[6,3] suggest that stabilizing additives (such as trehalose) act as "water substitutes" in the dried state by hydrogen bonding to the dried protein. These authors attribute the ineffectiveness of solutes such as polyethylene glycol to their tendency to crystallize during lyophilization, rendering them unavailable to hydrogen bond with dried protein.

The study presented here represents preliminary results of an inquiry into the mechanism of protein stabilization by co-solutes during freezing and drying. In particular, we are interested in the potential for long-chain sugars and polymers to cause liquid-liquid phase separation during the lyophilization process, adding yet another complication to the behavior of freeze dried proteins. Consider a typical lyophilization cycle, depicted in figure 2a. The sample is cooled until pure ice crystals begin to form, this point being determined by the colligative properties of the solution. Further freezing of ice causes an increase in concentration of the components in the non-ice phase (salts, protein, co-solutes). Such "freeze concentration" continues until the glass transition temperature is reached, at which point the remaining liquid vitrifies. Drying commences by pulling a strong vacuum and subliming away the bulk of the water. Now reconsider the freeze concentrating portion of this scenario with the ternary phase diagram of figure 3 in mind. The possibility exists that as water is removed from the non-ice phase and the remaining solutes concentrate, a liquid-liquid coexistence curve is encountered. The likelihood of phase separation increases when large supraideal solutes (polymers, polysaccharides) are added to the protein solution as stabilizers. Now there are essentially two systems to consider, with significantly different solute concentrations (figure 2b). Further, depending on the nature of the system, protein can partition into either phase, possibly away from the intended stabilizer, or become kinetically locked in an thermodynamically unfavorable phase. An additional complication arises in designing a lyophilization cycle; cycles are typically designed around calorimetric information which is an average of the entire system. If the system in question is in actuality composed of two phases, these phases can have different local glass transitions, potentially leading to a portion of the sample experiencing a melt during lyophilization.

The current study considers the effects of polyethylene glycol and dextran, two well known biological polymers, on the lyophilization of a recombinant human hemoglobin, with the potential for phase separation in mind.

Materials and Methods

Materials: Recombinant hemoglobin (rHb)[7] was obtained from Somatogen, Inc., Boulder , CO. in a 5mM phosphate buffer, pH 7.4, 150mM sodium chloride. Polyethylene glycol (PEG) with an average molecular weight of 3350 was obtained from Sigma and used as received. Dextran T500 (average molecular weight, 500,000) was obtained from Pharmacia Biotech as a highly pure powder, free of heavy metal contaminations, and used as received. Stock solutions of PEG and dextran were made at a concentration of 20%w/w in 5mM potassium phosphate, 150mM sodium chloride, pH 7.4. Solutions used for study were made from these stock solutions and hemoglobin solution at a concentration of 50mg/ml. Samples for lyophilization were prepared with a final hemoglobin concentration of 25mg/ml, and buffer concentrations were maintained at 5mM phosphate, 150mM sodium chloride.

Lyophilization. Samples of approximately 1mL were lyophilized in 3mL serum vials using a FTS Systems microprocessor controlled tray dryer. The following conservative freeze drying cycle was used: freezing with shelf temperature set at -50°C for 120 minutes; primary drying with shelf temperature at -20°C and vacuum set at 60mT for 1000 minutes; secondary drying steps to 0°C, 60mT for 120 minutes, 10°C, 60mT for 120 minutes, and 25°C, 60mT for 120 minutes.

Thermocouples placed in representative samples in each lyophilization run demonstrated that samples typically experienced around ten degrees of supercooling before freezing and cooling to shelf temperature. Evaporative cooling during primary drying drove the sample temperatures below -30°C.

Fourier Transform Infrared spectroscopy (FTIR). Infrared spectroscopy was used to assess the secondary structure of hemoglobin prior to lyophilization, in the dried state, and upon rehydration. Each type of secondary structure (α-helix, β-sheet, turn, unordered structure) in principle gives rise to a different C=O stretching frequency within the amide I band ($1700cm^{-1}$-$1600cm^{-1}$), rendering this region useful for studies of secondary structural composition and conformational change in proteins. Liquid samples with protein concentrations of 25 mg/ml were placed in IR cells with CaF_2 windows and 6-μm mylar spacers. The same cell was used to collect corresponding spectra of buffer blanks containing analogous components minus protein. Digital subtraction of the buffer spectrum was performed following the criteria of Dong *et al.*[8] Reconstituted freeze-dried samples were brought back to original concentration by the addition of deionized water and spectra were obtained in the manner described above.

Spectroscopy of the lyophilized samples was performed by pressing KBr pellets of 1-5mg of lyophilized protein mixture and about 200mg KBr. Pellets were placed immediately in the IR sample chamber in a magnetic sample holder.

All infrared spectra were collected using a Nicolet 800SX FTIR system equipped with a Globar source and a DTGS detector. 256 double sided interferograms collected with a Happ-Genzel apodization function and a resolution of $4cm^{-1}$ were co-added to give the final spectrum. Buffer and water vapor components were subtracted using the Nicolet software. Second derivative analysis[9] was used as a band-narrowing technique to discern the overlapping components of the amide I band. A seven-point smoothing was used to remove possible white noise, and a baseline correction was performed over the amide I region. Spectra were then normalized by their total area between $1700cm^{-1}$ and $1600cm^{-1}$ to allow direct comparison.

Differential Scanning Calorimetry (DSC) Calorimetry was used to consider the degree of PEG crystallinity found in lyophilized protein samples. All DSC thermograms were generated using a Perkin-Elmer DSC7, ramping from 20°C to 200°C at 5°C/minute. The presented thermograms are normalized by the suspected amount of PEG within the sample using a dry-weight percentage based on concentrations before drying.

Met-Hemoglobin assay. The heme iron of hemoglobin can undergo oxidation from the Fe^{2+} to the Fe^{3+} form, rendering hemoglobin as incapable of reversibly binding oxygen. The oxidized form of hemoglobin is known as met-hemoglobin. Met-hemoglobin levels were determined spectroscopically by the method of Tomita.

Results and Discussion

The effects of PEG on the conformational stability of hemoglobin in the dried state are given in Figure 4. Native hemoglobin's secondary structure is known to be primarily α-helix (87% by x-ray crystallography[10]), which is reflected in the second derivative IR spectra as a dominant sharp peak at $1656cm^{-1}$. The addition of PEG to liquid samples caused virtually no change in the IR spectra, and thus only a single liquid control is included in the figure. The dry-state spectrum of hemoglobin freeze-dried in buffer salts alone is significantly altered relative to the aqueous spectrum. The dominant α-helix peak area has shifted to wavenumbers indicative of intramolecular β-sheet (1689 and $1638cm^{-1}$), turn structures ($1677\ cm^{-1}$) and perhaps intermolecular β-sheet (1615 and $1627cm^{-1}$). The addition of 5%w/w PEG3350 to the protein solution provides a noticeable mitigation of the structural alterations caused by freeze drying, while 10%

PEG3350 shows an disproportionate additional increase in "native-like" structure. That is, the stabilizing effect of PEG3350 appears to be nonlinear with the polymer concentration. Also included in Figure 3 is a representative spectra of a re-hydrated sample. Again, all rehydrated samples were virtually identical, regardless of the polymer concentration. This indicates that hemoglobin, while showing conformational changes in the dry-state, refolds to a native structure upon rehydration.

Spectra of hemoglobin lyophilized in the presence of dextran500 are presented in figure 5. Analysis follows closely with that for PEG. IR spectra of liquid samples showed no conformational change with the addition of dextran. Dry-state spectra of samples lyophilized in the presence of dextran show a small, monatonic increase in "native-like" structure. All rehydrated samples showed virtually the same full return to native structure.

Met-hemoglobin levels of all reconstituted samples were greater than 75% compared to an average of 10% prior to lyophilization. There was no apparent trend with polymer concentration. The high met-hemoglobin levels indicate a loss in biological function. This may be attributed to the conformational change detected in the dry state; a primary function of the globin is to protect the chemically instable heme from autooxidizing.

The DSC thermograms presented in figure 6 focus on the distinct melting endotherm present in dried samples containing PEG. It should be noted that experimental samples that did not contain PEG demonstrated no calorimetric features in this temperature region. Included for comparison is a reference crystalline sample of PEG (taken directly from the bottle). While the freeze-dried experimental samples showed a peak corresponding to this reference crystalline melt, there is also the appearance of broader, lower temperature peak. This can be interpreted as a second population of crystalline PEG, different in calorimetric behavior from the reference sample. The second population may arise from interaction of the PEG with the protein or buffer salts, or it may be indicative of a phase separation occurring. It is interesting to note that there were visual differences in the cake structure of the samples lyophilized with PEG, the differences in the 5% PEG sample being the most prominent (photographs presented in the poster were not reproducible for this report). The cake structure of the sample containing 5%PEG was more granular in texture with large voids and a significantly darker color than both the sample without PEG and that containing 10%PEG. While the 10% PEG sample was also granular, it did not have the obvious voids in the cake structure that were present on the intermediate PEG concentration. This apparent extremity in physical appearance seems to correlate with the fraction of crystalline PEG in the lower temperature peak.

The results presented in this report show a clear effect of polyethylene glycol and dextran on the structure of lyophilized hemoglobin. Further, they emphasize the importance of analyzing the structural state of a protein in the dried solid. Solutions of PEG and phosphate undergo known liquid-liquid phase separation at appropriate concentrations. There is suggestion in the calorimetric studies of PEG containing freeze-dried samples that freeze concentration during the lyophilization cycle is causing such a phase separation to occur. This is also supported by the physical appearance of the cake itself. Clearly, the behavior of multi-component protein solutions during freeze drying involves a complex and delicate balance of thermodynamics and kinetics. The present

study has fostered further investigation into the behavior protein freeze-dried in phase separating systems.

References

[1]S.N Timmasheff, "Stability of Protein Pharmaceuticals," Part B, ed. by T. J. Ahern, M. C. Manning, Plenum Press, New York, 1992, pp.265-285.

[2]Carpenter, J.F., and J.H. Crowe, (1988), *Cryobiology*, **25**, 244.

[3] Carpenter, J.F., Prestrelski, S.J., and Arakawa, T., (1993) *Archives of Biochemistry and Biophysics*, **303** (2), 456-464.

[4] Franks, F., Hatley, R.H.M., and Mathias, S.F (1991) *BioPharm* **4**(9), 38-42.

[5] Levine, H., and Slade, L. (1992) *BioPharm* **5**(4), 36-40.

[6] Carpenter, J.F., and Crowe, J.H., (1989) *Biochemistry* **28**, 3916-3922.

[7] Looker, D. *et al.*, (1992) *Nature*, **356**, 258-260.

[8]Dong, A., and Caughey, W.S., (1994), *Methods in Enzymology*, **232**, 139-175.

[9] Dong, A., Prestrelski, S.J., Allison, S.D., and Carpenter, J.F., (1995) *J. of Pharm. Sciences*, **84** (4), 415-424.

[10] Levitt, M., and Greer, J. (1977) *J. Mol Biol.*, **114**, 181-239.

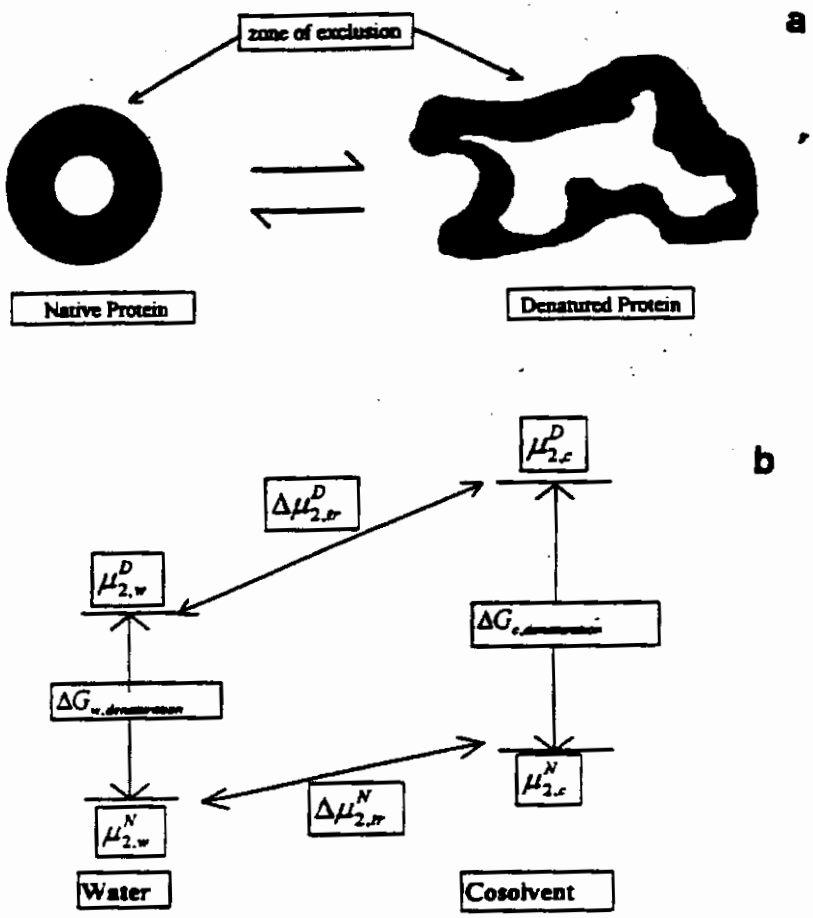

Figure 1: Schematic of the underlying principles of preferential exclusion. a) The unfolded, denatured state of a protein requires a much larger zone of exclusion than does the compact native structure. b) For the case of a protein stabilizer, the addition of a cosolvent (polymer) actually has a slight destabilizing effect on the protein (positive transfer free energies). This is larger for the denatured protein however (due to the zone of exclusion effect shown in a), with the net result being a relative stability effected on the native state relative to the denatured state ($\Delta G_{c,\ denaturation} > \Delta G_{w,\ denaturation}$)

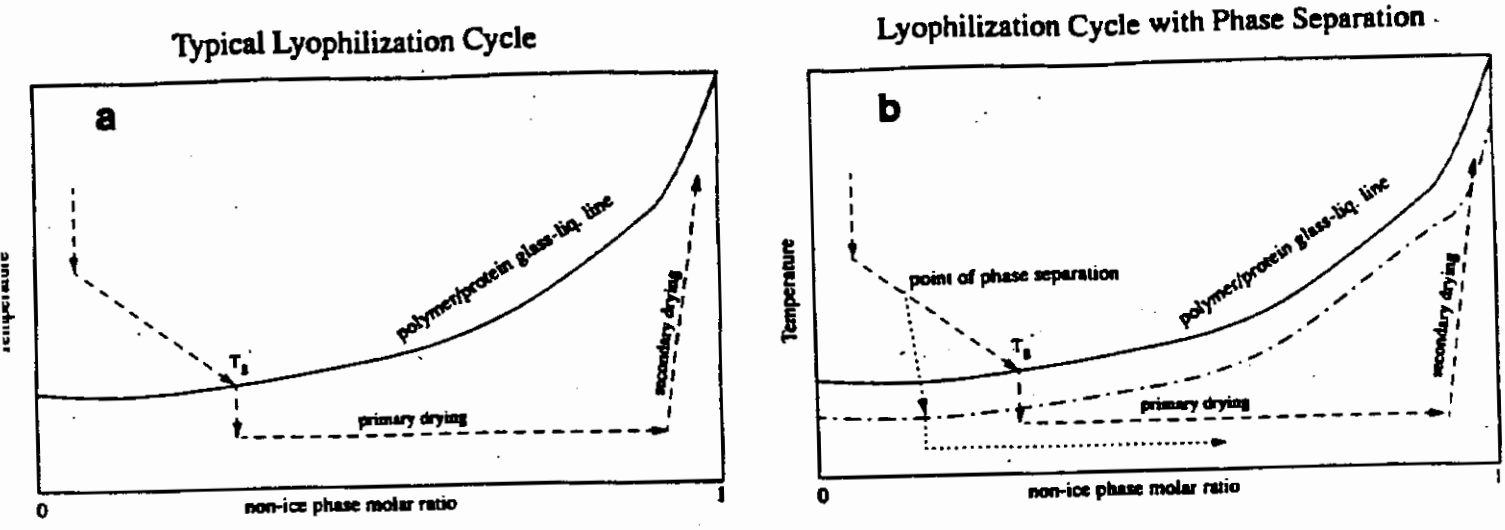

Figure 2: Schematic of a typical lyophilization cycle on a temperature-composition diagram (note that the concentration considered is that in the non-ice phase, i.e., salts, protein, polymer.) a) Cycle without a liquid-liquid phase separation. b) Phase separation has occurred as the system is freeze concentrated. Now there are two operating systems, with different T_g' s (glass transitions).

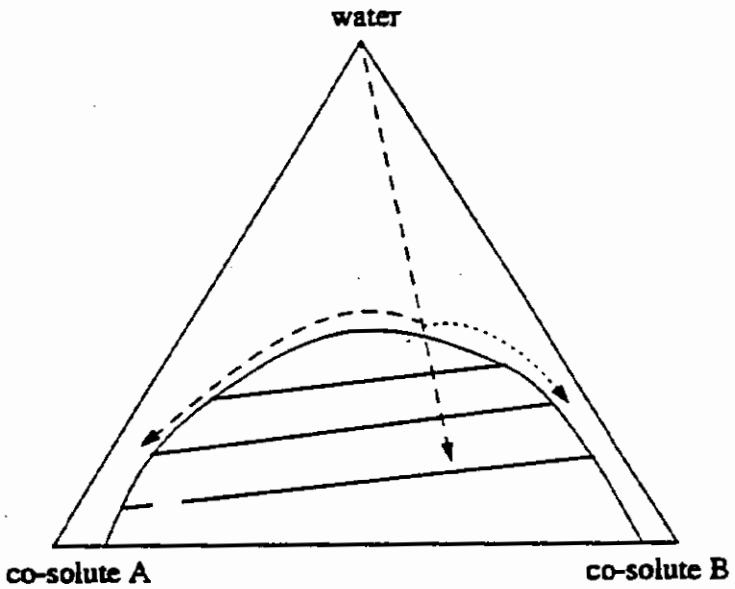

Figure 3: Ternary diagram demonstrating phase separation during freeze-concentration. A typical protein solution has been simplified by only considering 3 components. Solutions begin as primarily water (solute components are typically dilute). As ice forms a solid phase, solutes concentrate in the non-ice phase. A two-phase region is reached (likely when one or more of the components are strongly dissimilar) and the system separates into a phase rich in co-solute A and another rich in co-solute B.

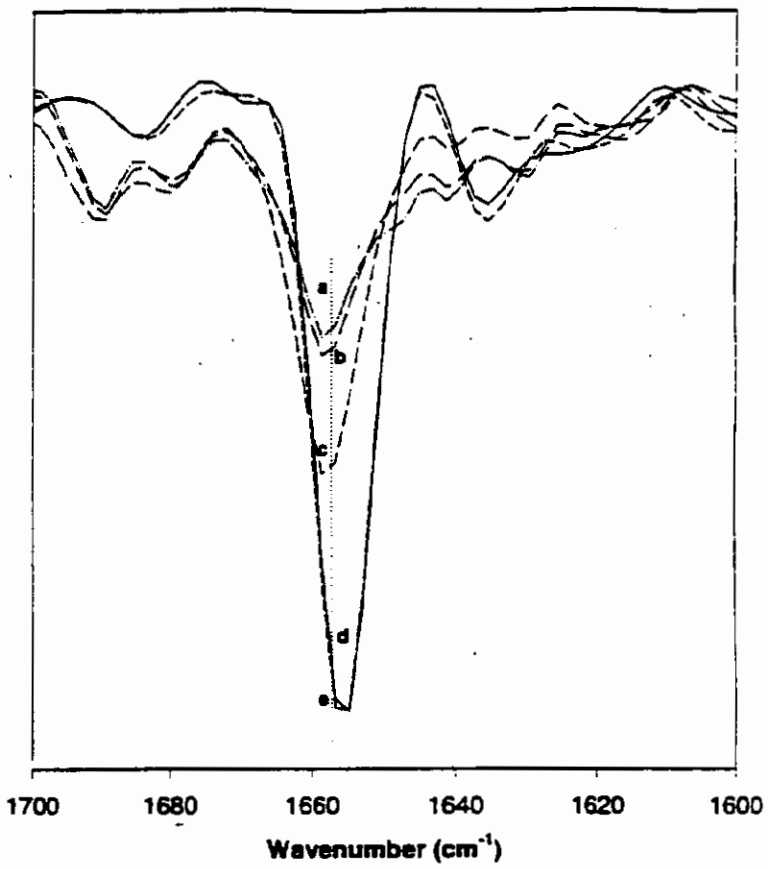

Figure 4: Effect of polyethylene glycol 3350 on the secondary structure of lyophilized hemoglobin: second derivative FTIR, amide I region. From top to bottom along dotted line: a) dried state spectrum, lyophilized in buffer salts only , b) dried state spectrum, lyophilized in 5%PEG3350, c) dried state spectrum, lyophilized in 10%PEG3350, d) example of liquid control, e) example of rehydrated sample.

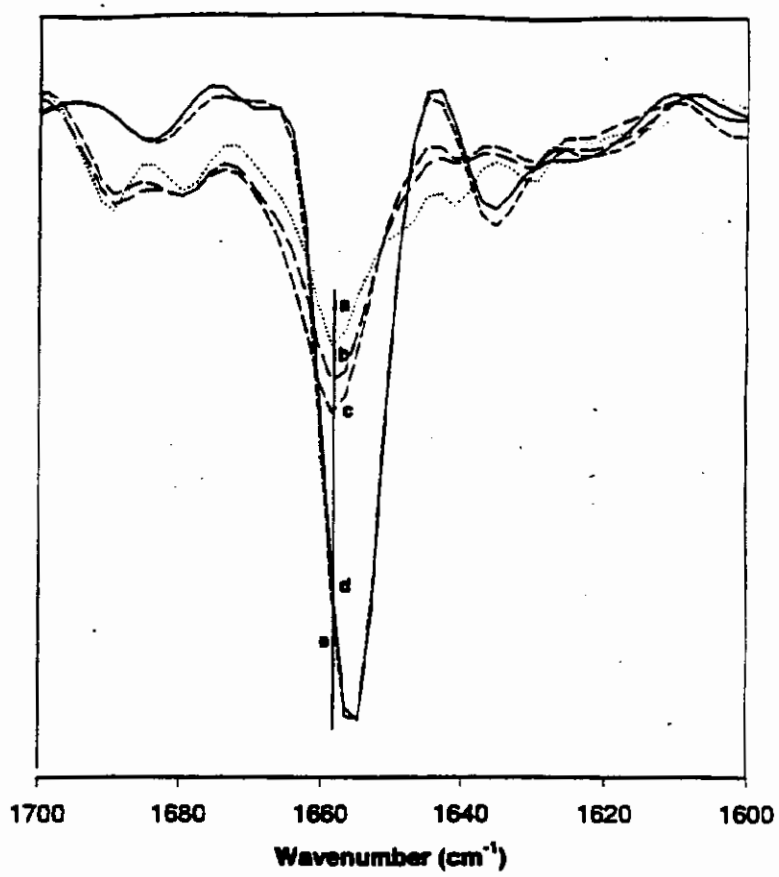

Figure 5: Effect of dextran500 on the secondary structure of lyophilized hemoglobin: second derivative FTIR, amide I region. From top to bottom along dotted line: a) dried state spectrum, lyophilized in buffer salts only, b) dried state spectrum, lyophilized in 4.5% dextran500, c) dried state spectrum, lyophilized in 9% dextran500, d) example of liquid control, e) example of rehydrated sample.

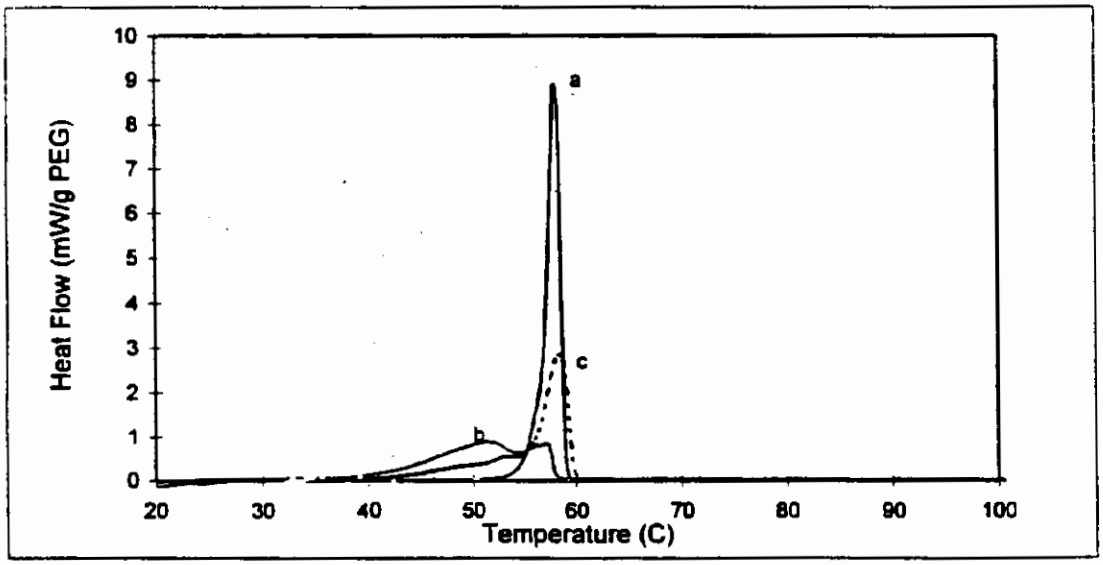

Figure 6: Crystallinity of PEG in lyophilized samples by differential scanning calorimetry. a) raw PEG3350, crystalline reference. b) hemoglobin lyophilized with 5%PEG3350. c) hemoglobin lyophilized with 10%PEG3350.

PURIFICATION OF RECOMBINANT HEPATITIS B VACCINE: EFFECT OF VIRUS/SURFACTANT INTERACTIONS

LaToya S. Jones and Theodore W. Randolph
Dept. of Chemical Engineering, University of Colorado, Boulder, CO-80309

Abstract

Recombinant Hepatitis B vaccine (rHBsAg) is a 22 nm 2.4 MDa particle produced in yeast and is comprised of surface proteins of the virus associated with lipids. A high degree of variability is seen in the purification process, thus making it a difficult one to optimize. Triton X-100 at various concentrations and incubation times is present in several purification stages. Through the use of a nitroxide spin probe and electron paramagnetic resonance (EPR) spectroscopy, interactions of rHBsAg and Triton X-100 have been studied. The vaccine prototype of rHBsAg was used. 16-DOXYL-stearic acid served as a spin probe. The stearic acid studies determined that the binding ratio of surfactant to vaccine particle is approximately 3000:1. A Triton X-100 concentration of 0.04% by weight is the critical concentration for these interactions to be detected.

Introduction

Plasma derived vaccines (PDV's) were the first generation vaccines against the hepatitis B virus (HBV), a DNA virus. The source of the vaccine particles was the plasma of chronically infected individuals. Although any infectious particles that might have been in the donated plasma were destroyed during purification, the PDV was not readily accepted by the public to the extent that the manufacturers desired. In addition, there was a concern about the future availability of suitable plasma. These factors led to the push to develop a recombinant vaccine (Ellis, 1991).

A yeast derived vaccine (YDV) is the current vaccine against HBV. Because the vaccine is purified from yeast, the major drawbacks of the PDV are overcome. The YDV is an intracellular product which requires a combination of separation techniques to purify it from the yeast fermentation broth (Stephenne, 1989). It is the first recombinant vaccine that received approval for use in humans (Ellis, 1991).

The vaccine particle for both the PDV and the YDV is the hepatitis B surface antigen (HBsAg). HBsAg is a 22 nm particle consisting of 100 surface proteins associated about a lipid core. The major form of the surface protein that exists in the vaccine particle is the S protein. The preS1 and preS2 proteins are found in relatively small concentrations in the PDV. Each S protein has a molecular weight of 24 kDa, thus, the molecular weight of a vaccine particle is in excess of 24 MDa. In the plasma of chronic carriers of HBV, the S protein is found associated with the viral particle and the separate HBsAg particle. The S proteins of the PDV are glycosylated; however, those of YDV lack glycosylation .

Efficacy studies have shown that this lack of glycosylation does not affect the immunogenicity of the vaccine (Kniskern and Miller, 1992). However, the amount of lipid that is associated with the protein in the vaccine causes variation in the immune response is the amount of lipid that is associated with the protein in the vaccine particle (Gavilanes *et al.*, 1990).

Non-ionic surfactants, such as Tritons, are added in the early stages of purifying both the HBsAg from PDV and rHBsAg from YDV. Factors such as surfactant concentration and incubation time of vaccine particle with the surfactant prior to and during chromatographic purification affect the amount of lipid in the final product. This is the motivation behind this research.

Materials

Triton X-100 and 16-DOXYL-stearic acid were purchased from Sigma Chemical Co. and were used without further purification. rHBsAg was supplied by Merck. All buffers were prepared using deionized water purified using a Barnsted water purification system. The buffer used in all experiments was 0.28 M NaCl 6 mM sodium phosphate buffer, pH 7.2.

Methods

Electron paramagnetic resonance (EPR) spectroscopy is the analytical tool used to monitor the rHBsAg Triton X-100 interactions. By measuring the rotation of a free radical, in this case 16-DOXYL-stearic acid, information about the environment of the spin probe can be deduced. Figure 1 illustrates the behavior of spin probe in the presence of increasing surfactant concentration. Figure 2 is the same scenario with the addition of another molecule, e.g., rHBsAg, which interacts with the surfactant. At surfactant concentrations below the critical micelle concentration (CMC), the rotation of the spin probe is not affected by the presence of the surfactant. Once micelles begin to form, some of the spin probes partition into the interior of the micelles. If there is a molecule in the solution that is interacting with the surfactant, the apparent CMC diminishes and the partitioning occurs at lower surfactant concentrations than in the absence of the additional molecule. The spectra obtained from the EPR contains signals from both the freely rotating and hindered spin probe.

Two sets of samples were prepared. Set one contained 10 μm 16-DOXYL-stearic acid, Triton X-100, and buffer. Set two was set one with 41.5 nM rHBsAg. The only variable in the experiment was the surfactant concentration, which ranged from 0.0% to 1.0% by weight. Spectra were also taken of rHBsAg in solution with varying amounts of 16-DOXYL-stearic acid to verify that the motion of the nitroxide was not influenced by the presence of the vaccine particle (data not shown). All data was collected at ambient temperature. Factor analysis, as described by Bam and Randolph (1994), was used to quantify the results.

Results and Discussion

The spectra in Figures 3 and 4 are representative spectra for Triton X-100 concentrations below the apparent CMC, slightly above the apparent CMC, and much above the CMC, in the absence and presence of rHBsAg, respectively. At low and high surfactant concentrations, the spectra for both sets of samples are almost identical. The three sharp peaks of the low surfactant concentration spectra indicate that the spin probe is rotating freely in solution. The broadened third peaks in the spectra of the samples containing 1.0% Triton X-100 indicate that the all of the spin probes are trapped in micelles and their rotational motions have been hindered. At a surfactant concentration of 0.05%, third peaks of the spectra in the figures are combinations of the other two extreme cases. The relative amounts of each type of spectra are directly proportional to the population of free and hindered spin probe, see Figure 5.

The consistently higher fraction of rotationally hindered label in the presence of rHBsAg in comparison to those without at identical Triton X-100 concentrations is indicative of vaccine - surfactant interactions. The difference of these two curves is plotted in Figure 6. The molar ratio of Triton X-100/rHBsAg corresponding to the greatest difference between the curves gives the binding stoichiometry. This binding stoichiometry of 3000:1 corresponds to a monolayer-like coverage of the vaccine particle.

Conclusions

There are indeed interactions between Triton X-100 and rHBsAg. It is likely that these interactions are the major causes of the variance in the purified vaccine particles. Although the stoichiometry of the interactions suggests monolayer coverage of the particle, further studies must be conducted to determine if this is indeed the case.

Acknowledgments

This research is supported by the National Science Foundation and Merck Corporation.

References

Bam, N. B., and T. W. Randolph, "Probing Surfactant-Protein Binding By EPR Spectroscopy," *Proceedings of the 24th Annual Biochemical Engineering Symposium*, 1994.

Ellis, R.W., "Recombinant Yeast-Derived Hepatitis B Vaccine: The Prototype for Biotechnologically Derived Old Vaccines," *Bioprocess-Technol.*, **13**, 355-369, 1991.

Gavilanes, F., Gomez-Gutierrez, J., Aracil, M., Gonzalez-Ros, J. M., Ferragut, J. A., Guerrero, E., and D. L. Peterson, "Hepatitis B Surface Antigen: Role of Lipids in Maintaining the Structural and Antigenic Properties of Protein Components," *Biochem. J.*, **265**, 857-864, 1990.

Kniskern, P. J., and W. J. Miller, "Hepatitis B Vaccines: Blueprints for Vaccines of the Future," *Vaccines: New Approaches to Immunological Problems*, 177-204, Ellis, R. W., Ed., Butterworth-Heinemann, Boston, 1992.

Stephenne, J., "Production in Yeast and Mammalian Cells of the First Recombinant DNA Human Vaccine Against Hepatitis B: A Technical and Immunological Comparison," *Advances in Animal Cell Biology and Technology for Bioprocesses*, 526-567, Spier, R. E., Griffiths, J. B., Stephenne, J., and P. J. Crooy, Eds., Butterworth & Co., 1989.

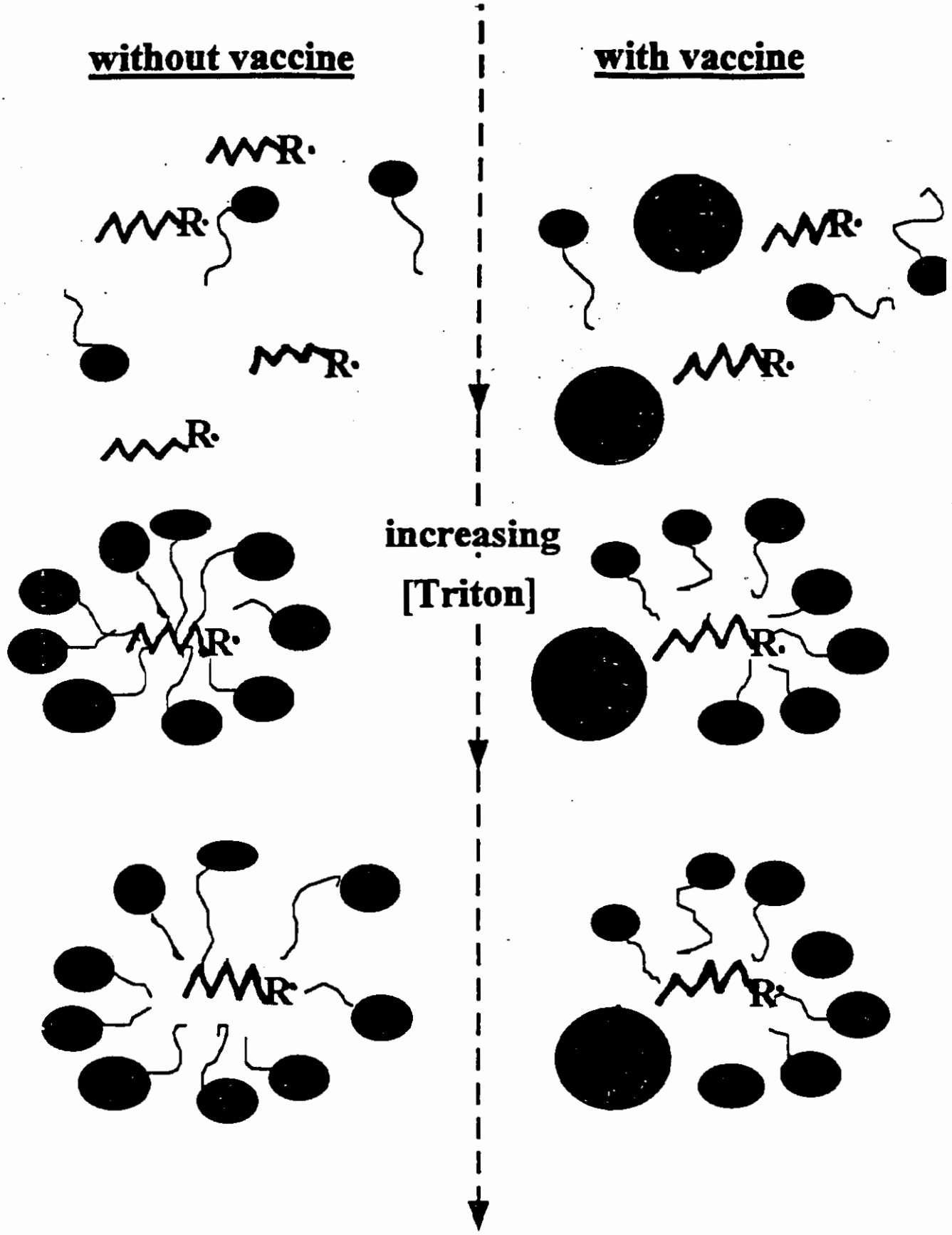

Figure 1: Mobility restrictions of free radicals in the presence of surfactant at increasing concentrations.

Figure 2: Same as Figure 1 with the addition of a particle which interacts with the surfactant.

Triton & 16-doxyl stearic acid

0.03%

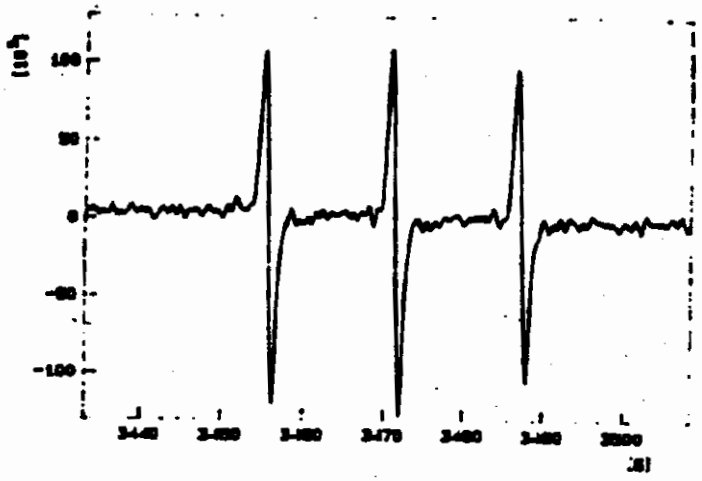

0.05%

1.0%

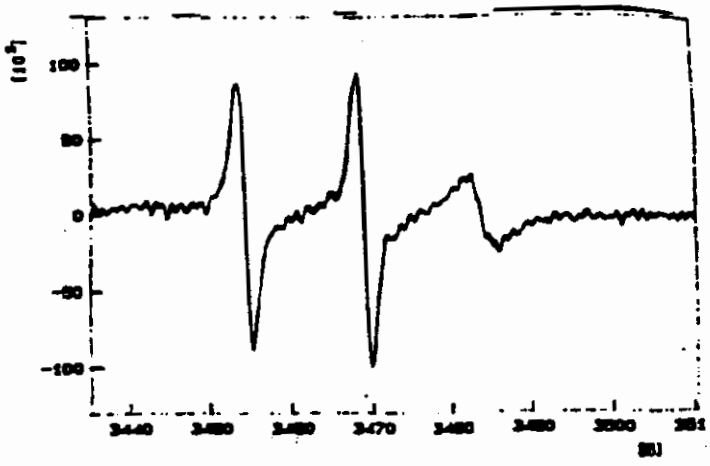

Figure 3: EPR spectra describing the motion of 16-DOXYL-stearic acid in the presence of Triton X-100 at three concentrations.

rHBsAg, Triton, & 16-doxyl stearic acid

0.03%

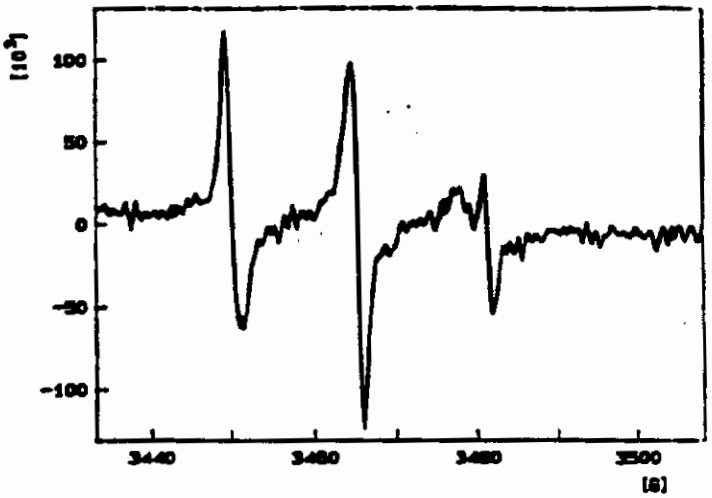

0.05%

1.0%

Figure 4: EPR spectra describing the motion of 16-DOXYL-stearic acid in the presence of rHBsAg and Triton X-100 at three concentrations.

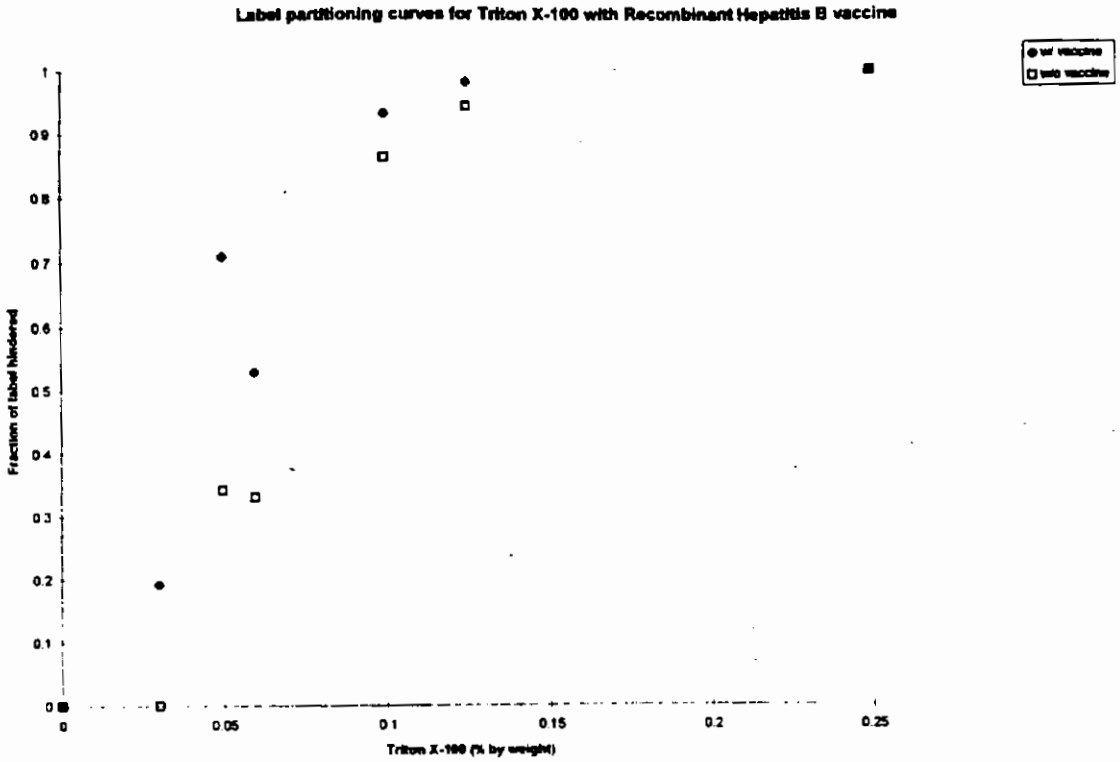

Figure 5: Curves representing the fraction of 16-DOXYL-stearic acid that has hindered motion in the absence and presence of rHBsAg.

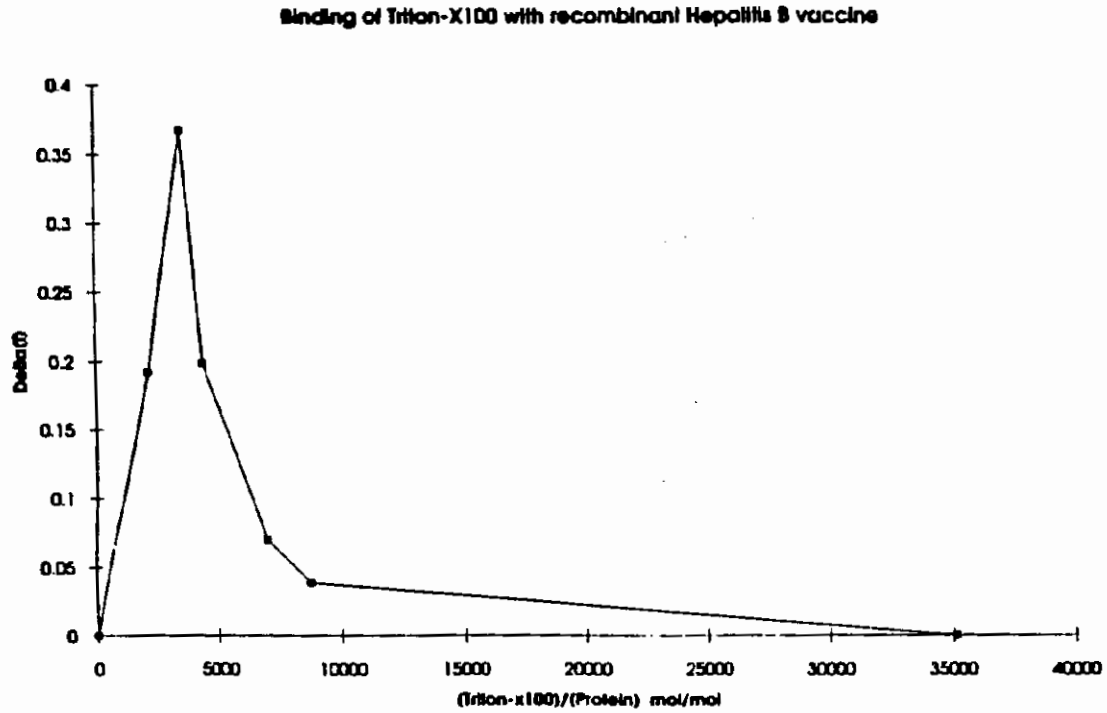

Figure 6: Binding stoichiometry of Triton X-100:rHBsAg.

Application of Osmotic Dewatering to the Crystallization of Oligonucleotides for Crystallography

Ching-Yuan Lee, Michael G. Sportiello, Stephen Cape, Sean Ferree, and Paul Todd,
Department of Chemical Engineering,

Craig E. Kundrot and Cindy Barnes,
Department of Chemistry and Biochemistry, University of Colorado, Boulder

Abstract

Rising interest in the application of oligonucleotides to medical problems has stimulated a need to determine the three-dimensional structures of oligonucleotides and their complexes with various ligands. Three-dimensional structure determination relies on high-quality crystals at least 0.5 mm in length; however, only about a dozen RNA molecules have been crystallized, and a broad record of experience in oligonucleotide crystallization is lacking. Osmotic dewatering is a crystallization method in which oligonucleotide and its precipitant are concentrated at a controlled rate by the removal of water through a reverse-osmosis membrane using a specified concentration gradient. A multi-chamber osmotic dewatering crystallizer was built and its transport characteristics were successfully modeled under conditions used for the crystallization of an oligonucleotide ("UU-dodecamer"), synthesized by *in vitro* transcription using bacteriophage T7 RNA polymerase and an immobilized DNA template and purified by gel electrophoresis. Crystals were grown with and without the removal of the terminal 5' triphosphate. The osmotic dewatering method was also tested in various devices during low-gravity space flights. Experiments to date lead to the conclusion that both the nucleation and growth stages of crystallization can be controlled by regulating the concentration gradient across a reverse-osmosis membrane during crystallization.

1. Introduction

Since the discovery of their catalytic properties in the early 1980's (Cech et.al., 1981, 1987), ribonucleic acids (RNA) have opened an era in potential development of pharmaceutical drugs. For example, Tuerk et. al. (1992) showed that a pseudoknot RNA molecule could inhibit DNA synthesis by human immunodeficiency virus type 1 (HIV-1) reverse transcriptase. Wu et. al. (1989) demonstrated that RNA had the potential for the treatment of hepatitis. However, the strategy of designing RNA drugs depends on the knowledge of the three-dimensional structures of the RNA molecules. The determination of RNA three-dimensional structures by x-ray crystallography, in turn, depends on the availability of high quality crystals. The growth of diffraction-quality RNA crystals is therefore critical.

Although the history of biological macromolecule crystal growth can be traced back to more than 150 years ago (McPherson, 1991), extensive experience in crystallizing

RNA molecules is lacking. Only about a dozen RNA molecules have so far been successfully crystallized (Doudna et.al, 1993). Methods for crystallizing biological macromolecules include batch crystallization, temperature gradient crystallization, equilibrium dialysis crystallization, and vapor phase diffusion. These methods, however, allow very limited control of the parameters involved in the nucleation and growth of macromolecule crystals. In 1990, Todd et. al. introduced a novel method for obtaining high quality crystals of biological macromolecules, namely osmotic dewatering crystallization. This method was successfully applied to growing lysozyme crystals which diffracted to 2.3Å (Todd et.al., 1990). It has, over the traditional methods, the advantages of controlling the rate of water removal, which affects both the nucleation and growth rate of crystals, adjustable extent of water removal, which dictates the sizes of crystals, and reducing convective flow, which is generally considered to be detrimental to the crystal quality.

In this work, we present an application of the osmotic dewatering technique to the crystallization of an oligonucleotide, the "U-U dodecamer". We developed a transport model of osmotic dewatering and successfully grew crystals of the target RNA molecule, U-U dodecamer.

2. Transport Model of Osmotic Dewatering

In osmotic dewatering, a reverse osmosis membrane is used to separate two solutions having different solute concentrations. The lower-concentration solution contains the species to be crystallized. Due to the osmotic pressure, resulting from the difference in osmolarity across the membrane, water from the low concentration solution permeates through the membrane into the high concentration solution. This dehydration, at a controllable rate, gradually concentrates the low concentration solution and causes crystallization to occur in the presence of a suitable precipitant. Figure 1 illustrates the concept.

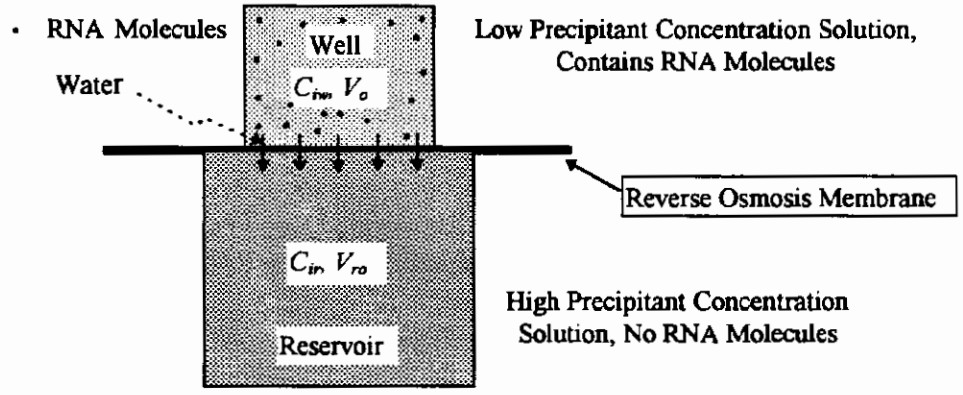

Figure 1. Concept of Osmotic Dewatering

The total pressure drop across the membrane can be represented by the sum of the gravity head and the Van't Hoff osmotic pressure for ideal solutions:

$$\Delta P = \rho g \Delta h + RT\Delta C$$

where ΔC is the total osmolarity difference across the membrane, R is the ideal gas constant, and T is the temperature, °K. A typical initial osmotic pressure is around 2 Mpa, while that due to the difference in fluid head is around 20 Pa. Therefore, the gravity head contribution is generally neglected.

The flux of water across a membrane is governed by Darcy's Law:

$$\frac{1}{A}\frac{dV}{dt} = \frac{RT}{\mu R_m}\sum_{i=n}\Delta C_i \qquad (1)$$

where A is the cross-sectional area of the reverse osmosis membrane (m^2), V is the volume of water that has permeated through the membrane (m^3), at time t, t is the time (hours), n is the number of solutes, μ is the viscosity of fluid (Pa-hr), and R_m is the membrane resistance (m^{-1}).

$$\text{Let} \quad \Delta C_i = C_{ir} - C_{iw} \quad \text{and} \quad R_i = \frac{C_{iwo}}{C_{iro}} \qquad (2)$$

where C_{ir} is the total osmolarity of species i in the reservoir (osmoles/m^3), C_{iw} is the total osmolarity of species i in the well (osmoles/m^3), C_{iro} is the initial total osmolarity of species i in the reservoir (osmoles/m^3), C_{iwo} is the initial total osmolarity of species i in the well (osmoles/m^3), and R_i is the ratio of initial well concentration to initial reservoir concentration of species i.

At time t,

$$C_{ir}(V_{ro} + V) = C_{iro}V_{ro} \quad \text{and} \quad C_{iw}(V_o - V) = C_{iwo}V_o$$

where V_{ro} is the initial reservoir volume (µl), and V_o is the initial well volume (µl). Therefore,

$$C_{ir} = \frac{V_{ro}}{V_{ro} + V}C_{iro} \qquad (3)$$

$$C_{iw} = \frac{V_o}{V_o - V}C_{iwo} = \frac{V_o}{V_o - V}R_iC_{iro} \qquad (4)$$

Combining equations (2), (3), and (4), we have

$$\Delta C_i = \frac{V_{ro}}{V_{ro} + V}C_{iro} - \frac{V_o}{V_o - V}R_iC_{iro}$$

and

$$\sum_{i=n} \Delta C_i = \frac{V_{ro}}{V_{ro}+V} \sum_{i=n} C_{iro} - \frac{V_o}{V_o - V} \sum_{i=n} R_i C_{iro} \qquad (5)$$

Let $\sum_{i=n} C_{iro} = C_{ro}$ and $\sum_{i=n} R_i C_{iro} = k$

where C_{ro} is the total osmolarity of all solutes in the reservoir (osmoles/m^3), and k is a constant (osmoles/m^3).

Therefore

$$\sum_{i=n} \Delta C_i = \frac{V_{ro}}{V_{ro}+V} C_{ro} - \frac{V_o}{V_o - V} k \qquad (6)$$

The viscosity, μ, was measured over the range of different solution concentrations at constant temperature, 310°K, and was approximated by the following equation.

$$\mu = aM_w + b \qquad (7)$$

where M_w is the total molarity in the well solution and a and b are constants.

Substituting M_w with M_{wo}, we have

$$\mu = aM_{wo} \frac{V_o}{V_o - V} + b \qquad (8)$$

where M_{wo} is the total initial molarity in well solution.

Combining equations (1), (6), and (8), we obtain

$$\frac{dV}{dt} = \frac{ART}{R_m} \frac{\frac{V_{ro}}{V_{ro}+V} C_{ro} - \frac{V_o}{V_o - V} k}{aM_{wo} \frac{V_o}{V_o - V} + b}$$

Let $K_1 = \frac{ART}{R_m}$

Rearranging the above equation, we obtain

$$\frac{(aM_{wo}+b)V_o V_{ro} + (aM_{wo}V_o + bV_o - bV_{ro})V - bV^2}{(C_{ro}-k)V_o V_{ro} - (C_{ro}V_{ro} + kV_o)V} dV = K_1 dt$$

Let $\alpha = \frac{V_o}{V_{ro}}$

Dividing the above equation by $V_o V_{ro}$, and rearranging, we get

$$\frac{(aM_{wo}+b)+(aM_{wo}\alpha+b\alpha-b)\left(\frac{V}{V_o}\right)-b\left(\frac{V}{V_o}\right)^2}{(C_{ro}-k)-(C_{ro}+k\alpha)\left(\frac{V}{V_o}\right)}dV = K_1 dt$$

By separating the above equation into 3 parts and integrating them separately, with the initial condition that at $t=0$, $V=0$, we obtain:

$$\left[\frac{(C_{ro}-k)^2 b\alpha V_o}{(C_{ro}+k\alpha)^3}-\frac{(aM_{wo}\alpha+b\alpha-b)(C_{ro}-k)V_o}{(C_{ro}+k\alpha)^2}-\frac{(aM_{wo}+b)V_o}{C_{ro}+k\alpha}\right]\ln\left[1-\left(\frac{C_{ro}+k\alpha}{C_{ro}-k}\right)\left(\frac{V}{V_o}\right)\right]+$$
$$\left[\frac{(C_{ro}-k)b\alpha V_o}{(C_{ro}+k\alpha)^2}-\frac{(aM_{wo}+b\alpha-b)V_o}{C_{ro}+k\alpha}\right]\left(\frac{V}{V_o}\right)+\frac{b\alpha V_o}{2(C_{ro}+k\alpha)}\left(\frac{V}{V_o}\right)^2=\frac{ART}{R_m}t,$$

the Transport Equation for Osmotic Dewatering (TEFOD). Although TEFOD appears complicated, most of the terms are either constants or measurable values based on the actual experimental conditions.

3. Experimental

3.1 Materials

The structures of U-U dodecamer are shown in figure 2.

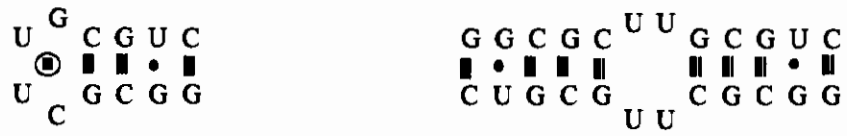

In Low Salt Concentration- Hairpin In High Salt Concentration- Double Stranded

Figure 2. Structures of U-U Dodecamer

U-U dodecamer was obtained by *in vitro* transcription using bacteriophage T7 RNA polymerase and immobilized DNA templates (Marble and Davis, 1995). Each 1-ml reaction contained 40 mM Tris (pH 8.1), 20 mM magnesium acetate, 5 mM dithiothreitol (DTT), 1 mM spermidine, 0.01% triton X-100, 6.4 mM cytidine triphosphate (CTP), 4.8 mM uridine triphosphate (UTP), 8.0 mM guanidine triphosphate (GTP), 0.05 mg/ml T7 RNA polymerase, and 1.0 μM immobilized DNA template. The reactions were carried out at 37°C for about 5 hours. The reaction supernatant was ethanol precipitated and resuspended in water. A stir cell with a 1000 molecular weight cut off membrane (YM1, Amicon) was used to desalt the RNA broth. Calf intestinal alkaline phosphatase (CIAP) was then added to cleave the triphosphate group at the 5'-end of RNA molecules and replace it with a hydroxyl group (Kundrot, 1995). This enzymatic reaction was carried out at 37°C for one hour and stopped by adding 1/10 volume of 500 mM EDTA and raising the temperature to 65°C for 10 minutes. The desired U-U dodecamers were then

purified from this reaction mixture by gel electrophoresis with a 20% polyacrylamide gel. RNA product was extracted from the gel by crushing the gel with a mortar and pestle and eluting with an elution buffer containing 10 mM Tris, 1mM EDTA, and 500 mM NaCl. The elution process was usually repeated 3 times (5ml buffer each time) for maximum product recovery. The total eluent was then concentrated and desalted by using the stir cell membrane. A typical final yield of dodecamer from a 1-ml reaction was between 350 μg and 400 μg. The final product in pure water was stored at -20°C until used in crystallization experiments.

3.2 Multi-Chamber Crystallizer

The schematic diagram of a multi-chamber crystallizer is shown in figure 3.

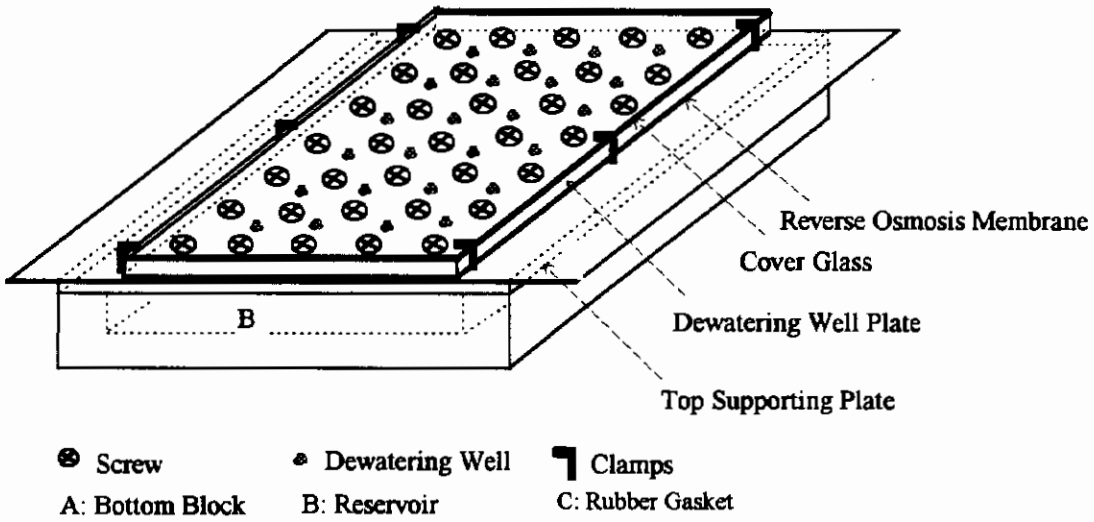

Figure 3. Schematic drawing of a Multi-Chamber Crystallizer

There are a total of 24 osmotic dewatering wells. Each well holds up to 30 μl of fluid. The volume of the reservoir is about 62 ml. The reservoir and top supporting plate are made of polycarbonate plastic, the dewatering well plate is made of delrin, and the clamps are made of aluminum. They were all machined at the Chemical Engineering Departmental machine shop by Mr. Willy Grothe.

3.3 Dewatering Rate Measurements

Dewatering rate experiments were carried out at 37°C. The reservoir solution contained 10% (wt%) methyl 2,4 pentane diol (MPD, Sigma Chemicals, Inc. St. Louis, MO), 400 mM ammonium acetate, 25 mM magnesium chloride, and 50 mM sodium cacodylate (pH 7.0). The starting concentrations of all the solutes in the solution for all the dewatering wells were exactly 50% of the those in the reservoir solution. After assembling the multi-chamber crystallizer, the reservoir solution was loaded first to saturate the RO membrane (MS-10,Osmonics, Inc., Minnetonka, MN) overnight. The following morning, 30 μl of well solution were loaded into each dewatering well. The

remaining volumes of the well solutions were measured in each well at various time points to obtain the dewatering rate data.

3.4 Crystallization

The same compositions of both reservoir and well solutions as described in 3.3 were used for crystallization experiments, except that different concentrations of dodecamer were added to the well solution. After assembling the crystallizer, reservoir solution was added to saturate the membrane overnight. Well solutions were added the next day. A typical crystallization experiment had 4 different initial dodecamer concentrations, 0.6 mg/ml, 0.7 mg/ml, 0.8 mg/ml, and 0.9 mg/ml. Each concentration of RNA-containing well solution was loaded into 6 wells, 15 µl per well. The duration of the experiment was at least 7 days. At the end of the experiment, the remaining solution from each well was harvested into a depression slide by using a microdispenser (Drummond) and glass pipettes. Each solution was then examined under the microscope for evidence of crystals or crystalline materials.

4. Results

4.1 Dewatering Rate Measurement

Under the experimental conditions, the total well solution volume is 720µl. Compared with the reservoir solution volume 62ml, we have $V_{ro} >> V_o$, and, therefore, $\alpha \cong 0$. Since the initial total osmolarity in the well solution is exactly half of that in the reservoir solution, we have $k = 0.5C_{ro}$. Applying these two values to TEFOD, the equation can be simplified to

$$-[\frac{(2aM_{wo} + b)V_o R_m}{2ARTC_{ro}}]\ln(1 - 2\frac{V}{V_o}) + (\frac{bR_m V_o}{ARTC_{ro}})\frac{V}{V_0} = t \qquad (9)$$

The viscosity of a fluid is a function of temperature and composition of the fluid. In a dewatering experiment, the concentrations of solutes in the well solution increase as the volume of the well solution decreases. Therefore, the viscosity of the well solution is not a constant. Viscosity data of the well solution at different concentrations were measured and shown in Figure 4. The two constants in equation (7) were determined to be $a = 2 \times 10^{-10}$, $b = 5 \times 10^{-8}$.

The manufacturer's membrane resistance, R_m, depends not only on the properties of the membrane materials but also on the characteristics of the contacting fluids. Therefore, this value was determined empirically. From experimental data, at $t = 10$ hour, V was measured as 8.125µl or 8.125×10^{-9}m^3. Substituting these two numbers and the above constants, R_m was determined to be 4.858×10^{16}m^{-1}. Other constants were $A = 7.92 \times 10^{-6}$ m^2, $R = 8.314$ J/°K-sec, $T = 310$°K, $M_{wo} = 1321$ moles/m^3, and $C_{ro} = 1800$ moles/m^3.

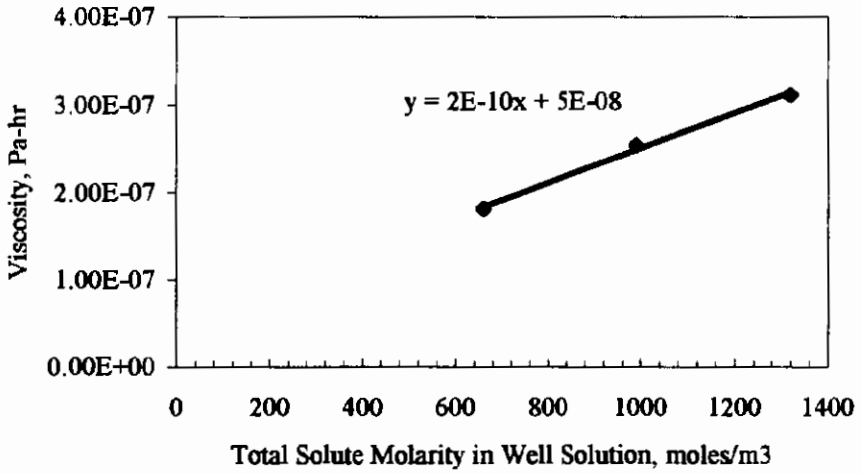

Figure 4. Viscosity as a Function of Total Solute Concentration

Therefore equation (9) becomes

$$-11.58\ln(1-2\frac{V}{V_0})+3.69\frac{V}{V_0}=t \qquad (10)$$

Equation (10) was then plotted and compared with two sets of experimental data. The result is shown in Figure 5.

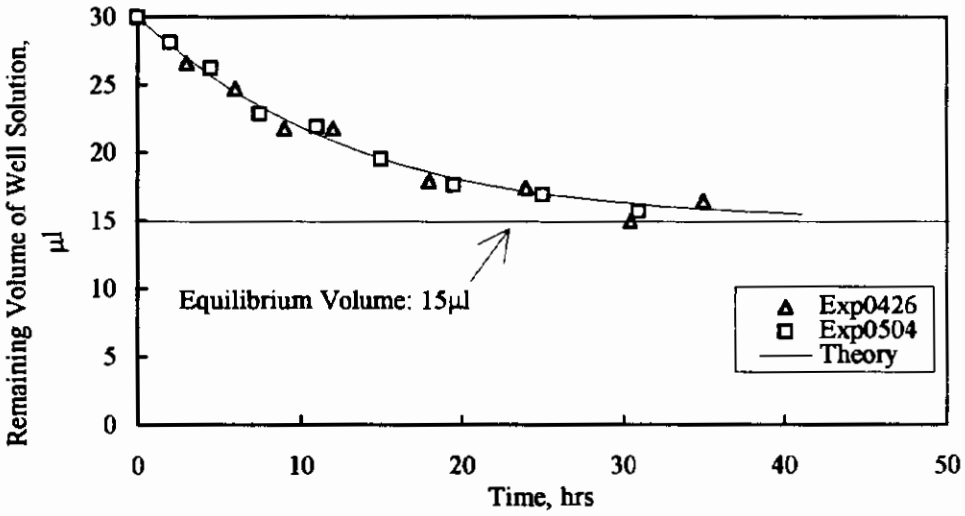

Figure 5. Comparison of Theoretical and Experimental Osmotic Dewatering Rate in Replicate Experiments Using the Multi-Chamber Crystallizer

4.2 Crystallization Experiments

Several crystallization experiments were performed, and dodecamer crystals were successfully obtained. Dodecamer molecules used in earlier experiments had a

triphosphate group on their 5'end. (In other words, CIAP reactions were not applied.) In later experiments, the dodecamer molecules were treated with CIAP, producing molecules with a hydroxyl on the 5' end. Therefore two types of crystal morphologies were observed, as shown in Figures 6 and 7. The triphosphate dodecamer crystals display a so-called "coffin" shape as shown in figure 6. The hydroxyl dodecamer crystals tend to form twin crystals and display a "V" shape, as shown in figure 7.

Figure 6. Triphosphate Dodecamer Crystals. (——— 100μm)

Figure 7. Hydroxyl Dodecamer Crystals. (———100μm)

5. Conclusions

A transport model was developed to describe the osmotic dewatering process. As shown in figure 5, with R_m the only fitted parameter, this model successfully predicted the dewatering rate in the crystallizer. This model will be very helpful in controlling the dewatering rate by controlling the total osmolarity difference across the membrane. This, in turn, enables the control of both the nucleation and crystal growth rates, which play important roles in crystal size and quality.

U-U dodecamer molecules were successfully crystallized in the multi-chamber crystallizer. However, the sizes of the crystals obtained so far were not adequate for mounting for x-ray diffraction analysis. In order to get x-ray diffraction data to determine the quality of crystals, further improvement in the experimental strategies are needed to improve the size of the crystals.

6. Acknowledgments

This work has been sponsored by NeXstar, the Colorado RNA Center, the Whitaker Foundation, Instrumentation Technology Associates, and the National Aeronautics and Space Administration (Grant NAGB-1167).

7. References

Cech, T.R.; Zaug, A.J.; Grabowski, P.J., "In vitro splicing of the ribosomal RNA precursor of tetrahymena: Involvement of a guanosine nucleotide in the excision of the intervening sequence", Cell, Vol. 27, p487 (1981)

Cech, T.R., "The chemistry of self-splicing RNA and RNA enzymes", Science, Vol. 236, p1532, 1987

Doudna, J.A.; Grosshans, C.; Gooding, A.; Kundrot, C.E., "Crystallization of RNA enzymes and small motifs using a novel sparse matrix approach", Proc. Natl. Acad. Sci. USA, 1993

Kundrot, C.E., "The preparation and crystallization of RNA: a sparse matrix approach", Methods in Enzymology, in press, 1995

Marble, H.A.; Davis, R.H, "RNA transcription from Immobilized DNA templates", Biotechnology Progress, Vol 11, p393, 1995

Todd, P.; Sikdar, S.K.; Walker C.; Korszun Z.R., "Application of osmotic dewatering to the controlled crystallization of biological macromolecules and organic compounds", Journal of Crystal Growth, Vol 110, p283, 1991

Tuerk, C.; MacDougal S.; Gold, L.; "RNA pseudoknots that inhibit human immunodeficiency virus type 1 reverse transcriptase", Proc. Natl. Acad. Sci. USA, Vol 89, p6988, 1992

Wu, H.N.; Lin, Y.J.; Lin, F.P.; Makina, S.; Chang, M.F.; Lai, M.M.C., "Human hepatitis δ virus RNA subfragments contain an autocleavage activity", Proc. Natl. Acad. Sci. USA, Vol. 86, p1831, 1989

Production of Protein-Rich Beverages from Cheese Whey and Soybean by Rapid Hydration Hydrothermal Cooking

Xueou Deng, L. E. Erickson, and D. Y. C. Fung

Food Science Program
Department of Chemical Engineering
Kansas State University
Manhattan, KS 66506

ABSTRACT

Experiments have been conducted with Rapid Hydration Hydrothermal Cooking (RHHTC) process for a slurry composed of 5.6% soy flour and 94.4% cheese whey to investigate the effect of cooking temperature on product sterility and suspension stability. Whey-soy milk produced at a temperature of 141 °C with a mean residence time of 55 seconds or longer was found to be sterile. The shelf-life of the whey-soy milk was studied under refrigeration temperature. During the 30 days of storage, there was no bacterial growth and no observed change in chemical and physical properties except for the suspension stability.

INTRODUCTION

Soybeans are rich sources of high quality protein, and they are widely available with a world production of over 100 million metric tons per year. Because they are much less expensive than milk when compared on a dry or nutritional basis, developing protein-rich products from soybeans is potentially important to the food industry. Studies on the production, properties and acceptability of a nutritious beverage base from soy flour, soy oil, maize syrup solids, and fluid sweet cheese whey were conducted by Holsinger et al. (1974, 1977). Shirai et al. (1992) have made a yogurt-like product from soy-milk, oat flour, and dried cheese whey and evaluated its sensory and physical attributes.

The rapid hydration hydrothermal cooking (RHHTC) process which was developed at Kansas State University (Johnson, 1978), is a highly efficient continuous process with a 11.3 m long holding tube as its main heating section. A mixture of steam and feed slurry is passed rapidly through the holding tube with residence time ranging from 20-200 seconds at temperatures ranging from 121 to 157 °C to achieve complete sterilization. The RHHTC method which has been used to produce soy milk

from soy flour, has been studied by several investigators at Kansas State University (Buono, 1988; Hung, 1984; Johnson, 1978; Johnson et al., 1981; Tuitemwong, 1992; Tuitemwong et al., 1993a; 1993b).

In this research work, new fundamental knowledge is reported for producing protein-rich beverages from soybeans and cheese whey by the RHHTC process.

MATERIALS AND METHODS

FORMULATION AND PRODUCTION OF WHEY-SOY MILK

Full fat soybean flour was mixed with sweet cheddar cheese whey to form a whey-soy slurry. Before each experimental run, the procedure was started by introducing clean tap water to the system through the screw feeder. Then, the steam valve (see Figure 1) was opened to let the steam mix with the water and go through the system. The system was kept running for at least 30 min., and the equipment was completely sterilized. The desired flow rate, cooking temperature, and pressure were obtained by adjusting the speed of the Moyno pump and the outlet control valve (see Figure 1).

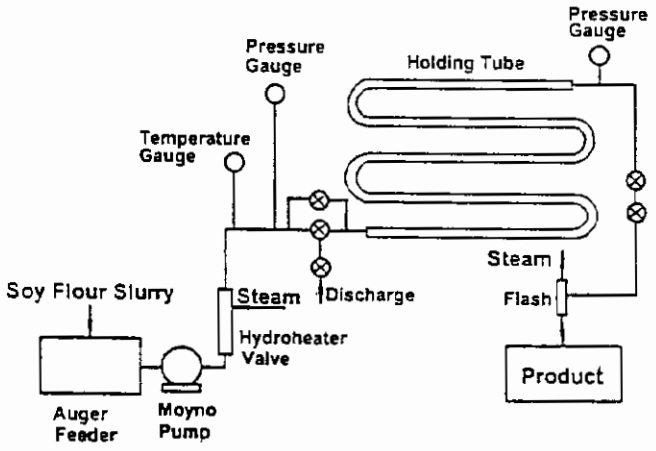

Figure 1. Rapid Hydration Hydrothermal Cooking Unit.

When the operation was under steady state conditions for about 10 min., the tap water was suddenly replaced with the prepared whey-soy slurry. Since the slurry has almost the same heat capacity as water, the steady state condition of the operation usually is not disturbed significantly by switching from water to the slurry. Samples of the cooked whey-soy slurry product were then collected at the flash unit.

RESIDENCE TIME DISTRIBUTION

The RHHTC system was running at a temperature of 149 °C and pressure of 69 psi. Hot samples were collected at the outlet of the flash evaporator every 10 seconds. For each experimental run, 14 samples were collected and cooled to room temperature in closed glass containers for future analysis of their total solids content. The data were reported using the mean of the elapsed time for each sample collected.

STORAGE STABILITY

To evaluate the microbiological shelf-life and the product suspension stability of the whey-soy milk, the milk produced at different cooking temperatures was stored at 5 °C. The evaluations started from day 0 and ended at day 30. The microbiological quality during the 30 days of storage was investigated by measuring the change of total viable bacteria. The pH of the milk as a function of storage time was measured.

The suspension stability of the milk was carried out in a 500 ml glass cylinder (30 cm height and 4.5 cm diameter) with precision scales; the cylinder was placed in a refrigerator at 5 °C with no agitation. At day 30, the solids content of each of the samples taken from different parts of the glass cylinder was measured to determine the solids distribution of the whey-soy milk.

RESULTS AND DISCUSSION

RESIDENCE TIME DISTRIBUTION

Figure 2 shows the residence time distribution (RTD) for the RHHTC process operating with whey-soy slurry at 149 °C. As shown in the graph, the mean residence time for this operating condition is about 65 seconds. In an ideal plug flow reactor, fluid elements fed in at the entrance at the same moment should come out of the reactor at the same time, which means that reacted or cooked fluid elements are not mixed with fresh ones from another time. Thus, an ideal plug flow reactor has the highest cooking and sterilization efficiency. As shown in the figure, the RTD curve of the RHHTC processor is very close to that of an ideal plug flow reactor. Thus, the RHHTC processor is a very efficient reactor.

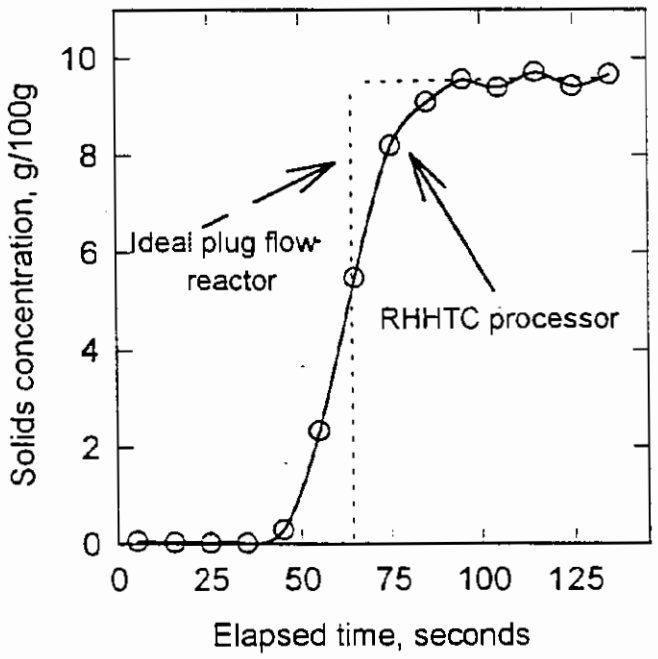

Fig. 2. Residence time distribution of RHHTC process operating with whey-soy slurry at a temperature of 149 °C. A step change in the solids content of the feed was made at t = 0.

MICROBIAL QUALITY AND THE CONDITIONS OF STERILIZATION

As shown in Table 1, the RHHTC system can be operated at several combinations of time, temperature, and pressure to produce completely sterilized whey-soy milk. However, to be safe, a temperature higher than or equal to 141 °C, a retention time longer than or equal to 55 seconds, and a pressure higher than or equal to 55.5 psi. are recommend for cooking the whey-soy slurry.

Table 1. Microbial Quality of Whey-Soy Milk
Produced by RHHTC Processing

Temperature °C (°F)	Mean retention time (seconds)	Pressure (psi)	Final bacterial number (CFU/ml)
112 (234)	31	20.0	253
117 (242)	29	24.0	14
131 (267)	37	39.0	10
136 (276)	49	46.0	0
141 (286)	55	55.5	0
146 (295)	63	62.0	0
152 (305)	90	74.0	0

CHEMICAL AND PHYSICAL PROPERTIES

Table 2 reports the solids content in the slurry before and after cooking. The dilution effect can be quantified by defining the relative change of solids content C^*,

$$C^* = \frac{C_0 - C}{C_0}$$

where C_0 is the solids content of whey-soy slurry before cooking and C is the solids content of the whey-soy milk after cooking. Since more steam is required to achieve a higher operating temperature, whey-soy slurry treated at a higher temperature is diluted. Thus, the relative change of solids content increases as the operating temperature is increased.

Table 2. Effect of RHHTC Processing Temperature on Solids Concentration of Whey-Soy Milk

Temperature °C (°F)	Slurry solids content (g/100g)	Whey-soy milk solids content (g/100g)	Relative change of solids content
138 (280)	10.74	8.55	0.204
131 (267)	10.79	8.68	0.195
122 (252)	10.69	8.84	0.173
117 (242)	10.88	9.07	0.166
112 (234)	10.715	8.96	0.164

The effect of RHHTC process temperature on protein content of whey-soy milk is shown in Table 3. The action of steam infusion cooking under the RHHTC conditions results in less damage to the protein (Hung, 1984).

Table 3. Effect of RHHTC Processing Temperature on the Protein Content of Whey-Soy Milk

Temperature °C (°F)	Whey-soy milk solids content (g/100g)	Protein content on wet basis (g/100g)	Protein content on dry basis (g/100g)
149 (300)	9.17	2.78	30.3
138 (280)	8.55	2.60	30.4
131 (267)	8.68	2.69	31.0
25[a] (77)	10.69	3.48	32.6

[a] Whey-soy slurry (uncooked milk).

STORAGE STUDY

After one month of storage at 5 °C, there was no visible color change, no significant change in pH, and no microbial growth. These results indicate that the heat treatment through RHHTC was adequate to control the microorganisms.

Figures 3 and 4 show the solids distribution in the milk stored for 30 days. Samples treated at 143 °C had a larger difference in solids content between the upper and lower layers, compared to samples treated at 152 °C. The degree of heat and pressure affects the stability of dispersions. Prior work has shown that the RHHTC process reduces the size of the fat globules (Tuitemwong, 1992). The protein-lipid droplets might increase the gel viscosity (Hong, 1989).

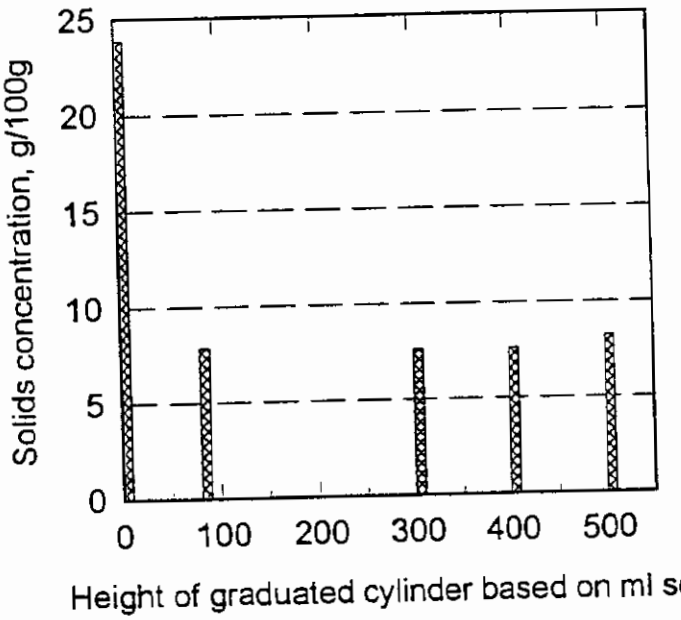

Fig. 4. Solids content distribution of whey-soy milk cooked at 143 °C and stored at 5 °C for 30 days.

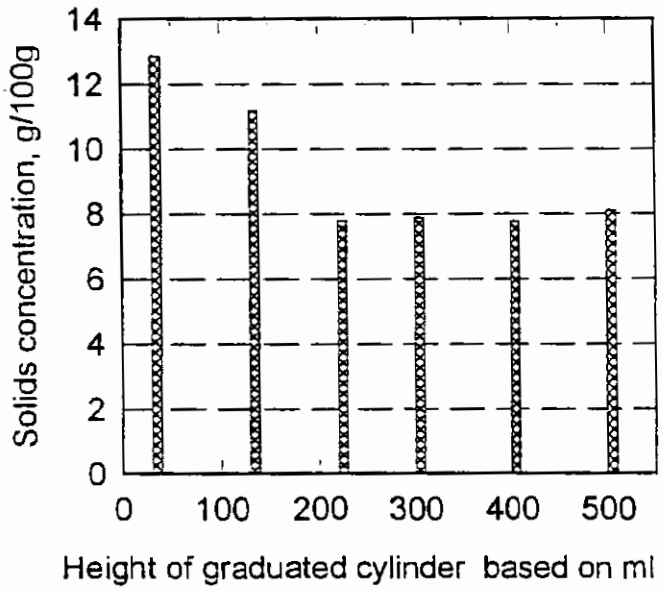

Fig. 3. Solids content distribution of whey-soy milk cooked at 152 °C and stored at 5 °C for 30 days.

CONCLUSIONS

Production of protein-rich beverages from cheese whey and soybeans by the RHHTC process is feasible. A process temperature higher than or equal to 141 °C, a retention time longer than or equal to 55 seconds, and a pressure higher than or equal to 55.5 psi. are recommended for cooking the whey-soy slurry to obtain a completely sterilized milk. Under refrigeration conditions, microbial quality and chemical stability are very good within one month, but the suspension stability is poor.

REFERENCES

Buono, M. A., 1988. An Engineering, Microbiology, and Sensory Study of Yogurt from Soy Milk. Ph.D. Dissertation, Kansas State University, Manhattan, KS.

Holsinger, V. H., C. S., Sutton, L. F. Edmondson, P. R. Crowley, B. L. Berntson, and M. J. Pallansch, 1974. Production and properties of a nutritious beverage base from soy products and cheese whey. IV International Congress of Food. Sci. and Techn. 8a, 16-17.

Holsinger, V. H., C. S. Sutton, H. E. Vettel, C. Allen, and F. B. Talley, 1977. Acceptability of whey-soy drink mix prepared with cottage cheese whey. J. of Dairy Sci. 60 (12), 1841-1845.

Holsinger, V. H., 1978. Fortification of soft drink with protein from cottage cheese whey. In Nutritional Improvement of Food and Feed Protein, ed. M.Friedman, Plenum Press, New York and London, pp. 735-748. -

Hong, K., 1989. Factors Affecting Viscosity of Soybean Milk Processed By Rapid Hydration Hydrothermal Cooking (RHHTC) Method. Ph.D. Dissertation, Kansas State University, Manhattan, KS.

Hung, J. S., 1984. Studies on Processing, Functional Characteristics and Nutritional Quality of Hydrothermal Extracts of Soybeans. Ph.D. Dissertation, Kansas State University, Manhattan, KS.

Johnson, L., 1978. Proessing Aqueous Extracts of Soybeans by Rapid-hydration Hydrothermal Cooking. Ph.D. Dessertation, Kansas State University.

Johnson, L., C. W. Deyoe and W. J. Hoover, 1981. Yield and quality of soymilk processed by steam-infusion cooking. J. Food. Sci. 46, 139-143.

Shirai, K., D. M. Gutierrez, V. Marshall, M. S. Revah, and G. M. Garcia, 1992. Production of a yogurt-like product from plant foodstuffs and whey, sensory evaluation and physical attributes. J. Sci. of fd. and Agri.59 (2), 205-210.

Tuitemwong, P., 1992. Sensory and Chemical Characteristics of Soy Yogurt and Frozen Soy Yogurt

Produced from Rapid Hydration Hydrothermal Cooked Soy Milk. Ph.D. Dissertation, Kansas State University.

Tuitemwong, P., L. E. Erickson D. Y. C. Fung, C. S. Setser, and S. K. Perng. 1993a. Sensory analysis of soy yogurt and frozen soy yogurt produced from rapid hydration hydrothermal cooked soy milk. J. Quality Foods, 16, 223-239

Tuitemwong, P., L. E. Erickson, D. Y. C. Fung, and K. Tuitemwong, 1993b. Effect of processing temperatures on microbiological and chemical quality of soy milk produced by rapid hydration hydrothermal cooking. J. of Food Processing Preserv. 17, 153-175.

Automated Docking of Glucoamylase Substrates and Inhibitors

Pedro M. Coutinho,[1] Michael K. Dowd,[2] and Peter J. Reilly[1]
[1]Department of Chemical Engineering, Iowa State University, Ames, IA 50011 and [2]Southern Regional Research Center, U.S. Department of Agriculture, New Orleans, LA 70179

Introduction

Glucoamylase (GA) is an exo-hydrolase that in nature produces glucose from the non-reducing ends of starch and maltooligosaccharide molecules. It can cleave all α-linked bonds between two glucosyl residues, with rates decreasing in the order α-(1→4) (maltose), α,β-(1→1) (α,β-trehalose), α-(1→6) (isomaltose), α-(1→3) (nigerose), and α-(1→2) (kojibiose) (Meagher and Reilly, 1989). GA cannot cleave β-linked bonds. At the high concentrations of partially hydrolyzed starch used as raw material in industry, GA produces appreciable amounts of all these disaccharides (Nikolov *et al.*, 1989), but chiefly isomaltose, and smaller amounts of oligosaccharides, reducing glucose yield to about 96% of theoretical. This is a serious problem, given the high tonnage of glucose produced as an intermediate in the high-fructose sweetener process.

Aspergillus awamori/niger GA is composed of two domains: catalytic (467 amino acid residues) and starch-binding (108 residues), separated by a 41-residue, highly glycosylated linker. The catalytic domain is composed of thirteen helices, twelve of them in an $(\alpha,\alpha)_6$ barrel (Aleshin *et al.*, 1992). The active site is in a funnel-shaped well, with Glu179 (Sierks *et al.*, 1990) serving as the catalytic acid and Glu400 (Harris *et al.*, 1993) serving as the catalytic base. It holds maltose, its primary substrate, in a different mode than it holds isomaltose (Coutinho and Reilly, 1994).

We have been subjecting GA to site-directed mutagenesis to improve its selectivity toward glucose production (essentially to increase its ability to hydrolyze and synthesize maltose and/or decrease its ability to hydrolyze and synthesize isomaltose) (Sierks *et al.*, 1993). Automated docking of substrates and inhibitors in the active site help in understanding interaction of different substrates with GA and therefore in choosing suitable amino acid residues to mutate for improved selectivity. We have used this technique with a series of isomaltosides (Figure 1) that have strikingly different hydrolysis kinetics, and with a series of inhibitors (Figures 2 and 3) of very different strengths.

Computational techniques

Structures of the molecules to be docked were studied by conformational mapping and optimized by the molecular mechanics algorithm MM3(92) (Quantum Chemistry Program Exchange, Bloomington, Ind., or Technical Utilization Corporation, Powell, Ohio) by methods used prev-

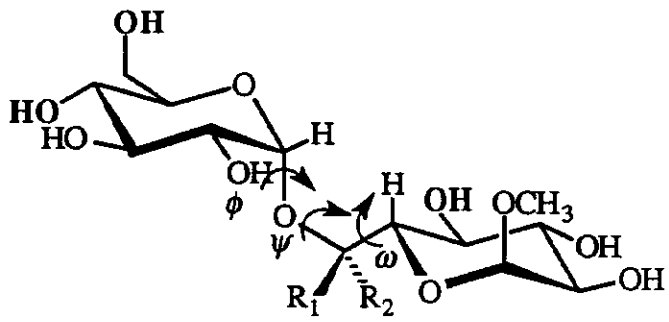

Figure 1. Methyl-α-isomaltoside (R_1 = H; R_2 = H), methyl-α-6R-C-methyl-α-isomaltoside (R_1 = CH_3; R_2 = H), and methyl-α-6S-C-methyl-α-isomaltoside (R_1 = H; R_2 = CH_3). In bold are shown the critical hydroxyl groups required for catalysis in isomaltose (Palcic *et al.*, 1993).

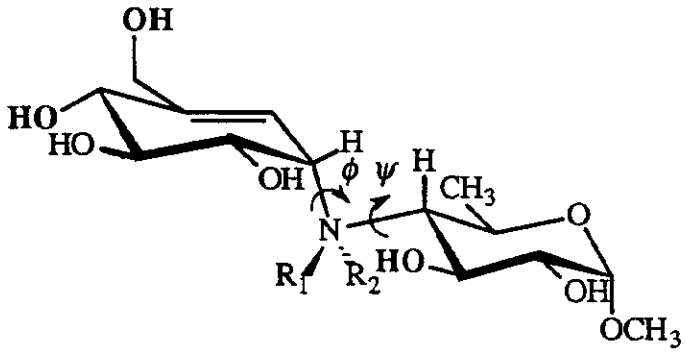

Figure 2. Methyl-α-R-acarviosinide (R_1 = H; R_2 = nothing) and methyl-α-S-acarviosinide (R_1 = nothing; R_2 = H). In bold are shown the critical hydroxyl groups required for catalysis in maltose (Palcic *et al.*, 1993).

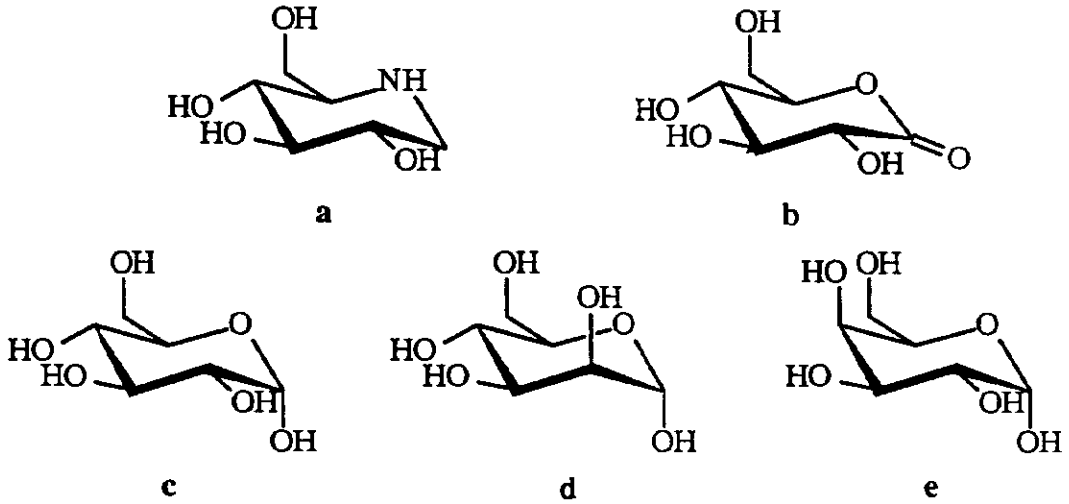

Figure 3. a) 1-deoxynojirimycin, b) glucono-1,5-lactone, c) α-glucose, d) α-mannose, and e) α-galactose.

iously (Dowd *et al.*, 1994). Different low-energy local minima were considered for disaccharide substrates and inhibitors.

The nonreducing-end ring of each ligand was superimposed on the crystal structure position of the corresponding ring of gluco-dihydroacarbose in the GA active site (Stoffer *et al.*, 1995; Aleshin, personal communication) to increase the number of successfully docked structures.

Docking simulations were with AutoDock 2.1 (Scripps Research Institute, La Jolla, CA) (Goodsell and Olson, 1990; Goodsell *et al.*, 1993) using Monte Carlo simulated annealing (the Metropolis method). Two rounds of docking simulations were made. In the first round, all low-energy disaccharide structures but only one optimized monosaccharide structure were docked. After each round, cluster analysis of all structures generated for a single compound was performed. Cluster families were based on a tolerance of 1 Å for the root mean square deviation (r.m.s.d.) for all atoms from the low-energy structure. The best structures obtained for each ligand following the first round were redocked.

Docking of Inhibitors

Numerical results for the docked structures of 1-deoxynojirimycin, glucono-1,5-lactone, and α- and β-glucose are presented in Table 1, while those for methyl-α-R- and methyl-α-S-acarviosinide are found in Table 2. Actual docked and crystal structures of 1-deoxynojirimycin appear in Figure 4, while docked structures of methyl-α-R- and methyl-α-S-acarviosinide are compared with the crystal structure of acarbose in Figure 5.

Excellent fits were obtained for all four inhibitors compared to their crystal structures in the corresponding GA complex (Table 1). Interestingly, smaller deviations were found for β-glucose than for α-glucose when both were referenced to the α-glucose structure found in a GA complex.

The two acarviosinides are close to the equivalent residues of acarbose complexed in the GA active site (Aleshin *et al.*, 1994), as are their imino linkage dihedral angles (Table 2). Their very negative binding energies agree with their very high joint K_i (2.0×10^{-7} M^{-1}, Sigurskjold *et al.*, 1994).

The docking simulations of monosaccharide substrates of GA that can be involved in condensation reactions are given in Table 3. Both anomeric forms of glucose, mannose, and galactose are able to dock in GA's active site, as found experimentally when the three monosaccharides were incubated with GA and disaccharides were formed (Pestlin *et al.*, 1995). Glucose binds better than the other monosaccharides and it reacts faster. Crystal studies of GA complexes with both anomeric forms of glucose but also with α-mannose and α-galactose (Aleshin, personal communication) indicate a preferential binding of α-glucose over β-glucose in the first site. Binding of mannose is also observed in the first site, while that of galactose is only observed at site two in the crystal structure.

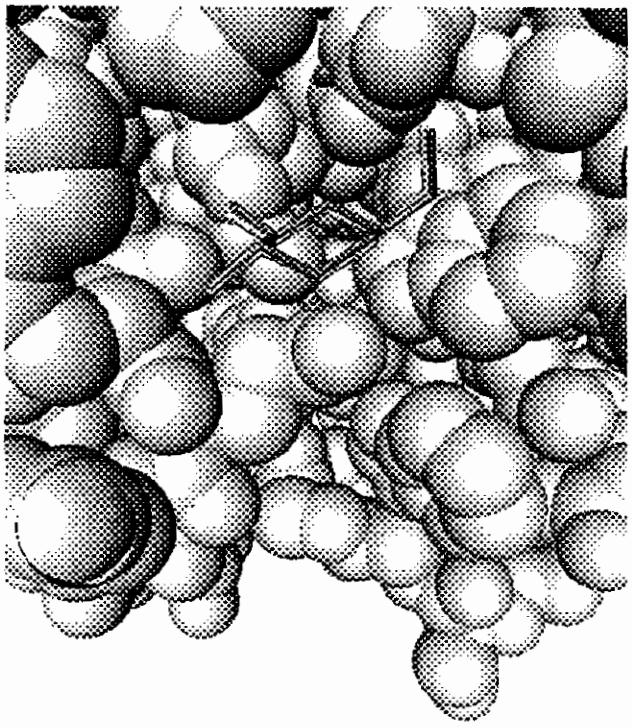

Figure 4. GA active site interacting with 1-deoxinojirimycin as obtained by docking simulation (dark grey) versus the crystal structure in GA complex (white). The catalytic water present in docking simulations is also shown.

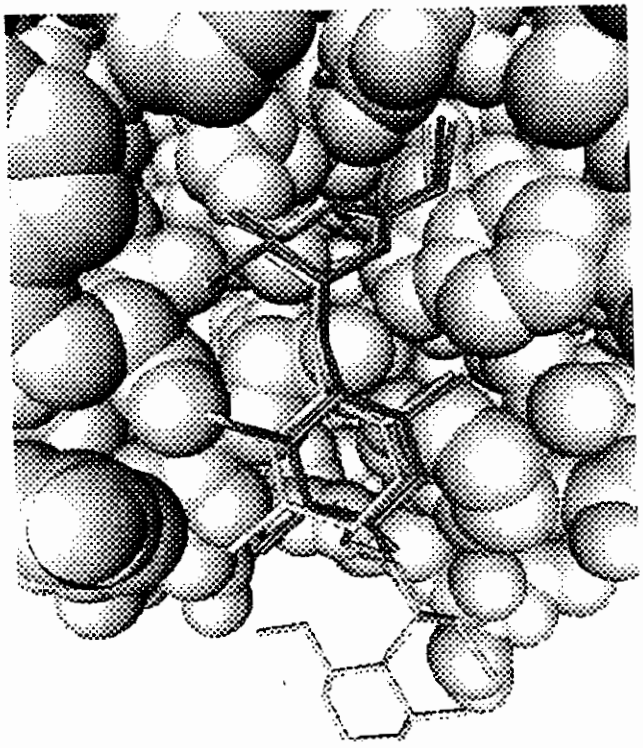

Figure 5. GA active site interacting with docked methyl-α-R-acarviosinide (dark grey) and methyl-α-S-acarviosinide (light grey) versus the crystal structure of acarbose in GA complex (white). The catalytic water present in docking simulations is also shown.

Table 1. Final results of monosaccharides and analogs. In brackets: number of structures in cluster/total number of simulations. In parentheses: cluster average results.

Substrate	Total energy (kcal/mol)	Internal energy (kcal/mol)	r.s.m.d. (Å)	K_i (M^{-1})
1-Deoxynojirimycin [327/400]	-72.03 (-67.75)	-1.46 (0.95)	0.257[a] (0.415)	3.3 x 10^4 [c]
Glucono-1,5-lactone [144/200]	-65.40 (-61.37)	-2.48 (0.73)	0.335[a] (0.584)	6.3 x 10^2 [d,e]
α-Glucose [144/200]	-71.95 (-66.52)	-1.41 (-0.99)	0.469[a] (0.638)	6.3[d]
β-Glucose [299/400]	-74.01 (-66.51)	-2.73 (1.19)	0.390[b] (0.602[b])	

[a]Using crystal structure of compound complexed with GA as reference (Harris *et al.*, 1993, Aleshin, personal communication).
[b]Using crystal structure of α-glucose complexed with GA as reference.
[c]Sigurskjold *et al.*, 1994.
[d]László *et al.*, 1978.
[e]Ohnishi *et al.*, 1990.

Table 2. Final results of acarviosinides compared to acarbose in GA complex (Aleshin *et al.*, 1994). In brackets: number of structures in cluster/total number of simulations. In parentheses: cluster average results.

Substrate	Total energy (kcal/mol)	Internal energy (kcal/mol)	Dihedral angles (°) φ	ψ	r.m.s.d. (Å)
Methyl-α-R-acarviosinide [11/100]	-104.77 (-103.55)	-4.62 (-5.96)	-19 (-14)	8 (4)	0.463[a] (0.450)
Methyl-α-S-acarviosinide [93/100]	-102.22 (-96.52)	1.41 (1.45)	-20 -20	7 (7)	0.456[a] (0.494)
Acarbose[a]			-16	6	

[a]Using crystal structure of equivalent atoms of acarbose complexed with GA (Aleshin *et al.*, 1994) as reference.

Table 3. Final docking results of monosaccharide substrates.

Substrate	Total energy (kcal/mol)	Internal energy (kcal/mol)	r.m.s.d.[a] (Å)
α-Glucose	-71.95	-1.41	0.469
β-Glucose	-74.01	-2.73	0.390
α-Mannose	-69.21	-2.21	0.733
β-Mannose	-69.07	-0.53	1.038
α-Galactose	-67.24	-0.62	0.851
β-Galactose	-70.32	-4.16	1.012

[a]Using crystal structure of α-glucose complexed with GA (Aleshin, personal communication) as reference.

Docking of Isomaltosides

Numerical results of the docking simulations of the isomaltosides are shown in Table 4, while their docked structures appear in Figure 6.

The total energy of interaction is lowest for the methyl-α-6R-C-methyl-α-isomaltoside, followed by methyl-α-isomaltoside and finally the 6S-C-compound. The results agree with the k_{cat}/K_M values obtained experimentally, even considering that the position of the 6-OH in the first methyl-α-isomaltoside structure is such that binding may not lead to hydrolysis.

Methyl-6R-C-methyl-α-isomaltoside has a clear unique low-energy binding mode. The optimal productive structure of methyl-6S-C-methyl-α-isomaltoside has a relatively low energy of interaction compared to the other isomaltosides. This is partially due to the fact that the extra methyl group is found perpendicular to the plane formed by the two glycosyl rings, and therefore it makes bad steric contacts with the active-site wall in such a way that it cannot fully penetrate the active site. Of all the isomaltosides, the 6S-C-compound had the highest internal energy, no surprise since MM3 modeling had already shown that it is the most conformationally restricted isomaltoside. As the result of these difficulties, other binding modes become accessible, such as the third cluster, which is completely non-productive.

The binding energies from docking of methyl-α-isomaltoside, methyl-6R-C-methyl-α-isomaltoside, and methyl-6R-C-methyl-α-isomaltoside agree with kinetic data. It is also shown that conformational and steric effects play a role in the binding of these isomaltosides. The similarity of the docking results of simpler compounds with results obtained by crystallography validates the approach.

More generally, an effective docking procedure for mono- and disaccharides has been developed to complement information obtained by X-ray crystallography and kinetic studies.

Table 4. Final docking results for isomaltosides in the active site. In brackets: number of structures in cluster/total number of simulations. In parentheses: cluster average results.

Substrate	Total energy (kcal/mol)	Internal energy (kcal/mol)	Dihedral angles (°) ϕ	ψ	ω	k_{cat}/K_M (mM^{-1} s^{-1})
Methyl-α-isomaltoside [136/300]	-97.48 (-90.93)	0.50 (5.59)	-19 (-18)	132 (137)	18 (9)	0.042[a]
[43/300]	-96.04 (-91.92)	10.20 11.09	-20 (-23)	146 (148)	4 (8)	
Methyl-α-6R-C-methyl-α-isomaltoside [212/300]	-102.29 (-96.52)	7.96 (1.45)	-27 (-30)	137 (141)	16 (17)	0.96[a]
Methyl-α-6S-C-methyl-α-isomaltoside [61/300]	-76.03 (-70.91)	14.78 (15.35)	-41 (43)	127 (126)	36 (34)	0.012[a]
[6/300]	-68.75 (-67.33)	12.70 (12.82)	-48 (-46)	146 (144)	53 (51)	
[86/300]	-67.94 (-59.10)	20.53 (20.49)	5 (14)	-134 (-131)	-27 (-30)	

[a]Palcic *et al.*, 1993.

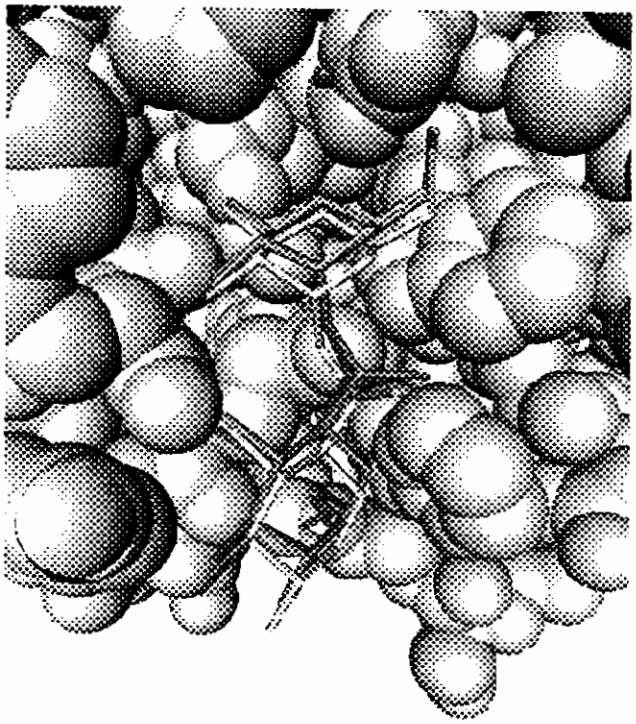

Figure 6. GA active site interacting with docked methyl-α-isomaltoside (dark grey), and with docked methyl-6R-C-methyl-α-isomaltoside (light grey) and its S-isomer (white). The catalytic water present in docking simulations is also shown.

References

Aleshin, A., A. Golubev, L. M. Firsov, and R. B. Honzatko. *J. Biol.Chem.*, **267**, 19291 (1992).

Aleshin, A. E., L. M. Firsov, and R. B. Honzatko. *J. Biol. Chem.*, **269**, 15631 (1994).

Coutinho, P. M. and P. J. Reilly. *Protein Eng.*, **7**, 393 (1994).

Dowd, M. K., P. J. Reilly, and A. D. French. *Biopolymers*, **34**, 625 (1994).

Goodsell, D. S. and A. J. Olson. *Proteins*, **8**, 195 (1990).

Goodsell, D. S., H. Lauble, C. S. Stout, and A. J. Olson. *Proteins*, **17**, 1 (1993).

Harris, E. M. S., A. E. Aleshin, L. M. Firsov, and R. B. Honzatko. *Biochemistry*, **32**, 1618 (1993).

Lászlo, E., J. Holló, A. Hoschke, and G. Sárosi. *Carbohydr. Res.*, **61**, 387 (1978).

Meagher, M. M. and P. J. Reilly. *Biotechnol. Bioeng.*, **34**, 689 (1989).

Nikolov, Z. L., M. M. Meagher, and P. J. Reilly. *Biotechnol. Bioeng.*, **34**, 694 (1989).

Ohnishi, H., H. Kitamura, T. Minowa, H. Sakai, and T. Ohta. *Eur. J. Biochem.*, **207**, 413 (1992).

Palcic, M.M., T. Skrydstrup, K. Bock, N. Le, and R. U. Lemieux. *Carbohydr. Res.*, **250**, 87 (1993).

Pestlin, S., D. Prinz, J. M. Starr, and P. J. Reilly. Unpublished results (1995).

Sierks, M. R., C. Ford, P. J. Reilly, and B. Svensson. *Protein Eng.*, 3, 193 (1990).

Sierks, M. R., C. Ford, P. J. Reilly, and B. Svensson. *Protein Eng.*, 6, 75 (1993).

Sigurskjold, B. W., B. Svensson, G. Williamson, and H. Driguez. *Eur. J. Biochem.*, **225**, 133 (1994).

Stoffer, B., A. E. Aleshin, L. M. Firsov, B. Svensson, and R. B. Honzatko. *FEBS Lett.*, **358**, 57 (1995).

Adsorption of Albumin on Polymeric Microporous Membranes

J. Johansson and R.K. Bajpai

Department of Chemical Engineering, University of Missouri, W 2030 Engineering Building East Columbia Missouri.

Abstract

Adsorption of proteins on membrane surfaces is major factor in reduction of solvent flux and mass transfer of solute molecules across membranes. Hence, adsorption of albumin on polypropylene, nylon, and polyvinylidenefluoride (PVDF) was studied. A radioactive tracer technique was used in this work. It was found that the protein-adsorption isotherms (at 24 °C) were linear in the range investigated. On polypropylene surface, the adsorption reached a plateau of ≈200 mg protein/m2. This corresponds to a thickness of 100 monolayers of albumin (side on) on the polymer surface. No saturation was observed for nylon and PVDF surfaces. There was almost no effect of pore size on the adsorption isotherms. Aqueous phase ionic strength adversely affected adsorption behavior of the protein on PVDF membranes. The effect of ionic strength on adsorption on nylon membranes was, however, opposite.

Introduction

Microfiltration is an important unit operation in membrane technology. Important applications are, for example, cell-recycling, sterilization, and protein purification. However, a reduction of flow often occurs when exposed to process solutions under flow conditions especially for biological macromolecules. It is believed that the phenomena that is mainly responsible for this behavior is adsorption.

Adsorption takes place instantaneously when a solid surface comes into contact with biological fluids. The macro- molecular film then formed, may act as a substratum for subsequent fouling or adhesion of cells.

A study was therefore initiated to obtain protein isotherms on selected membrane materials. PVDF was selected because it has been termed " a low protein-binding " membrane. Polypropylene was selected because of its hydrophobic character and finally, nylon was selected because its natural form possesses a positive charge.

Materials and Methods

The following materials was studied.

-Polyvinylidenefluoride (PVDF) with pore sizes 0.2 and 0.45 μm

- Polypropylene with pores sizes 0.1 and 0.45 μm and non porous sheet

-Nylon with pores sizes 0.1 and 0.45 μm

The surface area was measured in a BET Sorptometer (Porous Materials Inc.) with argon gas as a adsorbate at liquid nitrogen temperature. Unlabeled bovine serum albumin (globulin free, lyophilized and crystallized) was obtained from Sigma Chemical Co. The labeled bovine serum albumin was obtained from American Radiolabeled Chemical Inc. The water used for buffer

preparation was distillated and then taken through a deionizer followed by purification with an ion exchanger and finally filtered through a 0.2 µm membrane. Chemicals used for buffer preparation were all of analytical grade. The labeled and unlabeled protein were mixed in buffered water solution. The surfaces were then added to the protein solution and equilibrated. From the aqueous phase 1 ml was taken out. The surfaces were thereafter rinsed four times during a time period of approximately 10 minutes. Liquid scintillation cocktail was added (Fisher) and then the samples were counted with a Liquid scintillalator Counter (LS 7000, Beckman).

Results and Discussion

Surface area determination

For all adsorptive phenomena it is crucial to have knowledge of the area that is available for the adsorbing species. Protein adsorption data can be reported as mg adsorbed protein/ g membrane [ ] or be reported as mg adsorbed protein/mg planar area [ ]. However, for protein adsorption data reported in this way no comparison can be made with other surfaces or even within the same surface material with different pore sizes. The surface area for different membranes and pore sizes are shown in Table I.

Table I. Surface area and ratio surface area to frontal area for different membrane types and pore sizes

Membranes	Pore size (μm)	Surface area (m^2/g)	Ratio Surface area to frontal area
PVDF	0.2	8.6	557
PVDF	0.45	2.9	222
PP	0.1	22.0	595
PP	0.45	2.3	190
Nylon	0.1	11.5	716
Nylon	0.45	7.5	408

A low pore size membrane has a higher BET area/g compared to a high pore size membrane. The internal surface area of a polymeric microporous membrane is 100-700 larger than the membrane frontal area.

Protein adsorption

Protein adsorption isotherms are shown in Figures 1-3. They are linear in the range investigated On polypropylene surface, the adsorption reached a plateau of ≈200 mg protein/m2. This corresponds to a thickness of 100 monolayers of albumin (side on on the polymer surface. No saturation was observed for nylon and PVDF surfaces. That no saturation was found for these surfaces is not surprising since large amount of protein deposits is often found for polymeric membranes at large solution concentration [ ]. At small solution concentration the amount adsorbed is rather low, for example a value of 0.43 mg/m^2 is obtained at a protein concentration of 1 mg/ml using linear regression. This value can be compared with data reported by

Aldo Pitt. He obtained a value of 0.064 mg/m^2 on 0.22 µm PVDF using the same protein concentration, 0.14 M NaCl and 0.02 M Phosphate buffer pH 7.2.[Jnl of Parenteral Science and Technology, 41, 110 (1987)]. Even if these values differ in one magnitude they are both less than monolayer (side on). Experimental errors and difference in analytical methods may explain the discrepancy. There was almost no effect of pore size on the adsorption isotherms. It can be argued that the surface area obtained with the BET method is larger than the area accessible to proteins because the size difference between the gas molecule and the protein. If that would the be case it is not likely that the adsorptions isotherms for different pore sizes would coincidence. Therefore, the BET area represent a total area that are easy accessible to albumin at least for the presently investigated membranes.

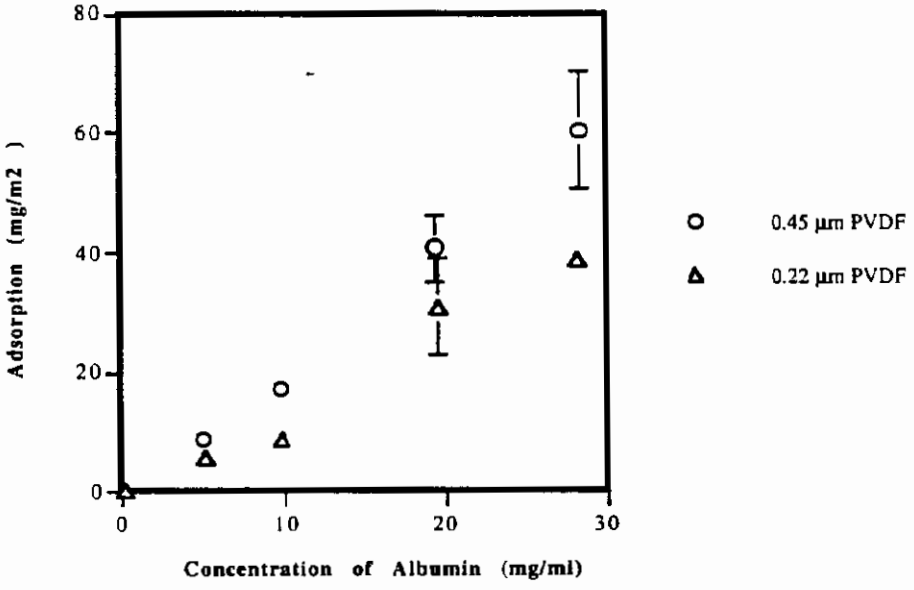

Figure 1 Amount albumin adsorbed on PVDF at different solution concentrations of albumin (pH=7.0, T=24 C, 0.01 M phosphate buffer with 0.15 M Nacl)

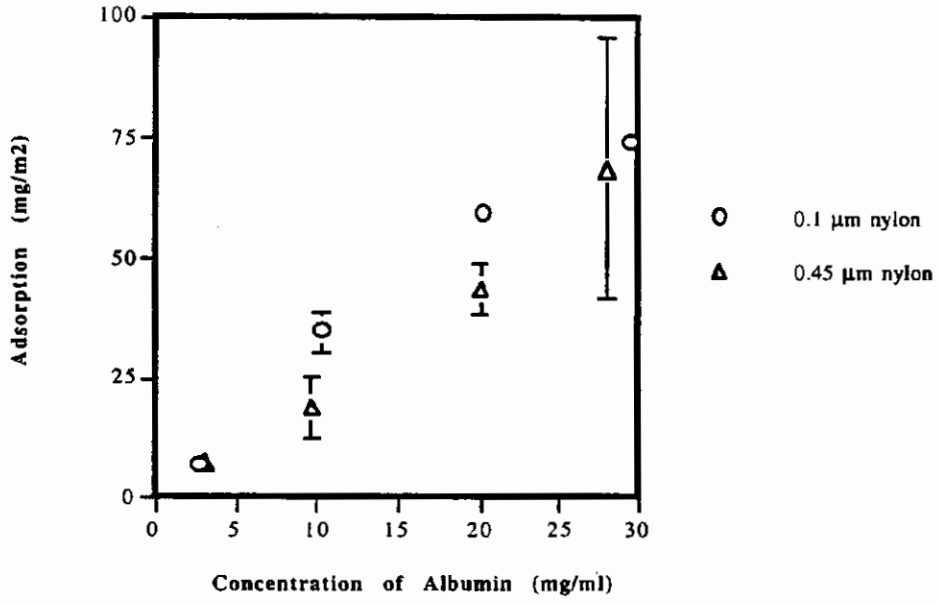

Figure 2 Amount albumin adsorbed on nylon at different solution concentrations of albumin (pH=7.0, T=24 C, 0.01 M phosphate buffer with 0.15 M Nacl)

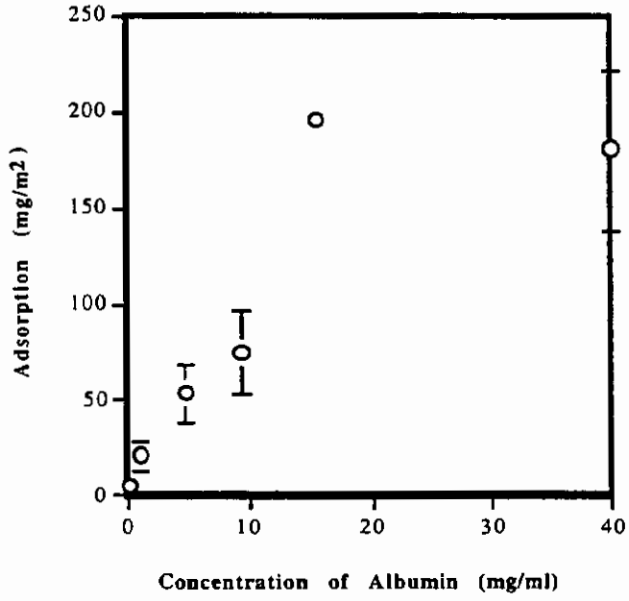

Figure 3 Amount albumin adsorbed on polypropylene at different solution concentrations of albumin (pH=7.0, T=24 C, 0.01 M phosphate buffer with 0.15 M Nacl)

The effect of changing the ion strength on albumin adsorption can be seen in Figure 4 to 5. For PVDF a weak reduction of adsorption with increasing ionic strength can be detected. It is in agreement with result from Bowen et al.[ ] were also a reduction in amount albumin adsorbed with an increase in ionic strength was observed. DuraPore or PVDF in its original version was a hydrophobic membrane, but it has however been modified by incorporating hydrophilic groups into the membrane matrix. It is thus basically a hydrophilic membrane. The zeta potential have also been reported at a value of -19.5 mV at pH 7.0 [ ] for the hydrophilic PVDF. At this pH albumin carries a negative charge. Ionic interaction are then expected to dominate and an increase in ionic strength may further increase this interaction and also lower the level of albumin adsorbed. An increase of amount adsorbed with increasing ionic strengths can be observed for nylon. In its natural form it possesses a positive charge. Ionic interaction between albumin and nylon is the dominating type of interaction. Increasing the ionic strengths will further strengthen the attracting ionic interaction. This will lead to an increase in adsorption. It is also observed that a the standard deviation in Figure 4 to 5 decreases with increasing ionic strengths this may indicate that the protein is more stable at higher ionic strengths.

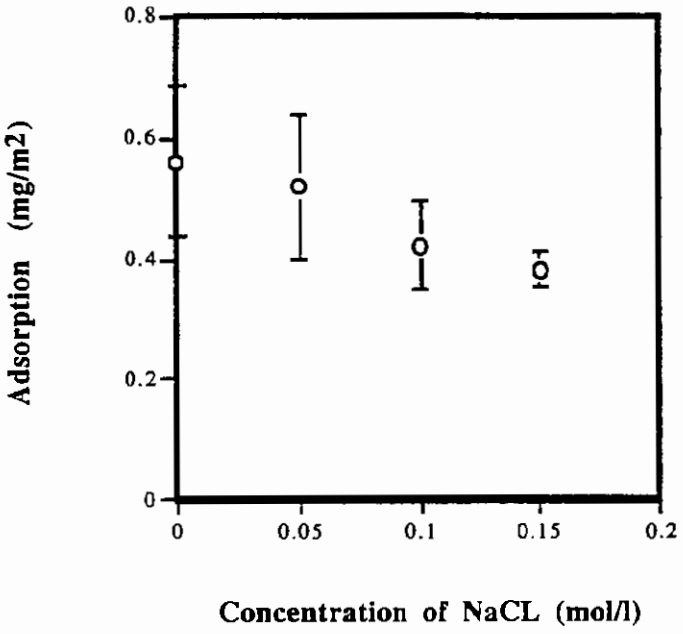

Figure 4. Adsorption of albumin on PVDF as a function of NaCL concentration (pH=7.0 , T=24 C and 0.2 mg/ml albumin)

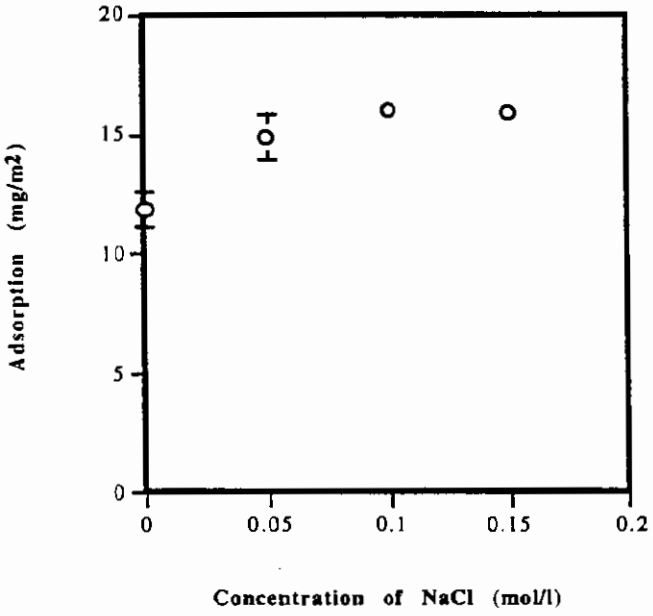

Figure 5. Adsorption of albumin on nylon as a function of NaCL concentration (pH=7.0 , T=24 C and 0.2 mg/ml albumin)

In Figure 6 adsorption of albumin for the different surfaces is compared.

Of the surfaces polypropylen adsorbed the highest amount followed by nylon and then PVFD. The higher amount of albumin adsorption on polypropylene is attributed to its hydrophobic character. That nylon have higher adsorption than PVDF can possible depend on that ionic attraction play a large roll in the interaction between albumin and the nylon surface.

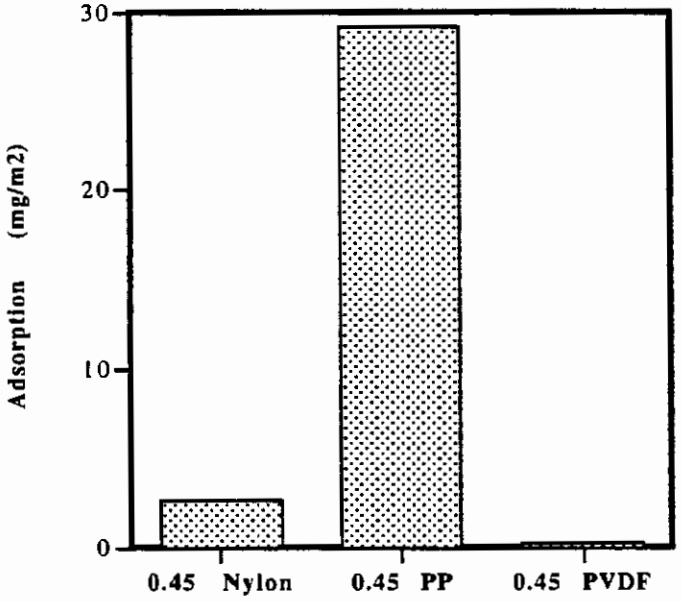

Figure 6. Adsorption of albumin on 0.45 µm nylon, polypropylene and PVDF (pH= 7.0, T=24 C, 0.01 M phosphate buffer 0.2 mg/ml albumin)

Conclusion

For the membranes investigated there was no effect of pore size on the adsorption isotherm. The BET area therefore represented the total area accessible to the protein bovine serum albumin. The high adsorption on polypropylene and nylon is attributed to the hydrophobic and electrostatic character of these surfaces. The amount of albumin adsorbed decreased with ionic strength for PVDF but increased with ionic strength for nylon. This is attributed to the different surface charge of the two surfaces.

25th ANNUAL BIOCHEMICAL ENGINEERING SYMPOSIUM
COLUMBIA, MO 65211
SEPTEMBER 16, 1995

E1419 Engineering Building East, MU

9:00 - 9:25 AM	**Pedro M. Coutinho**, Iowa State University Automated Docking of Three Isomaltosyl Analogues and Several Inhibitors into the Active Site of Glucoamylase
9:25 - 9:50 AM	**Barry Vant-Hull**, University of Colorado The Binding of T7 RNA Polymerase to Double-Stranded DNA
9:50 - 10:15 AM	**Brad Forlow**. University of Oklahoma The Effect of P-selectin Site Density on the Rolling Velocity of White Blood Cells
10:15 - 10:40 AM	**Jeff Kern**, University of Colorado Improvement of RNA Transcription Yield Using a Fed-Batch Enzyme Reactor
10:40 - 11:00 AM	**COFFEE BREAK**
11:00 - 11:25 AM	**Michael Rigney**, University of Kansas Investigation of Cyclic Shear Stress Effects on Mammalian Cells
11:25 - 11:50 AM	**Jin Zhong**, University of Missouri - Columbia Effectiveness of Oligomeric Lactic Acid in Lowering Surface pH of Beef
11:50 AM - 12:15 PM	**LaToya Jones**, University of Colorado Purification of Recombinant Hepatitis B Vaccine: Effect of Virus/Surfactant Interactions
12:15 - 1:45 PM	**LUNCH BREAK**
1:45 - 2:10 PM	**Satish K. Santharam**, Kansas State University Surfactant-Enhanced Remediation of a Non-Aqueous Phase Contaminant in Soil
2:10 - 2:35 PM	**Krishna M. Subramanian**, University of Missouri - Columbia Biodegradation Studies Using a Respirometer

2:35 - 3:00 PM **Narayan Muralidharan**, Kansas State University
Biodegradation Studies of Organic Pollutants in a Chamber in the Presence of Alfalfa Plants

3:00 - 3:25 PM **Patrick C. Gilcrease**, Colorado State University
Biotransformation of TNT under Aerobic and Anoxic Conditions

3:25 - 5:00 PM **COFFEE BREAK and POSTER VIEWING**

POSTERS

Ching-Yuan Lee, University of Colorado
Application of Osmotic Dewatering to the Crystallization of Oligonucleotides for Crystallography

Carolym L. Lauron, University of Oklahoma
Biological Imaging with the Atomic Force Microscope

Martin Heller, University of Colorado
The Effect of Polyethylene Glycols and Dextrans on the Lyophilization of Human Hemoglobin

Jan Johansson, University of Missouri - Columbia
Adsorption of Albumin on Polymeric microporous membranes

Florence Kolasinki, University of Oklahoma
Effects of Aryl Sulfatase and Peroxidase on the Biodegradation of an Asphaltene Petroleum Fraction

Kevin Leung, University of Missouri - Columbia
Conductivity Tracer Studies in a Fluidized-Bed Bioreactor

Sridhar Sunderam, University of Kansas
Oxygen Transport and Mixing Considerations for Microcarrier Culture of Mammalian Cells in an Airlift Reactor

Prashant Kalia, University of Missouri - Columbia
A Bioreactor Model to Aid the Design of Treatment System for Toxic Organics

Laura Worthen, University of Oklahoma
Intracellular Calcium Changes in Endothelial Cells

Travis V. Thelin, University of Colorado
Bed-Height Dynamics of Expanded Beds

Xueou Deng, Kansas State University
Production of Protein-Rich Beverages from Cheese Whey and Soybean by Rapid Hydration Hydrothermal Cooking

Sudhakar A. Vivek, University of Missouri - Columbia
TCE Metabolism in a Fluidized-Bed Bioreactor